6-2019

Modular Synthesis of Targeted Molecular Imaging Agents for MRI, PET, and PET-MRI of Cancer

Kelsea Jones
kgj5109@rit.edu

Modular Synthesis of Targeted Molecular Imaging Agents for MRI, PET, and PET-MRI of Cancer

Kelsea Jones

A thesis submitted in Partial Fulfillment of the Requirements for the Degree

Master of Science in Chemistry

Supervised by
Dr Hans Schmitthenner

School of Chemistry and Materials Science
College of Science
Rochester Institute of Technology

June 2019

Signature of the Author _____

Accepted by _____
Director, M.Sc. Degree Program Date

SCHOOL OF CHEMISTRY AND MATERIALS SCIENCE
COLLEGE OF SCIENCE
ROCHESTER INSTITUTE OF TECHNOLOGY
ROCHESTER, NEW YORK

CERTIFICATE OF APPROVAL

M.S. DEGREE THESIS

The M.S. Degree Thesis of Kelsea Jones has
been examined and approved by the thesis
committee as satisfactory for the thesis required
for the M.S. Degree in Chemistry.

_____
Dr. Hans Schmitthenner, Thesis Advisor

_____
Dr. Scott Williams

_____
Dr. Joseph Hornak

_____
Dr. George Thurston

_____
Date

Abstract

Molecular imaging is a field widely used in the diagnosis and treatment of cancer. We offer here a modular method for the synthesis of targeted molecular imaging agents (TMIAs), which will improve the accuracy of current molecular imaging methods, as well as allow for earlier detection of tumors. The use of TMIAs in molecular imaging yields increased signal at cancerous cells and reduced signal from healthy cells. Our modular approach is useful as a facile method for the synthesis of dual-modal TMIAs for PET-MRI, which combine the sensitive detection of functional activity from PET with the high-resolution structural information obtained by MRI. Here, we present the synthesis of both a TMIA for the MRI of prostate cancer, followed by the synthesis of a dual-modal TMIA for use in simultaneous MRI-PET. By our method, a lysine backbone is utilized for the synthesis of imaging modules, by means of coupling the DOTA cyclene to the side chain of the lysine. A metal such as Gd^{3+} for use as an MRI contrast agent is chelated by DOTA. The imaging module is then coupled to a targeting moiety, such as c(RGDyK), through a carbon linker such as DSS or SMCC, to yield a novel TMIA. This same method is applied to the synthesis of dual-modal TMIAs featuring imaging modules for use in both MRI and PET. In the case of PET, where a radioactive isotope is required, we utilize a stable lanthanide placeholder that can be replaced by a useful metal isotope, such as ^{64}Cu, at the end of the synthesis. Through the course of this research, our modular approach to the synthesis of TMIAs has proven to be an effective method of synthesis, and intermediate steps have been optimized. Additionally, methods of measuring the relaxivity of MRI contrast agents have been applied to our novel compounds for comparison with commercial agents available in clinical labs, hospitals, and imaging centers today.

Acknowledgements

This endeavor was by no means a solo project. I would like to thank, first and foremost, my advisor, Dr. Hans Schmitthenner, who was supportive at all stages as I began my career as a chemist.

I could not have done any of this without my family, who supported me financially and academically, and supported my pursuit of this degree. I must also acknowledge my girlfriend: Allyssa, thank you for helping me maintain my sanity the last five years.

I'm very grateful to the community at RIT, both within the lab and outside of it. I'd like to extend my thanks to all my lab mates, past and present, who provided the groundwork for this project: Mike Regan, for his mentorship when I first joined this lab; Chelsea Weidman and Stephanie Beach for laying the groundwork in the 'puzzle-piece' synthetic method; Jessica Perez, for her transmetallation and kinetic studies; and Damien Dobson for his work with the DCL targeting module. Everyone was supportive along the way and provided advice and morale during this project.

I would also like to thank all the professors I've encountered along the way, who provided important lessons during my years of study, particularly Dr. Nathan Eddingsaas, Dr. Jeffrey Mills, and my committee members: Dr. Joseph Hornak, Dr. Scott Williams, and Dr. George Thurston. Thank you for your support during this time. Additionally, I would like to thank Dr. Hornak for his assistance with the MRI side of the project.

Financial support for this project was received from two R15 NIH grants from the NIH: 1R15CA192148-01 entitled "Targeted Molecular Agents for Photoacoustic Imaging of Prostate Cancer" and R15CA219915-01 entitled "High Relaxivity PSMA-Targeted Contrast Agents for MRI of Prostate Cancer".

Abbreviations

Frequently Used Solvents

- ACN: acetonitrile
- AmAc: Ammonium Acetate, used as an aqueous buffer
- DCM: dichloromethane
- DI H_2O: deionized water, 18mΩ
- DMF: n,n-dimethylformamide
- DMSO: dimethyl sulfoxide
- EtOAc: ethyl acetate
- MeOH: methanol
- NMP: n-methylpyrrolidone

Frequently Used Reagents and Compounds

- BuAm: n-butylamine
- DEA: diethylamine
- DIPEA: diisopropylethylamine
- dLys, dK: the unnatural isomer of lysine
- DOTA: 1,4,7,10-tetraazacyclododecane-1,4,7,10-tetraacetic acid
- Lys, K: lysine, a natural amino acid
- NMM: n-methylmorpholine
- TEA: triethylamine
- TFA: tetrafluoroacetic acid

Other Instrumentation

- HPLC-MS: high-pressure liquid chromatography and mass spectrometry
- HPLC-prep: preparative high-pressure liquid chromatography
- NMR: nuclear magnetic resonance
- SPE: solid-phase extraction

Molecular Imaging Terms

- CA: contrast agent for MRI use
- MRI: magnetic resonance imaging
- PET: positron emission tomography
- TCA: targeted contrast agent for MRI use
- TMIA: targeted molecular imaging agent

Table of Contents

Abstract ..... *iii*
Acknowledgements ..... *iv*
Abbreviations ..... *v*
Table of Contents ..... *vi*
List of Figures ..... *vii*
List of Schemes ..... *viii*
List of Tables ..... *viii*

Chapter 1. Introduction 1
1.1 Background: Cancer 1
1.2. Molecular Imaging in Cancer Treatment 2
1.3 Targeted Molecular Imaging Agents 4
1.5 Molecular Imaging Methods 7
1.6 Magnetic Resonance Imaging 10
1.6.1 A Simple Treatment of MRI Theory 10
1.6.2 MRI Contrast Agents 12
1.7 Positron Emission Tomography 14
1.7.1 Theory and Physics of PET 14
1.7.2 Radionuclide Imaging Agents 15

Chapter 2. Experimental Approach 18
2.1 Modular Synthetic Approach to TMIA Synthesis 18
2.2 Novel use of Metals as DOTA-Protecting Groups 22
2.3 Evaluation and Analysis of Compounds 25

Chapter 3. Results and Discussion 27
3.1 Optimization of One-Pot Reactions for Synthesis of Imaging Modules 27
3.2 Simple Fmoc Deprotections 30
3.3 Troublesome Dimetal Peptide Coupling Reactions 31
3.4 Fmoc Deprotection of dipeptide module 36
3.5 SMCC vs DSS carbon linker 37
3.6 Synthesis of TMIA containing SMCC linker 39
3.7 Synthesis of TMIA containing DSS linker 41
3.8 Convergent Synthesis of TMIA for MRI of Prostate Cancer 43
3.9 T_1 Relaxivity Measurements 45
3.10 Transmetallation of La^{3+} to Cu^{2+} Successful, Though Incomplete 48
3.11 Preferred Methods of Purification and Analysis 50
3.12 Successful Synthesis of Several TMIAs by a Modular Approach 51

Chapter 4. Conclusion 53

Chapter 5. Experimental Procedures 54

References 59

Appendix I. HPLC-MS & HRMS Data 64

List of Figures

Figure 1. c(RDGyK) 5

Figure 2. CFM images of A549 lung cancer cells targeted by NIR-TMIA: c(RDGyK)-Cy5.5 6

Figure 3. DCL urea-based PSMA inhibitor. N-[N-[(S)-1,3-dicarboxypropyl]carbamoyl]-(S)-L-lysine. 6

Figure 4. Structure of Breast cancer peptide 18-4. 7

Figure 5. An example of individual PET and MRI scans, and the fused image of the two scans, showing the high-resolution structure and the sensitive biological activity information which can be obtained from such an image.[36] 8

Figure 6. Representation of the precession of a nucleus about the applied B_0 magnetic field..[45] 10

Figure 7. Representation of the T2 decay process, showing how the many spins in a sample dephase over time after the initial excitation by an RF pulse to ultimately produce a net magnetic spin of zero. 11

Figure 8. A selection of commercially available Gd-based CAs.[49] 13

Figure 9. Elementary graphic explanation of theory behind PET.[52] 15

Figure 10. General schematic for synthesis of a dual-modal TMIA 19

Figure 11. Color-coded structure for one of the final TMIA products, c(RGDyK)-SMCC-dK(DOTA-Cu)-K(DOTA-Gd)-NH2, useful for targeted PET-MR of cancer. 19

Figure 12. Graph showing the displacement of La^{3+} by Cu^{2+} in a DOTA chelator in 0.1M TFA over several days, as well as the stability of Gd-DOTA in those same conditions. Data points were obtained by HPLC-UV analysis, and the intensity was taken from the area under the curve for the UV-absorption of each compound. 25

Figure 13. CFM image of A249 lung cancer cells treated with NucBlue and a previously synthesized TMIA for MRI and fluorescence of cancer cells, using the c(RGDyK) targeting peptide. Cell nuclei are stained blue; the TMIA appears red due to fluorescence. 26

Figure 14. A selection of organic bases (top row) and peptide coupling reagents (lower two rows) which were considered. 33

Figure 15. Fmoc-dAla-OH (left) and Fmoc-dLys(DOTA-La)-OH (**5**), right. 33

Figure 16. SMCC linker. 38

Figure 17. DSS linker. 38

Figure 18. DCL-DSS-K(DOTA-Gd)-NH2 42

Figure 19. Sample plot used to determine T_1 and S_0 for a sample. Signal Intensity is obtained from the integration of the peak for each repetition, and the inversion time is increased for each repetition. The blue points represent the experimentally obtained data points, and the orange curve represents the theoretical values obtained by equation (2). 47

Figure 20. Sample plot used to determine the relaxivity of a contrast agent. R_1 values are taken from the solution found for each equation (2) at each concentration. Y-intercept of the linear intercept represents the R_1 for a sample of H_2O without the presence of [Gd^{3+}] contrast agent; the slope yields the relaxivity of the contrast agent at a given field strength. 47

Figure 21. Showing the relaxivities of four distinct compounds as measured by inversion-recovery sequences on the 43MHz Magritek NMR. 48

List of Schemes

Scheme 1. Schematic for linear method of dual-modal TMIA synthesis. 21

Scheme 2. Schematic for convergent method of synthesis for dual-modal TMIA. 21

Scheme 3. Multi-step procedure for synthesis of Fmoc-Lys(DOTA-Gd)-NH_2 , **3a**. 27

Scheme 4. One-pot synthesis of Fmoc-Lys(DOTA-Gd)-NH_2, **3b**. 28

Scheme 5. Undesirable di- and tri-substituted byproducts. 29

Scheme 6. One-pot synthesis of **5**, PET placeholder module. 30

Scheme 7. Fmoc deprotection of **3** to yield H-Lys(DOTA-Gd)-NH_2, **4**. 30

Scheme 8. Initial method for peptide coupling to yield dual-modal imaging agent. 32

Scheme 9. Activation of an acidic lysine backbone by TSTU yields a succinimidyl leaving group. 35

Scheme 10. Monitoring NHS ester formation by addition of butyl amine to form a more lipophilic product which is easily observed by HPLC-MS. 35

Scheme 11. Fmoc deprotection of **6** to yield H-dLys(DOTA-La)-Lys(DOTA-Gd)-NH_2,**7**. 37

Scheme 12. Coupling of SMCC to **7** for formation of **9**. 40

Scheme 13. Coupling of c(RGDyK) to **9** for formation of **11**. 40

Scheme 14. Coupling of DSS to di-metal module **7** for formation of **8.** 41

Scheme 15. Coupling of c(RGDyK) to **8** for formation of **10**. 42

Scheme 16. Convergent synthesis of TMIA for MRI of prostate cancer, DCL-DSS-K(DOTA-Gd)-NH_2 (**14**) 44

List of Tables

Table 1. Summarizing some useful properties of isotopes used in PET as radionuclides for imaging.[55] 16

Chapter 1. Introduction

1.1 Background: Cancer

Cancer is among the most widely feared diseases of the twenty-first century, and one of the leading causes of mortality worldwide, due to the numerous types which can manifest and cause damage. In 2012, more than 14 million new cancer cases appeared worldwide, and there were more than 8 million deaths due to cancer.[1] Even as our medical understanding of the disease improves and developments are made in medical treatment of cancer, the number of new cases of cancer annually worldwide is expected to increase to 22 million by 2030.[2] Improving methods for the detection and treatment of cancer are crucial areas of research to pursue in the fight against cancer.

Cancer begins as a localized disease based on unrestrained cell replication. Cells reproduce; that is the basis of life. Healthy cellular reproduction is in equilibrium with cellular death and decay. When there is an error in the cells' DNA which causes the cells to reproduce too quickly, unrestrained reproduction results in the growth of a tumor, which may or may not be cancerous. Some tumors are benign: they remain localized to one area, generally do not increase in size beyond a certain point, and can easily be removed if needed, though they often don't warrant such treatment. (Moles are one example of such a benign tumor.) Other tumors, however, may be malignant, and are considered cancerous. Cancerous cells are able to progress through the circulatory and lymphatic systems, leading to metastasis to other parts of the body. The cancer then interferes with other cells and essential biological functions, resulting in serious illness or death.[3]

After the cancer has metastasized and tumors are growing in different regions across the body, surgical treatment of the cancer becomes difficult and will likely not

be wholly effective, so more aggressive methods of treatment are required. These aggressive treatments include chemotherapy and radiotherapy, which are meant to slow or stop the growth of the cancerous cells that reproduce so quickly. However, these methods of treatment often cannot distinguish any difference between cancerous cells and healthy cells, so all fast-growing cells are attacked, including, most notably, hair cells and cells in the digestive tract, such as those in the stomach and intestines. Although chemotherapy and radiation are successful in a large proportion of cases, it is no secret that these aggressive treatments take their toll on the patients. Side effects of chemotherapy- and radiation-based treatments can cause problems in and of themselves, and include a loss of hair, loss of appetite, change in taste preferences, vomiting, dehydration, fatigue, lymphedema, and blood disorders such as low red blood cell counts.[4]

1.2. Molecular Imaging in Cancer Treatment

Because cancerous tumors can develop and spread very quickly, early diagnosis is the best defense against cancer. If a cancer is detected at an earlier stage, before it has metastasized, then the tumor(s) may be more easily removed by surgery, chemotherapy or targeted radiation than would be possible for a more developed form of that cancer. Currently, a variety of methods are used to detect and diagnose cancer in patients, including invasive methods (such as biopsies) and non-invasive imaging methods such as x-rays, computed tomography (CT), positron emission tomography (PET), magnetic resonance imaging (MRI), and ultrasound imaging techniques.[5–8] In some types of molecular imaging (most notably, MRI, PET, and CT), a variety of small molecules, nanoparticles, quantum dots, or biosensors may be useful as imaging agents or contrast agents which improve the quality of the image.[8–10]

Regardless of the method of imaging used, the purpose is to allow medical professionals to locate the cancerous cells in the body, determine how far the cancer has spread, and to what degree it is currently present in the body, and determine the most effective method of treatment. If the cancer is diagnosed, detected, and located prior to metastasis, the tumors are small and localized, and can be surgically removed with good prognosis.

However, such early detection is not always possible with current methods of imaging. At very early stages, cancerous cells may not be distinguishable from healthy tissue in the image. Therefore, improvements in methods for molecular imaging of cancer cells offers great potential to aid doctors in the early detection and treatment of cancer, and will reduce the mortality associated with the most fatal types of cancer.

When methods of molecular imaging are considered, the extent of imaging required for diagnosis and treatment should be limited. This is especially true in methods involving exposure to potentially harmful radiation or materials. Some methods of imaging, such as PET, rely on the use of radioactive nuclei. Other imaging methods use radiation in the form of short-wave energy, such as x-rays and CT scans, and while limited exposure (for example, that which is experienced during the acquisition of a single x-ray image) is safe for the average patient, repeated exposure to ionizing radiation can be detrimental, and may itself may be a factor which contributes to an increased risk of cancer.[11] Additionally, the risks associated with such radiation exposure are elevated for patients of compromised health, such as young children, those already suffering from chronic ailments, and the elderly.

When all of this is taken into account, there are several important factors to keep in mind when considering methods for the improvement of molecular imaging methods and the application of such methods to the diagnosis and treatment of cancer. One: the

imaging method should be specific to the cancerous cells of interest, so that even small areas of cancerous cells may be distinguished from healthy tissues, and so that healthy tissues will not be misdiagnosed as tumors. Two: the efficiency of the contrast agent used for the imaging method should be increased, thereby lowering the required dosage. This will reduce the potential for negative side effects that result from the accumulation of toxic metals in the body or excessive exposure to radiation. Three: the improvements to imaging methods should be easily translated to the diagnosis and treatment of a variety of cancers, in order to have the widest possible impact.

1.3 Targeted Molecular Imaging Agents

One recent development towards improving molecular imaging methods is the use of targeted molecular imaging agents (TMIAs).[7,12–14] By targeting the imaging agent to the cancerous cells, the imaging agent will collect more densely at the diseased areas of tissue. This increases the signal at the diseased cells and reduces the signal arising from healthy cells.[15] Therefore, the cancerous cells can be more easily distinguished from the healthy tissue, even when only very small quantities of diseased cells are present, and the cancer can be more effectively treated and removed from the body. Biomarkers on cancer cells have been successfully targeted in a number of molecular imaging methods, including ultrasound imaging, near infrared (NIR) imaging, MRI, and PET, by coupling a compound or small protein with an affinity for a biomarker to a contrast or imaging agent.[7,12,14,16,17]

Potential biomarkers for cancerous cells include a variety of components. For example, prostate cancer tumors and cells overexpress prostate-membrane specific antigen (PSMA), so PSMA can function as a target for cancer treatments and imaging methods for use in patients with prostate cancer.[17–19] Tumors found in breast cancer, on

the other hand, overexpress estrogen receptors (ER), progesterone receptors (PrG), and human epidermal growth factor 2 (HER2), each of which may serve as a targeted biomarker in breast cancer imaging, as shown in confocal fluorescence microscopy (CFM) studies.[5]

1.4 Targeting Groups of Interest

In the early days of molecular imaging, certain peptides were found to target biomarkers found on a wide range of cancerous cells, such as cyclo(Arg-Gly-Asp-dTyr-Lys), or c(RGDyK) (Figure 1). The RGD peptide has an affinity for the $\alpha_v\beta_3$ integrin that is overexpressed in a number of types of cancer cells, including melanoma, ovarian, lung, and breast cancer.[20,21] c(RGDyK) is favored as a targeting group and is used to test targeted imaging methods due to its reproducible affinity for a variety of cancer cells.

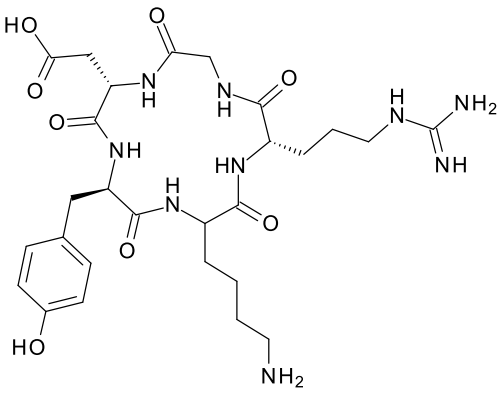

Figure 1. c(RDGyK)

The cyclic peptide, c(RGDyK) was also the first targeting moiety employed in our imaging agent lab leading to early TMIAs in our group in which the dye Cy5.5 was simply bound to the targeting agent, and was utilized to provide CFM images of A549 lung cancer cells in the Evans lab here at RIT (Figure 2).

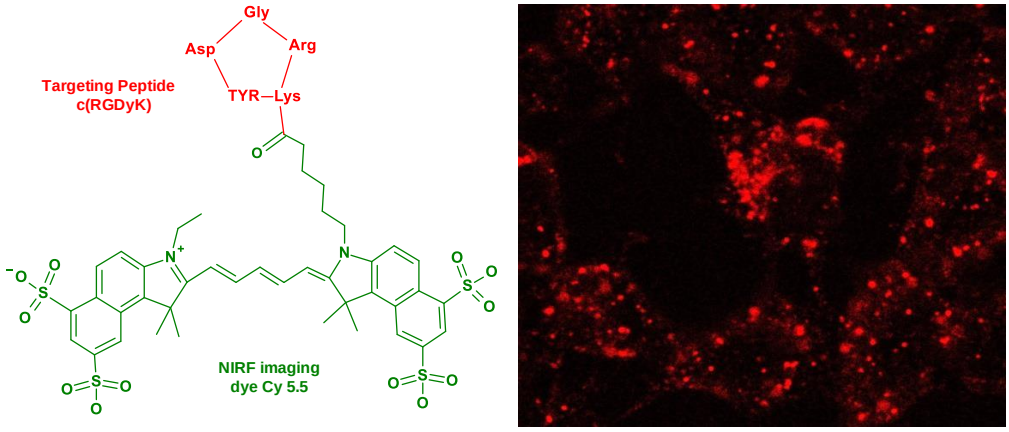

Figure 2. CFM images of A549 lung cancer cells targeted by NIR-TMIA: c(RDGyK)- Cy5.5

In the interest of creating TMIAs which are useful for specific types of cancer, it is important to explore specific targeting groups which might be useful for biomarkers of different cancers. Within our group, we have developed a method for the synthesis of a urea-based targeting moiety for prostate cancer (PrCa). DCL urea (Figure 3) is based on the Glu-urea-Lys dipeptide, and is known to target PSMA and therefore is being aggressively pursued in clinical studies as a targeting group in PrCa-specific imaging agents or treatments.[22–29] Based on this current research, DCL is a strong candidate for use in a contrast agent that is specific to PrCa.

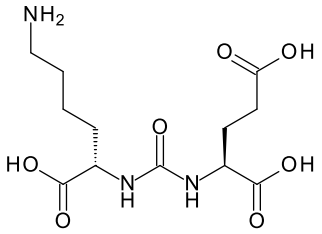

Figure 3. DCL urea-based PSMA inhibitor. N-*[*N-*[(*S*)-1,3-dicarboxypropyl]carbamoyl]-(*S*)-L-lysine.*

There are also more specific targeting moieties being developed, including a targeting peptide for breast cancer (BrCa), 18-4 (WxEAAYQkFL). Dr. Kamalijit Kaur (Chapman University, CA) developed that peptide and is collaborating with our group to synthesize a TMIA for BrCa.[30] The variety of targeting moieties available for use demonstrate the opportunities for collaboration and broad range of impact for this field of research. The peptide, shown in Figure 4, has been synthesized in our lab and is the focus of a related TMIA project.

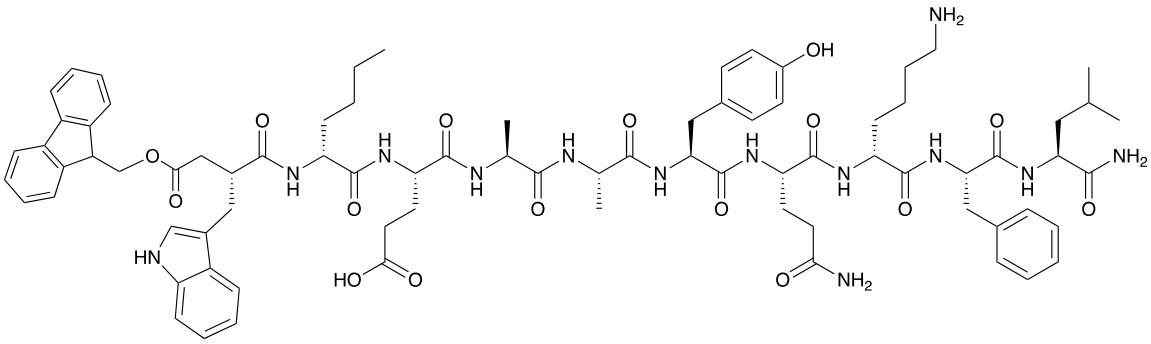

Figure 4. Structure of Breast cancer peptide 18-4.

1.5 Molecular Imaging Methods

In addition to targeting the cancer cells, the method of imaging used must be considered in the future of cancer diagnosis. Each imaging method – PET, MRI, photoacoustic (PAI), CFM, and others, offers its own merits and suffers its own shortcomings. For example, CFM produces a very sharp three-dimensional image, but the depth of the image below the surface of the sample is limited to about 100μM, which limits this technique to in-vitro imaging.

To counter the shortcomings associated with each method of imaging, dual-modal (sometimes also called bi-modal) molecular imaging has gained some ground in recent years.[31,32] Dual-modal imaging involves the combination of two imaging techniques; the images may be obtained simultaneously using specialized

instrumentation, or the images may be digitally fused in the post-processing stages. The imaging techniques for dual-modal methods are selected to complement each other – that is, it wouldn't be overly helpful to combine two methods of imaging which both provide structural information, but combining structural details with mapped biological activity would very practically applicable. In the field of cancer imaging, simultaneous PET/MRI is presented as a dual-modal method of choice, and will be further explored below.[17,33,34]

PET provides physiological data for a variety of biological functions, such as blood flow, oxygen use, and sugar metabolism.[35] Although PET is sensitive to the presence of even very small amounts of radiotracer in a sample, this method does not provide significant structural resolution for the sample. It is not immediately clear from a PET scan which tissues are present or whether the anatomy is at all abnormal.

Therefore, it is useful to fuse PET images with structural information, such as images obtained by CT or MRI, for a more complete analysis of cancerous cells present within the patient. An example of such an image overlay is shown in Figure 5**.** Structural tissue information from MRI is compared to physiological data from PET to provide a more specific, more accurate diagnostic of smaller cancerous tumors.

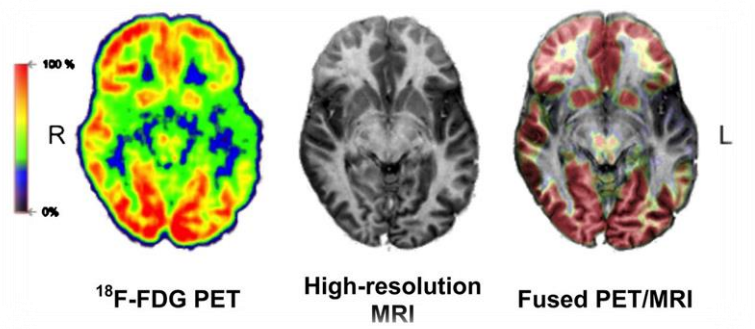

Figure 5. An example of individual PET and MRI scans, and the fused image of the two scans, showing the high-resolution structure and the sensitive biological activity information which can be obtained from such an image.[36]

The integration of PET with either CT or MRI can be done with in-line systems (which produce both images simultaneously) or by obtaining the images from two separate instruments and fusing the images in post-processing. However, if images are to be fused during post-processing, it is important for the images to be properly aligned, so that the signal in the final image is correctly mapped to the body. Improper alignment can result in a number of problems, including misled assignment of surrounding tissues or incorrect diagnosis regarding the size of the tumors. If the images are overlaid accurately, however, they can be most useful to the diagnostic team. Therefore, validated methods for the accurate overlay of MRI and PET images are essential for diagnostic techniques associated with dual-modal imaging.[37]

PET/CT imaging methods are commonplace in hospitals today after an in-line method for simultaneous bi-modal imaging was introduced in the late 1990s.[38] Today, the use of PET/MRI is considered a potential competitor for PET/CT, because MRI provides a comparable structural resolution when compared to the data obtained by CT, and because MRI does not involve high-energy x-ray exposure.[39–41] PET/MRI has also been shown to offer higher diagnostic accuracy when directly compared to PET/CT.[34]

The primary factor currently preventing a complete transition from CT to MRI is a financial one. PET/CT and PET/MRI provide comparable results at the moment, so it is difficult to justify the expensive change from one to the other. However, MRI has been shown to be more sensitive than CT in some situations, such as soft tissue imaging, and further research and improvements to PET/MRI systems may encourage such a switch.[42,43]

1.6 Magnetic Resonance Imaging

1.6.1 A Simple Treatment of MRI Theory

MRI is a non-invasive method of molecular imaging which uses magnetic fields to manipulate nuclei that have a magnetic spin.[44] These nuclei include ^{1}H, ^{2}H, ^{13}C, and ^{14}N, among others. During an MRI scan, a strong (1.5 to 3 Tesla) magnetic field (B_0) is applied along the designated z-axis, which aligns the nuclear spins to be parallel with that B_0 field. An RF pulse rotates the nuclei 90 degrees into the xy-plane, perpendicular to B_0. While the nuclei are in this position, there is net transverse magnetization within the sample, and the nuclei precess at their Larmor frequencies as determined by the chemical environment; this is related to the familiar chemical shift observed in NMR spectra (Figure 6). The precession and the transverse magnetization induce a current in an RF coil. This induced current is recorded as a signal in the image. However, because a large magnetic field is still in place, the nuclei will eventually return to their thermal equilibrium and realign with the B_0 field, at which point the induced current in the RF coil decays and, with it, the signal.

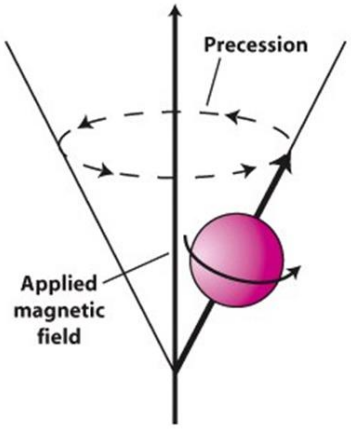

Figure 6. Representation of the precession of a nucleus about the applied B_0 magnetic field..[45]

The process by which the nuclei return to their thermal equilibrium positions is known as relaxation. There are two different relaxation processes to consider in MRI: T_1 and T_2. Both of these affect the strength of the signal produced in the image. The longitudinal relaxation time (T_1) is a measure of how quickly a nucleus returns to its equilibrium alignment with B_0 after the application of an RF pulse, which rotates the nuclei spins by 90 degrees. The spin-spin relaxation (T_2) is the process by which the net transverse magnetization decays to zero, which occurs because not all spins within the sample precess at exactly the same frequency, but are, rather, slightly out of phase, so after many precessions, the spins will 'cancel' in the transverse direction and the net transverse magnetization will eventually be zero (Figure 7).

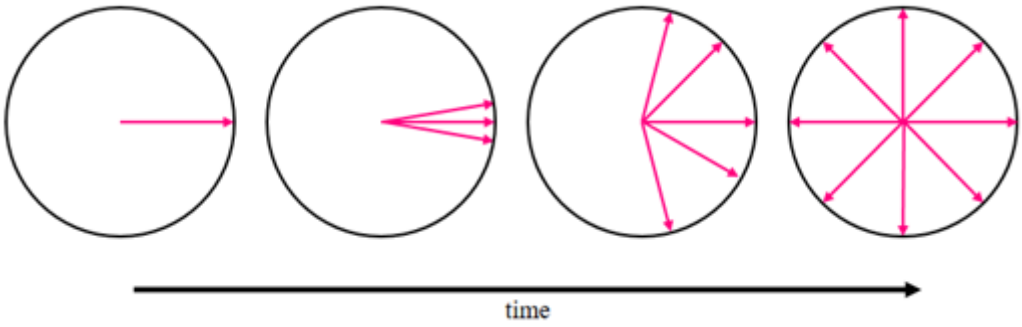

Figure 7. Representation of the T2 decay process, showing how the many spins in a sample dephase over time after the initial excitation by an RF pulse to ultimately produce a net magnetic spin of zero.

Those relaxation processes, T_1 and T_2, are measured according to the time it takes the signal from a sample to decay by a factor of e, and are affected not only by the tissues present in the sample, but also by the parameters used for the acquisition of the image (which are beyond the scope of this background discussion). T_1 and T_2 can then be considered as rates by taking the reciprocal of the relaxation time for each

process. The longitudinal relaxation rate, R_1, is $1/T_1$, and the spin-spin relaxation rate, R_2, is $1/T_2$.

1.6.2 MRI Contrast Agents

In the field of MRI, contrast agents (CAs) are commonly used to increase the signal generated by different types of tissues. There are two general classes of CAs for MRI: ferromagnetic and paramagnetic. Ferromagnetic CAs distort the magnetic field surrounding the CA, which have the primary effect of shortening the T_2 time for nearby nuclei. Common ferromagnetic (or T_2) CAs are based on iron nanoparticles. Paramagnetic (or T_1) CAs, on the other hand, have unpaired electrons which primarily increase the rate of T_1 relaxation of the nuclei in the surrounding tissue.

Gadolinium (III) is the most frequently used paramagnetic CA due to its seven unpaired electrons (for a total electron spin of 7/2). CAs are considered in terms of their relaxivity, which is the extent to which a specific CA affects the relaxation rate of the tissues per unit concentration of CA, per equation (1), where n = 1 or n = 2, depending on which relaxation mechanism is being investigated, r_n is the relaxivity of the CA, T_n is the relaxation time for the nuclei of interest when a certain concentration of CA is present in a treated sample, T_0 is the relaxation time for the untreated sample when no CA is present, and [CA] is the concentration of CA present in the treated sample. The relaxivity r_n has units of $s^{-1}mM^{-1}$.

$$r_n = \left(\frac{1}{T_n} - \frac{1}{T_{n0}}\right) \div [\mathrm{CA}] \qquad (1)$$

The DOTA chelating group and other cyclenes are frequently used for both MRI and radioisotope imaging methods (such as PET).[46] Many metals used in imaging, such as Gd(III), are safe when chelated but can have problematic effects on the body if they

are released from the chelating group.[47] For example, Gd(III) has a similar size to Ca(II), and therefore competes with Ca(II) in biological processes.[48]

It is therefore necessary to develop highly stable complexes to protect the body from the Gd to be used during imaging. DOTA-metal complexes have been shown to be kinetically stable, and Gd-DOTA is particularly kinetically stable, so DOTA-type complexes are favored for MRI contrast agents, and are available as commercial CAs (Figure 8).[31] In the end, a kinetically stable targeted MRI contrast agent with a high relaxivity could be used in much smaller doses, and the amount of gadolinium which a patient is exposed to would be cut drastically while still providing useful results to their treatment team.

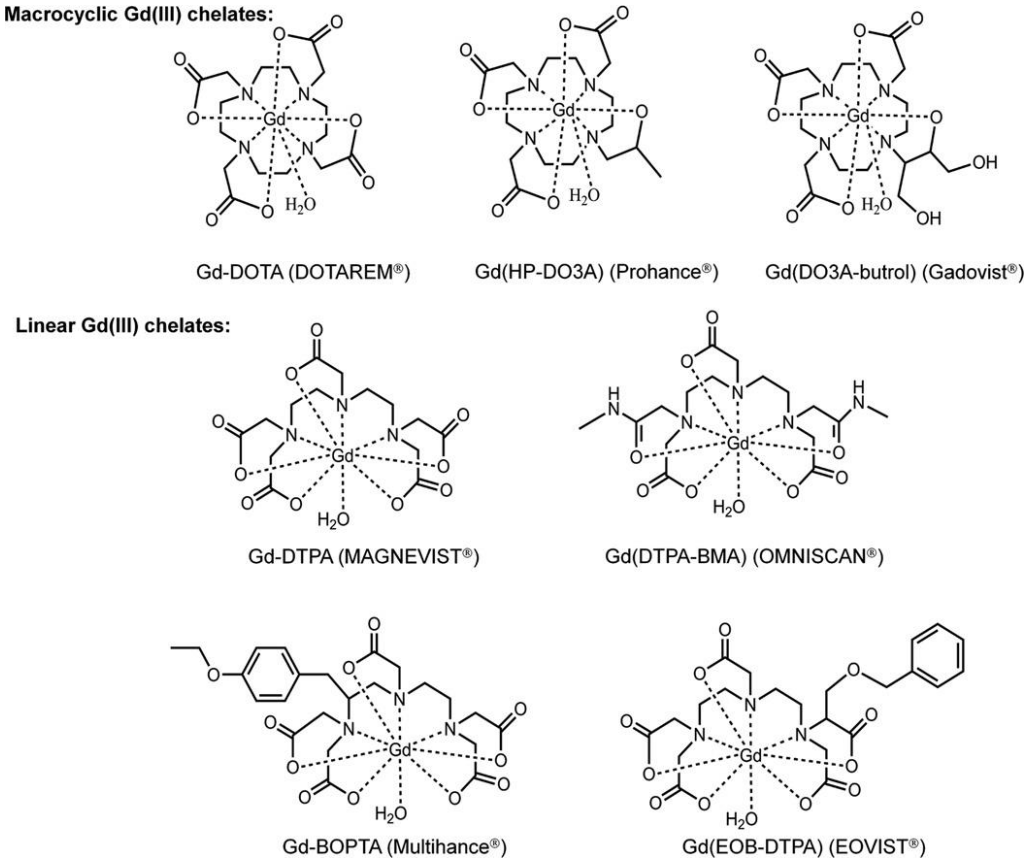

Figure 8. A selection of commercially available Gd-based CAs.[49]

1.7 Positron Emission Tomography

1.7.1 Theory and Physics of PET

PET is based on the use of radioisotopes which will undergo the process of positron decay, also known as beta plus (β^+) decay.[50] Unlike MRI, which can be done without a contrast agent, PET is not possible without the introduction of a suitable radioisotope into the sample. Commonly used radioisotopes for PET include ^{15}O, ^{18}F, ^{11}C, and ^{13}N, because it is easy to incorporate them into organic molecules that are metabolized by the body and, by that process, track the metabolic processes in a region of interest.

During the process of positron decay, a proton within the unstable nucleus is converted into a neutron, and a positron, bearing the mass of an electron and the positive charge of a proton, is emitted.[51] The energy of the positron will vary depending on what type of nuclei has decayed: a positron from ^{18}F decay will most often have around 200keV of energy (and a maximum of 630keV), while a positron from ^{68}Ga positron-decay has roughly three times that. The positron will travel some small distance, on the scale of millimeters, while it loses kinetic energy – in ^{18}F decay, this is an average of 0.6mm, with a maximum of 2.4mm; for ^{68}Ga, an average of 2.9mm and a maximum of 8.2mm. When the positron has approximately come to rest, it undergoes annihilation with an electron, and this annihilation releases two photons with 511keV at 180 degrees from each other, whose locations can be recorded by detectors within the instrument (Figure 9).

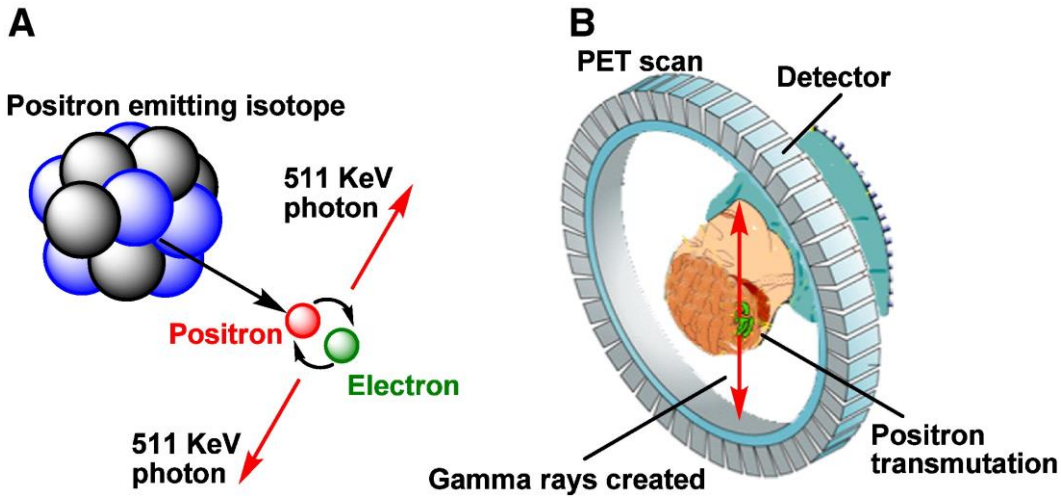

Figure 9. Elementary graphic explanation of theory behind PET.[52]

1.7.2 Radionuclide Imaging Agents

^{18}F has been commonly used as a radionuclide for PET in the form of ^{18}F-fluoro-2-deoxy-glucose (^{18}F-FDG). In this form, it is particularly useful for cancer imaging, because the similarities to glucose cause the imaging agent to accumulate in cancerous tumors more so than in healthy tissue.[53] However, there are a number of issues to deal with when using ^{18}F-FDG, including difficulties during the synthesis of the radionuclide and the short lifespan of the radioisotope.

Because of this shortcoming, ^{64}Cu has gained attention within the last 30 years for use as a radionuclide for PET.[54] Copper has a number of radioactive forms, each of which has a different half-life and produces positrons with different amounts of energy. ^{64}Cu has a half-life of about 12.7 hours, which is significantly longer than several radioisotopes that have been used for PET in the past, including ^{15}O, ^{18}F, ^{11}C, or ^{13}N, which have half-lives on the scale of minutes (Table 1). This characteristic makes ^{64}Cu a more useful candidate for imaging biological processes which make take longer to occur, and, when coupled with a targeting moiety, will provide more time for the imaging agent to accumulate at the desired area.

Additionally, the coordination chemistry of ^{64}Cu is well understood and can be taken advantage of to produce an imaging agent that is stable *in vivo*. Although ^{64}Cu undergoes multiple types of radiodecay and not all are useful for PET, this is less of a problem than it might first seem to be, due to the sensitivity of PET. Also note that ^{68}Ga is also often used as a nucleus for PET, despite the fact that it decays by positron emission less than 10% of the time.

Isotope	**Half-life**	**β+ energy**	**Odds of β+ decay**
C-11	20.4 min	0.385 MeV	99.8%
N-13	9.97 min	0.492 MeV	100%
O-15	122 seconds	0.735 MeV	100%
F-18	110 min	0.250 MeV	100%
Cu-64	12.7 hours	0.278 MeV	17.9%
Ga-68	68.1 hours	0.836 MeV	8.79%

Table 1. Summarizing some useful properties of isotopes used in PET as radionuclides for imaging.[55]

It is important to ensure that the ^{64}Cu is securely held in place in the TMIA before it is exposed to any *in vivo* conditions. While copper is an essential nutrient for humans, it is still possible for too much copper to accumulate in the body and interfere with certain biological processes. Particularly when a radioactive form of copper is being used, it is most undesirable to allow the radioactive copper to accumulate in any part of the body. Additionally, if the copper is removed from the chelating group in the TMIA, the imaging agent is no longer effective for PET. DOTA and DOTA-type derivatives are frequently used as chelating groups, and Cu^{2+} chelates of DOTA and its derivatives have been shown to be kinetically stable at *in vivo* conditions for radiopharmaceutical work.[56]

Because we do not have access to radioactive metals, we utilized the cold isotopes of each respective metal in our studies – that is, we used the stable $^{63}Cu^{2+}$ and $^{65}Cu^{2+}$ in our studies, rather than the radioactive isotope ^{64}Cu. However, because the size of the metals will not be greatly affected by that difference, the stability of the product and relative reaction rates are expected to be the same for both the cold and radioactive isotopes.

Chapter 2. Experimental Approach

2.1 Modular Synthetic Approach to TMIA Synthesis

Our group is interested in a peptide-based modular approach to synthesizing imaging agents. Imaging or contrast modules for each imaging method are synthesized, and the relevant imaging and targeting modules are coupled together.[57] An amino acid backbone such as lysine is favorable due to its primary amine side chain. This functional group is easily coupled to a chelating group (such as DOTA) for chelation of a metal that is useful for imaging. Peptides are preferable over original small molecules that could possibly be designed. They have known advantages in medicinal chemistry due to their relatively small, compact structures and their bioavailability and biostability.[58] Because the reagents and coupling mechanisms for peptides are fairly well known, we can focus efforts on developing new TMIAs, rather than developing new reactions.

Ultimately, the goal of this work was to prove the usefulness of our modular method by its application to the synthesis of two unique TMIAs: one for MR imaging of prostate cancer, and one for simultaneous MRI and PET of cancerous cells overexpressing the $\alpha_v\beta_3$ integrin.

Our method involves synthesizing each module of the TMIA on a lysine backbone before constructing the TMIA from C terminus to N terminus, as is the norm for peptide synthesis. In this case, for the synthesis of a TMIA for PET/MRI of some cancer, the synthesis proceeds generically as shown in Figure 10. Each of the modular components (MRI contrast module, PET imaging module with placeholder, linker, and targeting moiety) are either synthesized and purified in-house, or purchased from a commercial source, and then coupled to yield the penultimate product in the synthesis.

The last step is a simple transmetallation to replace the La^{2+} with Cu^{2+}, where the use of Cu^{2+} in our lab functions as a substitute for a radioactive metal.

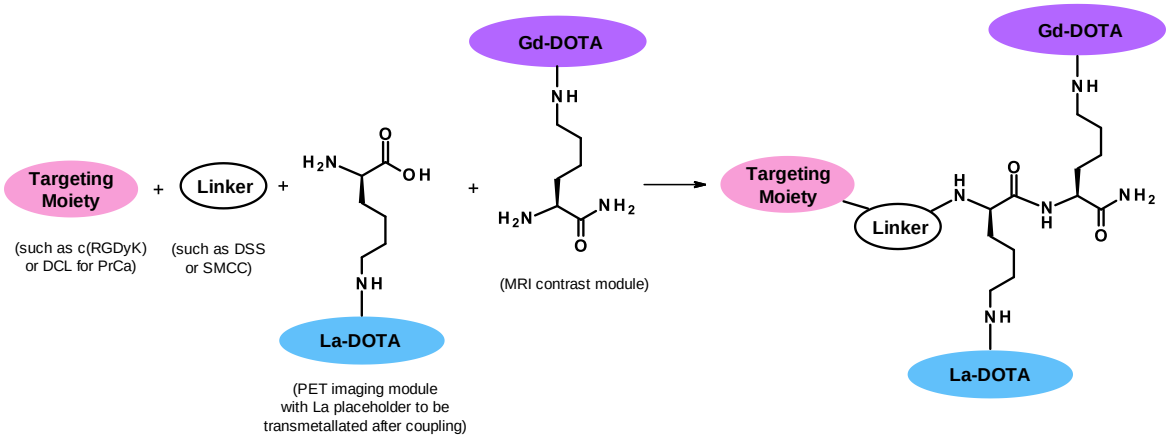

Figure 10. General schematic for synthesis of a dual-modal TMIA

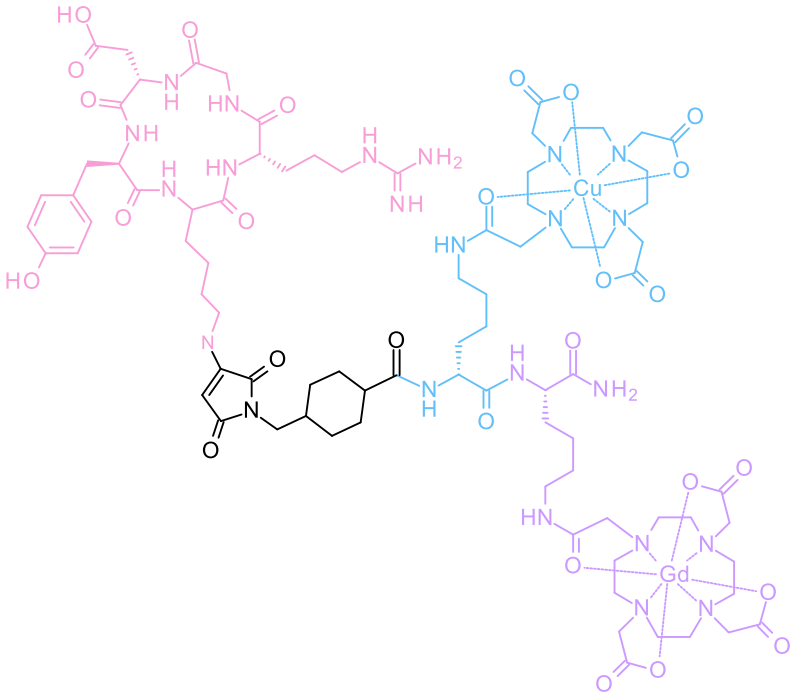

Figure 11. Color-coded structure for one of the final TMIA products, c(RGDyK)-SMCC-dK(DOTA-Cu)-K(DOTA-Gd)-NH2, useful for targeted PET-MR of cancer.

A specific TMIA for use in dual-model MRI/PET of cancer is shown above (Figure 11). This particular TMIA features the MRI contrast module in purple (Lys(DOTA-Gd)-NH_2), the PET imaging module in blue (dLys(DOTA-Cu)-OH), a carbon linker in black (SMCC), and a commercially-available targeting group in pink (c(RGDyK)).

In the world of peptide synthesis, there are important choices to make regarding the methods available. These include convergent versus linear synthesis, and solution-phase versus solid-phase synthesis. Linear and convergent methods of synthesis refer to the order in which the peptide is built. In a linear method, the peptide is built from right to left. The components are connected by building peptide bonds, which involve a terminal N on the first component and a terminal C on the second (from right to left). For a specific dual-modal TMIA of interest, the linear synthesis would proceed according to Scheme 1. In a convergent method of synthesis, the synthesis follows Scheme 2. Traditionally, our group has focused on a linear method when building the final peptide-based TMIAs, but convergent methods have provided better yields in certain cases.

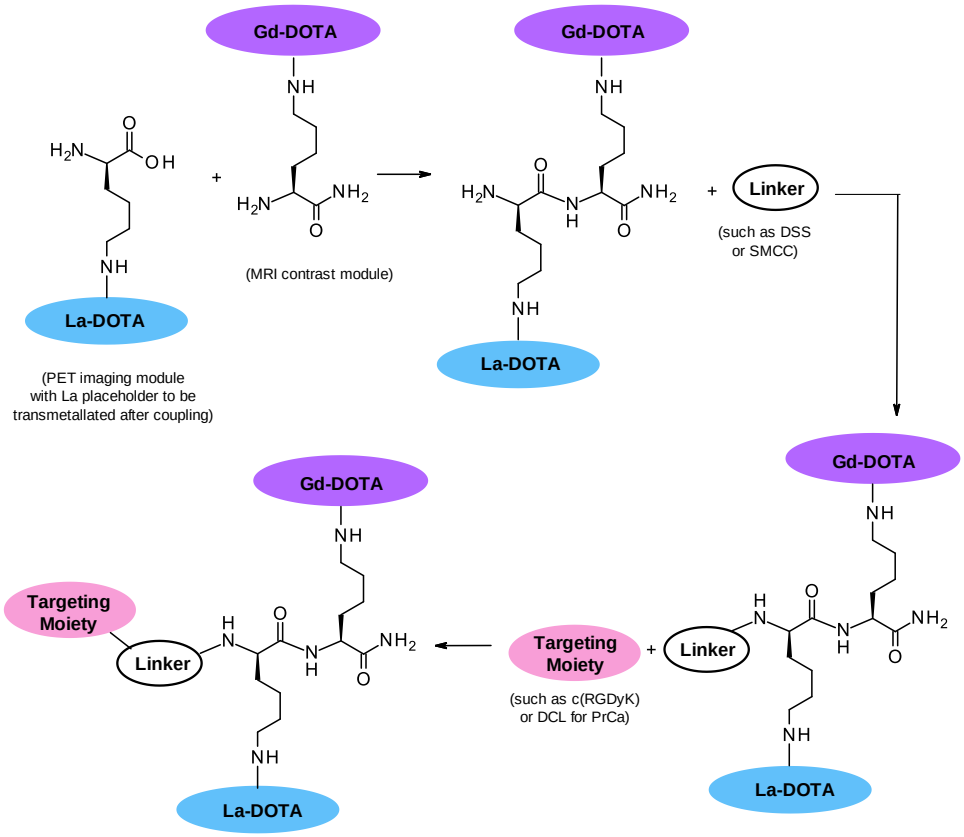

Scheme 1. Schematic for linear method of dual-modal TMIA synthesis.

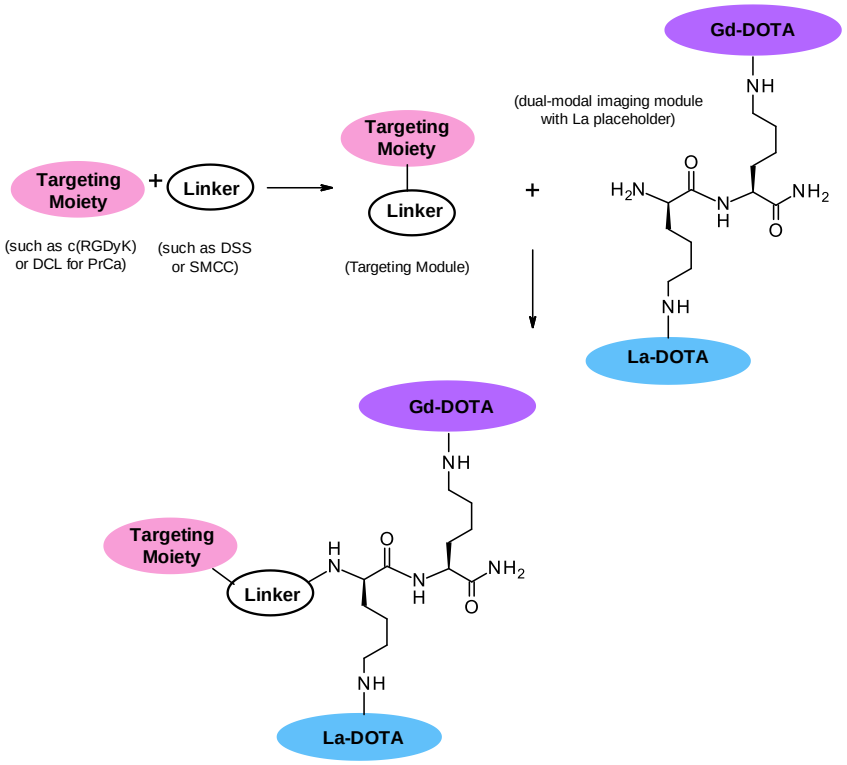

Scheme 2. Schematic for convergent method of synthesis for dual-modal TMIA.

The decision to use solution-phase peptide synthesis methods rather than solid-phase methods was made based on a number of factors. Solution-phase synthesis tends to be more useful for shorter peptides, and the dual-model imaging agent modalities of interest involve just two lysine groups. Additionally, solid-phase methods require a linear synthesis of the final product. Solid-phase methods also require a specific type of resin for the peptide synthesis, which can become costly, and increases the number of factors that must be considered during synthesis, whereas solution-phase synthesis requires only a suitable organic solvent as a medium.

Solid-phase synthesis is often preferred because the intermediate products do not need to be removed from the resin and purified; rather, the final peptide is cleaved from the resin only after synthesis is complete. In this situation, that feature is not necessarily a benefit, because we want to focus on the modality of the synthesis, and how simple it can be to substitute in a different imaging contrast agent or targeting group during the procedure. For example, we can potentially synthesize a dual-modal imaging agent and linker (DSS-dK(DOTA-La)-K(DOTA-Gd)-NH_2) in large quantities, and later couple a small sample of this compound to different targeting groups.

2.2 Novel use of Metals as DOTA-Protecting Groups

Imaging and contrast agents have been in use since the eighties – altogether, a relatively new field of science. But the idea of targeting the imaging or contrast agents to a specific type of cell is newer still. The synthesis of such agents, then, is a developing area of chemistry. Even so, there are already somewhat ‘standardized’ methods of synthesis for targeted molecular imaging agents.

Because a metal is required for imaging methods such as MRI and a radioactive isotope is required for PET, the addition of a metal to the compound and its chelation into a group such as DOTA is a very important step. Current methods in the literature generally consider chelation as the last step in the synthesis of an imaging agent. Our group, however, has developed a different procedure, in which the metal is chelated into the DOTA-type macrocycle in the early stages of synthesis.

By chelating the metal early on in the synthesis, the metal itself functions to protect the chelating group from undesirable side-ructions: DOTA and similar chelating groups contain reactive functional groups (i.e., carboxylic acids and amines). Left unprotected, these groups are susceptible to further reactions during the synthesis. Most methods in the literature rely on protecting groups such as t-butyl groups to protect these carboxylic acids; the protecting group is removed in the latter stages of synthesis by treatment with a strong acid like TFA before the metal is chelated. This modular method avoids harsh deprotections and the associated risk of decomposition of the TMIA under those conditions. We have found that the metal is just as capable as traditional protecting groups of shielding the DOTA group from further chemistry during synthesis.

Chelating a metal at the beginning of the synthesis is easily said, and for stable isotopes (i.e. $^{157}Gd^{3+}$ for MRI) it is easily done. However, PET requires a radioactive isotope, and it is not feasible to chelate a radioactive metal at the beginning stages of a long and arduous synthetic process. The metal would begin decaying from the time of its initial chelating and would no longer be useful as a PET imaging agent by the time the TMIA had been fully synthesized.

Fortunately, our group has developed a workaround for this issue: the use of a placeholder metal. Metals of similar size to Cu^{2+} are useful as placeholders within the

DOTA group. That is, the placeholder metal is chelated in to the DOTA macrocycle in the early stages of synthesis, and functions as the protecting group until the end stages of synthesis. Then, the placeholder metal is displaced in an aqueous acidic solution, and the desired metal (i.e. Cu^{2+}) is introduced and takes its own place in the DOTA group.

Because the placeholder metal must be removed from the DOTA without destroying the rest of the TMIA, it is important to ensure that the metal is not too securely chelated – but it must also be stable enough to remain in place during the synthesis of a TMIA. Our hypothesis for this work was based on ionic radius: smaller metals, such as Gd and Cu, were expected to chelate strongly with the DOTA group, while larger metals would be less stable within that group. Due to the lanthanide contraction phenomenon, such as La^{3+} or Ce^{3+} are large enough to be significantly less stable within DOTA than smaller metals such as Gd^{3+} or Cu^{2+}. Our aim was to find mild acidic conditions to displace the larger lanthanides without affecting the smaller ions (such as Gd^{3+}). We found several early literature studies which supported our hypothesis that mild acid would displace metals on the left of the lanthanide row more easily than those towards the right. [59–61]

After conducting kinetic studies of our own, we settled on La^{3+} as a favorite. The La-DOTA group holds up well to the further reactions necessary for TMIA synthesis, but La^{3+} is also readily displaced from the DOTA group in a solution of about 0.1M TFA. Additionally, Gd^{3+} is strongly chelated by DOTA and is not displaced from the chelator under those conditions, making this suitable for use in di-metal TMIA synthesis (Figure 12).

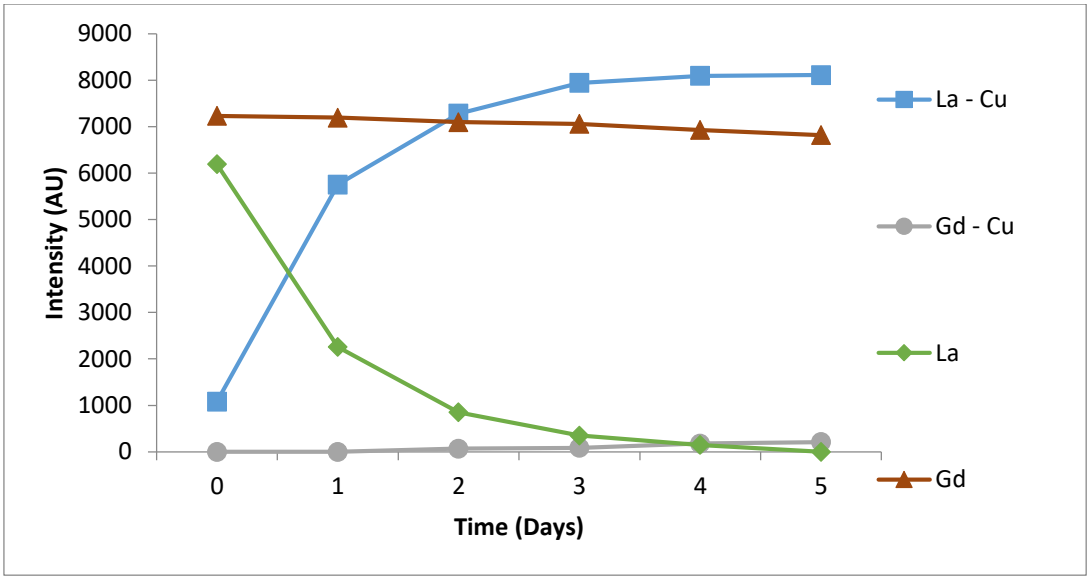

Figure 12. Graph showing the displacement of La^{3+} by Cu^{2+} in a DOTA chelator in 0.1M TFA over several days, as well as the stability of Gd-DOTA in those same conditions. Data points were obtained by HPLC-UV analysis, and the intensity was taken from the area under the curve for the UV-absorption of each compound.

2.3 Evaluation and Analysis of Compounds

Purified products are characterized by HMRS for an exact mass, and by NMR experiments for further confirmation of structure. T_1 relaxation experiments are run on a 43MHz NMR spectrometer used to determine the relaxivity of the targeted contrast agents for use in MRI. These values can then be approximately compared to commercial MRI CAs, such as Gd-DOTA (trademarked as Dotarem).

Unfortunately, we have no means here in our lab of testing our compounds in-vivo as PET or MR contrast agents, so any testing on that front requires future collaborative efforts at another site.

We are able, however, to verify the ability of a metal-containing TMIA to target a specific type of cell through CFM, through the addition of a fluorescent NIR dye imaging module to the TMIA, yielding a dual-modal TMIA. In a previous dye-based project in our lab, we developed a TMIA containing both and MRI module and an NIRF

dye, Cy5.5, that effectively utilized c(RGDyK) as a targeting moiety. This TMIA was shown to selectively target the cells of interest, as evidenced by our collaborative work with Dr. Irene Evans's lab at RIT, and their CFM imaging of A249 lung cancer cells treated with that TMIA (Figure 13).

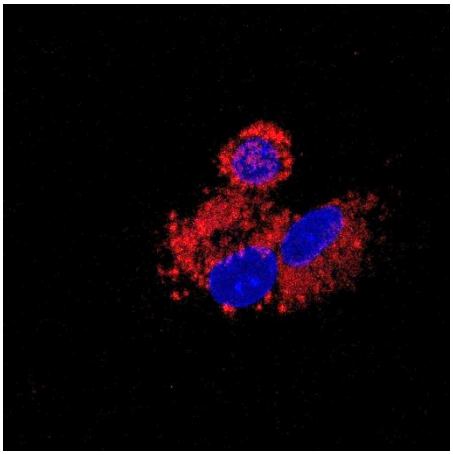

Figure 13. CFM image of A249 lung cancer cells treated with NucBlue and a previously synthesized TMIA for MRI and fluorescence of cancer cells, using the c(RGDyK) targeting peptide. Cell nuclei are stained blue; the TMIA appears red due to fluorescence.

Chapter 3. Results and Discussion

3.1 Optimization of One-Pot Reactions for Synthesis of Imaging Modules

In our group's initial approaches to the DOTA-chelating imaging modules, a multi-step synthesis was developed (Scheme 3). However, the commercial DOTA-$OtBu_3$ used here was expensive, and the yields were not sufficient to justify the cost of the starting materials. Therefore, it was crucial to develop a more economical and efficient method of synthesizing these modules.

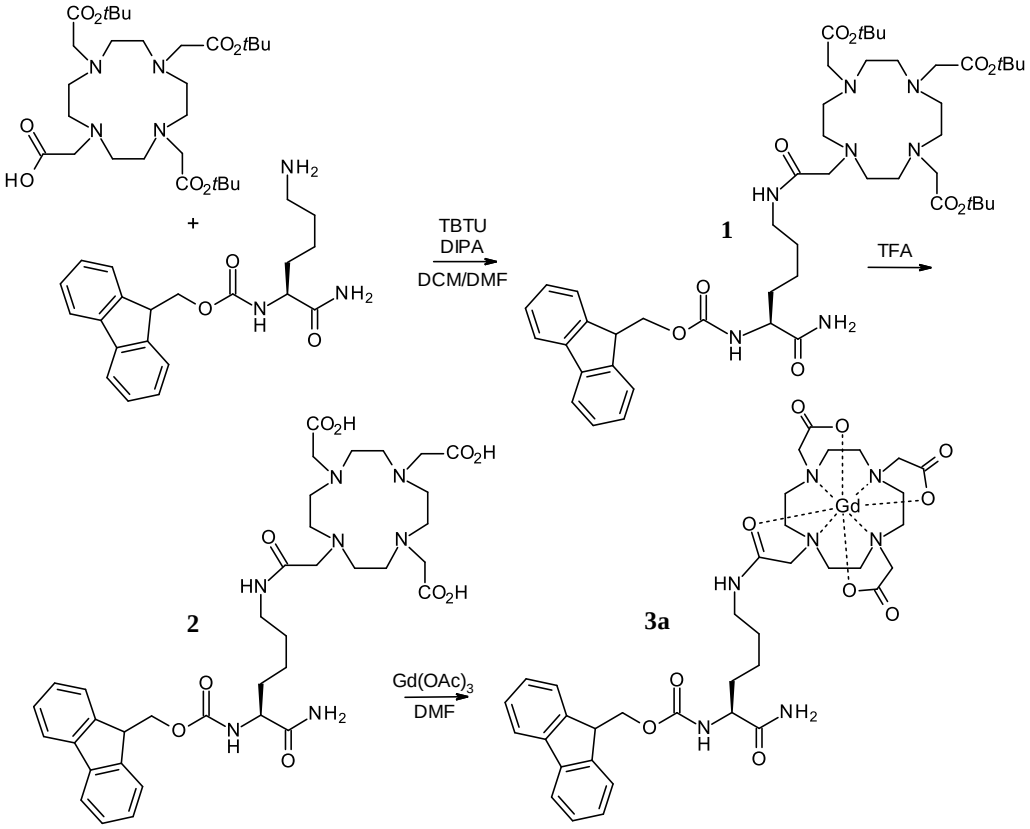

*Scheme 3. Multi-step procedure for synthesis of Fmoc-Lys(DOTA-Gd)-NH_2 , **3a**.*

To this end, a one-pot reaction was developed in our lab by former students (Scheme 4). In this method, the commercial unprotected DOTA was coupled to the

lysine side chain. However, the yield from this procedure was lower than expected. Therefore, one of the early goals for this project was to improve the yields of the one-pot reaction.

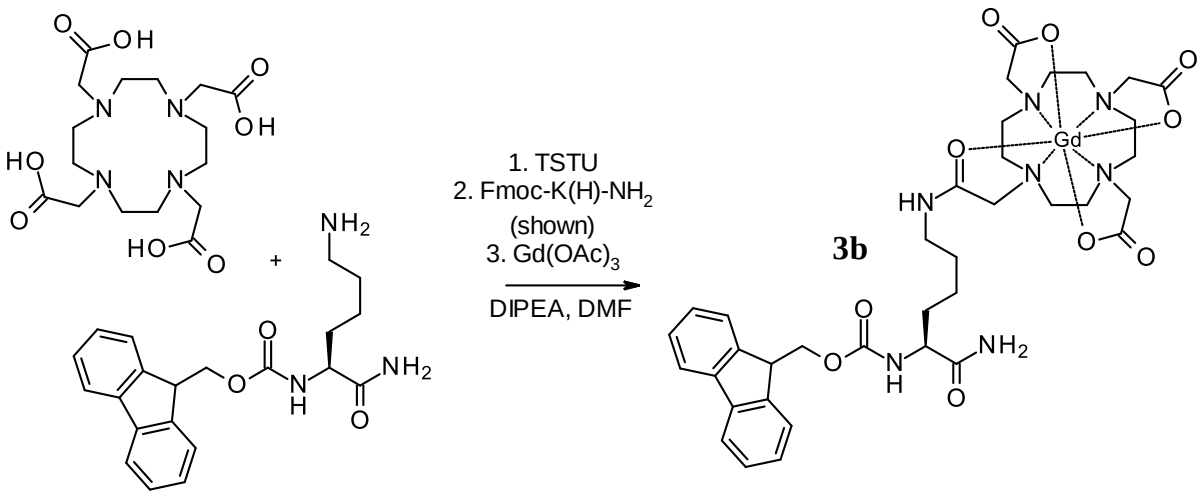

Scheme 4. One-pot synthesis of Fmoc-Lys(DOTA-Gd)-NH_2, ***3b****.*

After running both sets of reactions a number of times to synthesize the MRI contrast module, Fmoc-Lys(DOTA-Gd)-NH_2 (**3**), (Scheme 3 & Scheme 4), we determined that any loss in overall yield in the one-pot method was outweighed by the reduced reaction & purification time investments required. The initial multistep synthesis requires at least three days to obtain the final product, whereas the more economical one-pot reaction can be run in a morning, and the purified product isolated that afternoon.

While focusing efforts on the one-pot reaction, we found that certain modifications increased the yield of the reaction, and decreased the production of di- and tri-substituted DOTA groups (Scheme 5). The use of a dilute reaction solution, heating the initial DOTA-OH in organic solution (to promote solvation), the slow

addition of the peptide coupling reagent TBTU (to favor mono-substitution on the DOTA), the slow addition of lysine, and allowing the reaction to run for no more than two or three hours all proved beneficial.

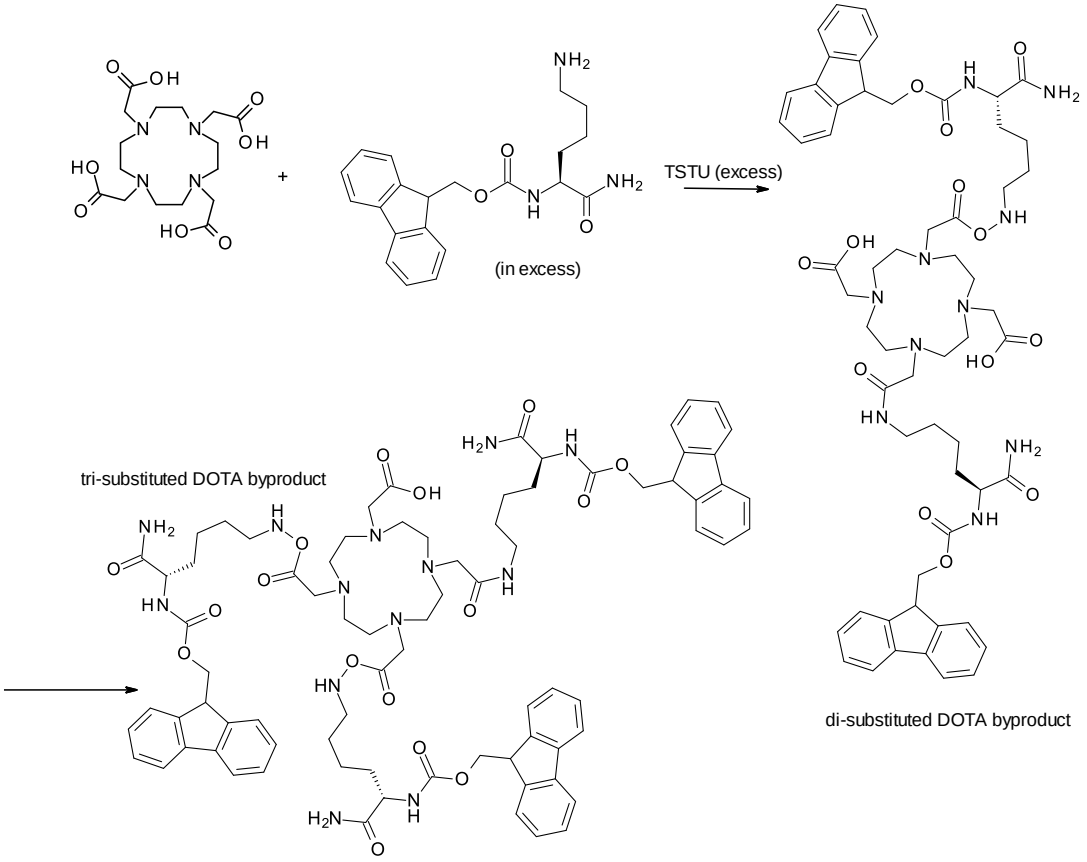

Scheme 5. Undesirable di- and tri-substituted byproducts.

Because the MRI and PET imaging modules are so similar, varying only in the metal used and the form of lysine used, the methods for synthesis are remarkably similar, as well. Improvements in method **3b** also resulted in improvements for the synthesis of Fmoc-dLys(DOTA-La)-OH (**5**), shown in Scheme 6.

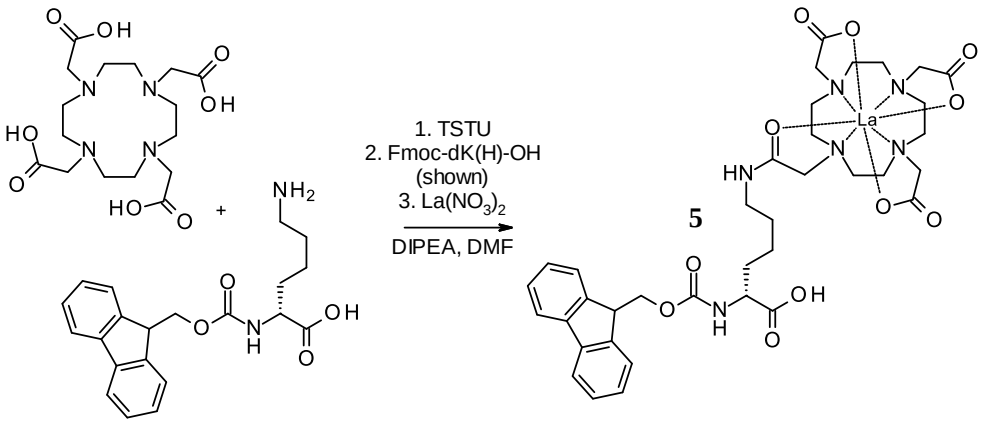

*Scheme 6. One-pot synthesis of **5**, PET placeholder module.*

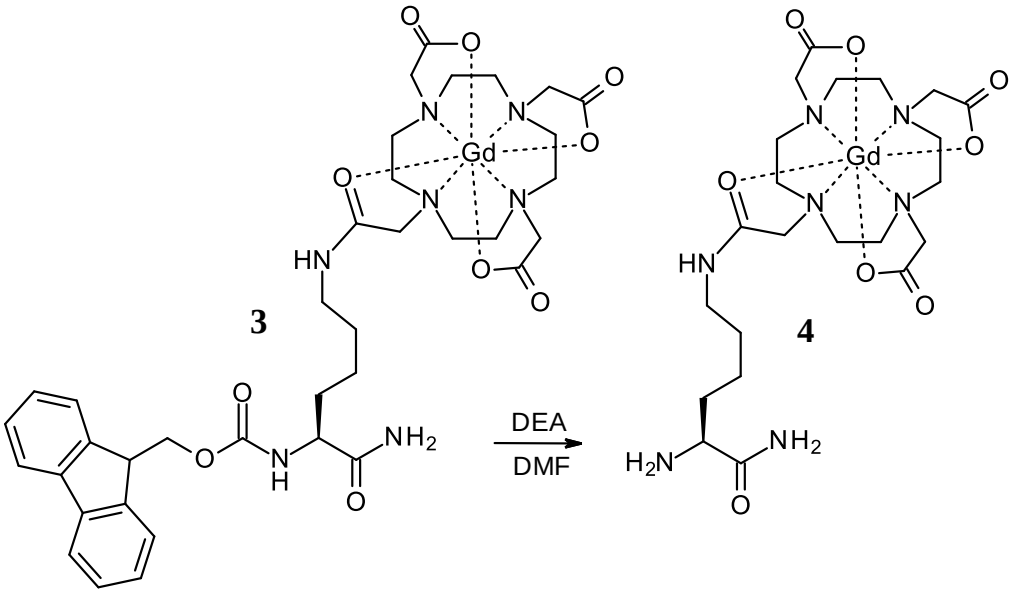

*Scheme 7. Fmoc deprotection of **3** to yield H-Lys(DOTA-Gd)-NH_2, **4**.*

3.2 Simple Fmoc Deprotections

Removal of the Fmoc group exposes the primary amine of the peptide backbone for coupling chemistry in the next step. The Fmoc deprotection of **3** was simple enough (Scheme 7); treatment with diethylamine in organic solution provided reproducible results and yields of 90% and above. Initially, purification was done by liquid-liquid

extraction, with the H-K(DOTA-Gd)-NH_2 product (**4**) found in the aqueous layer and the Fmoc byproduct taken up by the ethyl acetate organic layer. However, on small scale reactions of 20mg and below, we were concerned some product might be lost by this method, so we decided that triturating the crude product with ethyl acetate, centrifuging, and decanting the organic solvent was sufficient to remove the Fmoc byproduct.

3.3 Troublesome Dimetal Peptide Coupling Reactions

The truly troublesome reaction was the coupling of the two imaging modules to yield a di-metal imaging module. Initially, this reaction was run according to Scheme 8. However, this resulted in disappointing yields. The product was often not able to be isolated, nor did the reaction run to completion according to the HPLC-MS data acquired.

A number of different reagents for were considered in an attempt to solve this problem (Figure 14). The use of different organic bases or peptide coupling reagents as found in the literature failed to provide different or improved results.

After numerous failed attempts, we began to experiment with a readily available commercial amino acid (Fmoc-dAla-OH, Figure 15) to couple to the MRI contrast module. This way, at least, large quantities of valuable imaging modules were not wasted when the reactions failed.

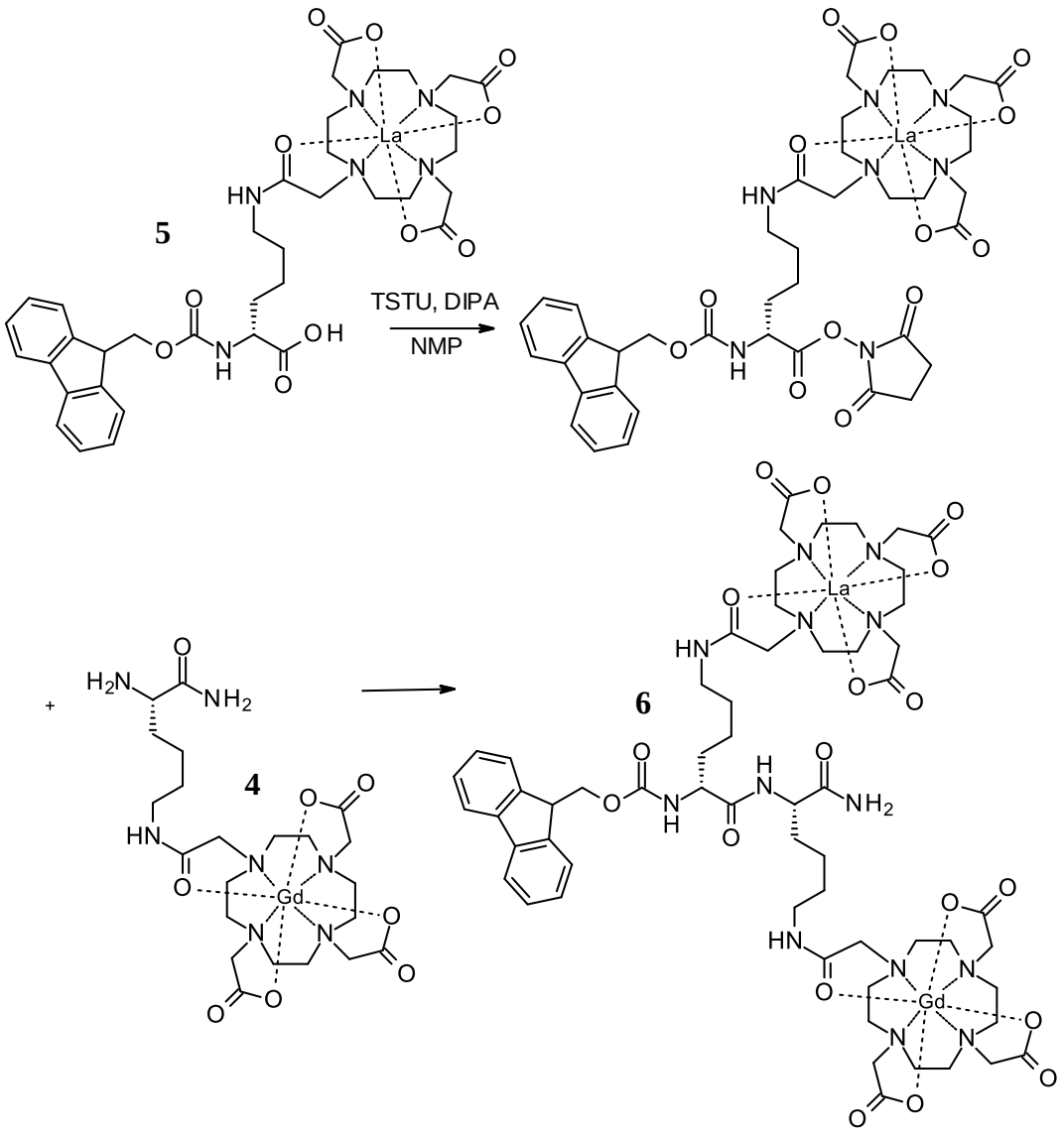

Scheme 8. Initial method for peptide coupling to yield dual-modal imaging agent.

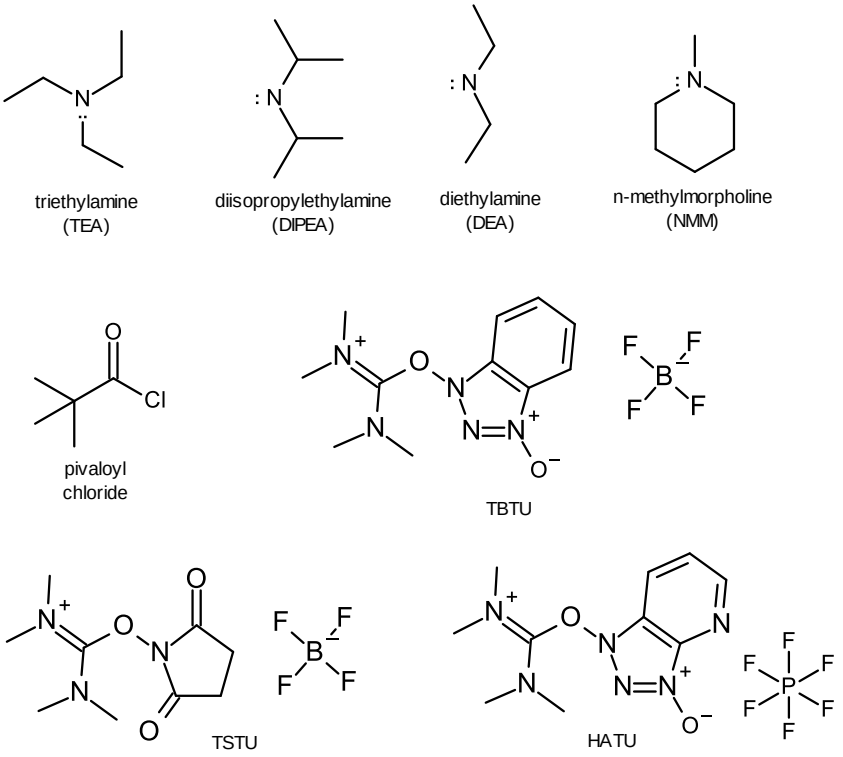

Figure 14. A selection of organic bases (top row) and peptide coupling reagents (lower two rows) which were considered.

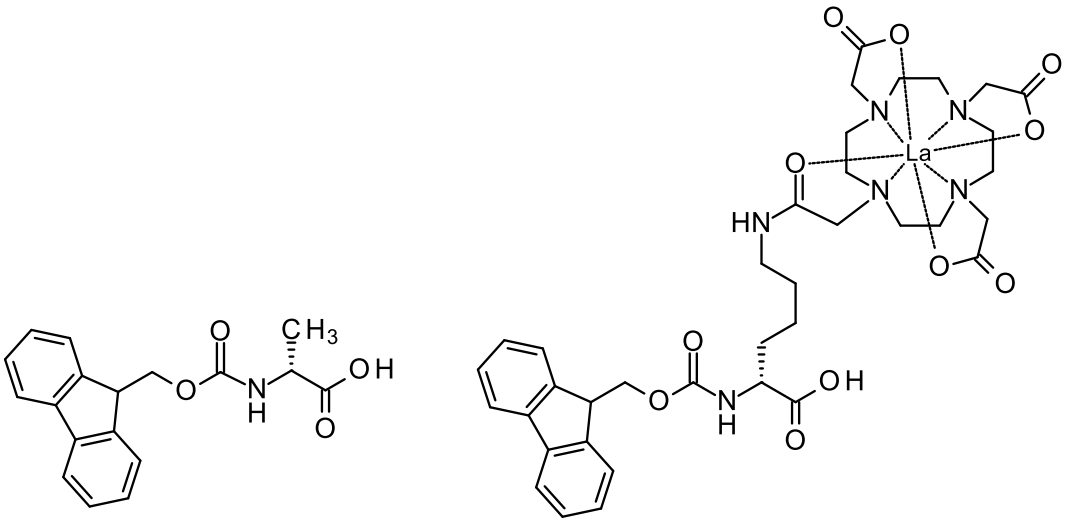

*Figure 15. Fmoc-dAla-OH (left) and Fmoc-dLys(DOTA-La)-OH (**5**), right.*

Pivalyl chloride presented itself as a possible solution. Coupling reactions using pivalyl chloride as the coupling agent yielded good product, and the reaction run to completion with the trial amino acids according to the data from the HPLC-MS. Upon replacing the Fmoc-dAla-OH with the PET imaging module, however, the results were significantly less impressive.

It was back to the drawing board again: we needed to more thoroughly investigate what the basics of the reaction were and which factors (reagent, solvent, time, temperature, phase of the moon) were the most important. To test the activation of the acid module by activating agents such as TSTU, a method was developed in which butyl amine was used to quench a small aliquot for analysis. HPLC-MS reveals formation of butyl amide product and the saturated four-carbon chain decreases the polarity of the quenched product to provide good separation to a slower moving peak by HPLC-MS analysis; see

Scheme 10. Additionally, the reaction of an NHS ester with H_2O forms a product which is identical to the starting material, so diluting the active ester reaction with pure water for HPLC analysis is useless.

By testing the product of this step with a dilute aqueous solution of butylamine on HPLC-MS, it was evident that this step was never an issue with any set of reaction conditions used.

Rather, it was found that it was the second step in the reaction – the addition of the MRI contrast module – which was so difficult to achieve. What remained was to determine which factor was negatively affecting this step. Some byproducts were seen in the MS data, true, but not enough was known to say exactly what these byproducts were (or how to avoid them). Alkaline, anhydrous conditions were needed, but

obtaining the correct pH by the addition of organic base was never an issue. The only remaining factor to consider was the choice of organic solvent.

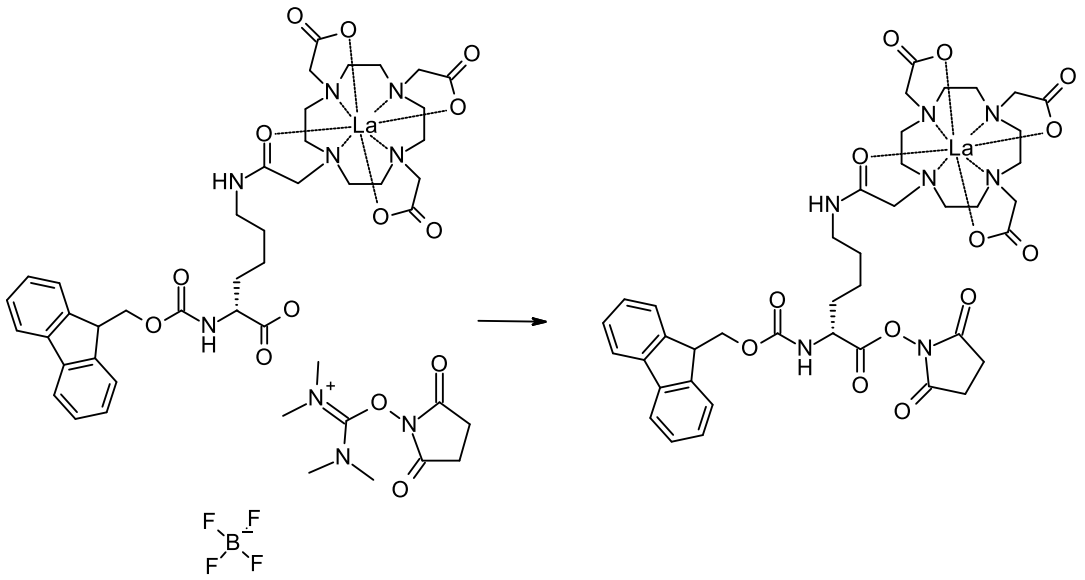

Scheme 9. Activation of an acidic lysine backbone by TSTU yields a succinimidyl leaving group.

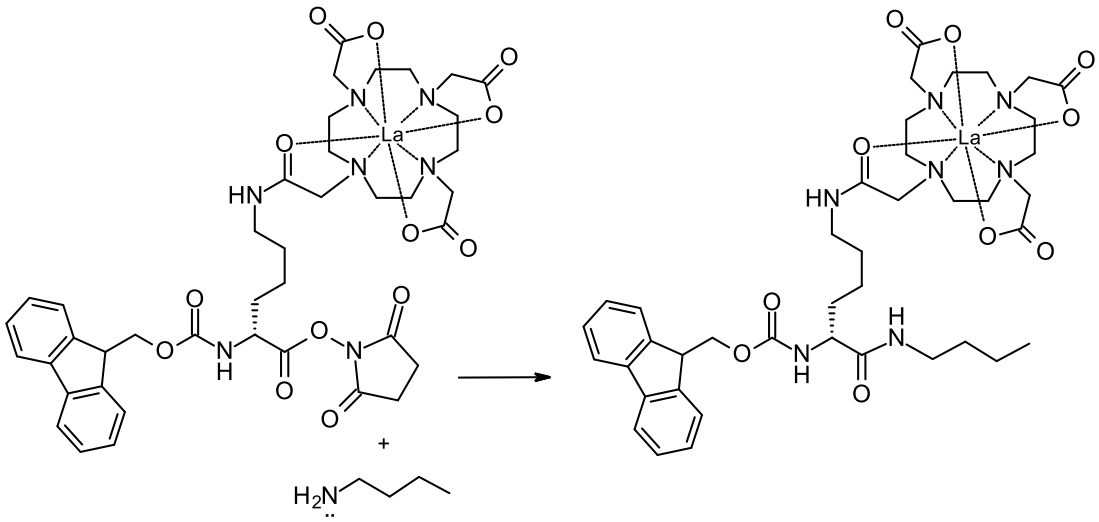

Scheme 10. Monitoring NHS ester formation by addition of butyl amine to form a more lipophilic product which is easily observed by HPLC-MS.

The true issue with the reaction proved to be solubility. After removal of the Fmoc protecting group, the MRI contrast module simply is not soluble in more commonly used solvents, such as NMP, DMF, ACN, or MeOH. In the past, we had simply heated the solution to 50℃ and given it time, in the hopes that the reagents would prove 'soluble enough' for what was needed. This, however, was not good enough. After running some solubility tests for the MRI contrast module, we discovered that the compound was readily soluble in DMSO. When the solvent was changed to DMSO, this allowed for successful and reproducible results of the coupling reaction.

In addition to the reaction conditions required, the manner of purification was found to be an important factor to consider. We use two primary methods of purification for the di-metal imaging modules: SPE and HPLC-prep, both utilizing reverse-phase stationary phases. We found that, although HPLC-prep is capable of providing sharper separations by use of a linear gradient and high pressure, yields were significantly smaller than expected. Conversely, when manual SPE methods were used, yields were in the range of what was expected based on data acquired while monitoring the reaction. We suspect this may be due to some chemistry occurring between the crude products and the HLPC columns used, but further work would be required to confirm or refute this.

3.4 Fmoc Deprotection of dipeptide module

Upon successful coupling of the two amino acids, it was necessary to remove the Fmoc protecting group from the dipeptide to proceed with further chemistry. This reaction was run similarly to that discussed above for the deprotection of **3** to yield **4**, and, likewise, provided reproducible results with high yields.

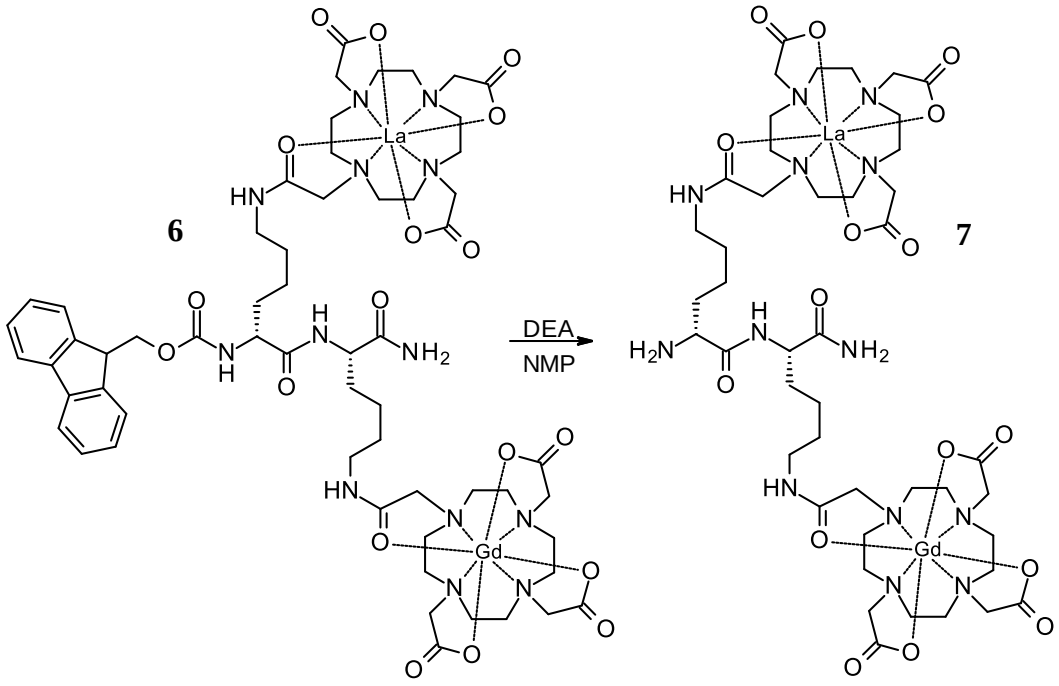

*Scheme 11. Fmoc deprotection of **6** to yield H-dLys(DOTA-La)-Lys(DOTA-Gd)-NH_2,**7**.*

3.5 SMCC vs DSS carbon linker

Within our modular approach, two different carbon-chain linkers are available for use. SMCC [succinimidyl 4-(N-maleimidomethyl)cyclohexane-1-carboxylate, Figure 16] is often used for formation of peptide bonds and cross-linking in proteins. DSS [disuccinimidyl suberate, Figure 17] is used for a similar purpose and is more common in peptide synthesis and coupling as well. Because of the different functional groups, one may be more useful or efficient than the other for purposes of modular TMIA synthesis.

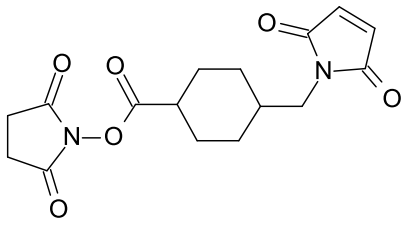

Figure 16. SMCC linker.

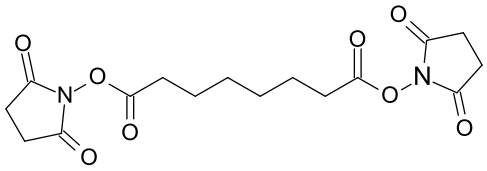

Figure 17. DSS linker.

DSS is symmetrical and contains two succinimidyl groups which are equally reactive, while SMCC is asymmetrical and contains one succinimidyl group and one maleimide group. Therefore, SMCC is expected to be more selective for synthesis and limit the symmetric products formed. DSS, on the other hand, coupled to the targeting group in a timely manner, but the DSS reactions included additional factors for consideration, such as the water sensitivity of the succinimide group and the increased potential to form symmetric product. In the end, both DSS and SMCC were useful for the synthesis of TMIAs for MRI/PET of cancer, but DSS was preferable because it coupled more reliably than SMCC in the final steps.

3.6 Synthesis of TMIA containing SMCC linker

SMCC was the first of the two linkers to be introduced into the experimental procedures. The succinimide group coupled readily to the primary amine of lysine. However, the coupling of a primary amine to the maleimide of SMCC (which is intended for sulfur bonds) proved to be a difficult reaction to force to completion. SMCC was useful in that it did prevent symmetric products (wherein a dimetal imaging module is coupled to both the maleimide and the succinimidyl groups), but the final coupling to the targeting group took quite some time and/or heat to proceed; these reactions are shown in

Scheme 12 and Scheme 13. Additionally, a method for the removal of excess SMCC from the crude product following

Scheme 12 has yet to be developed, and the lack thereof introduces some complications in the coupling of c(RGDyK) to **9**.

.

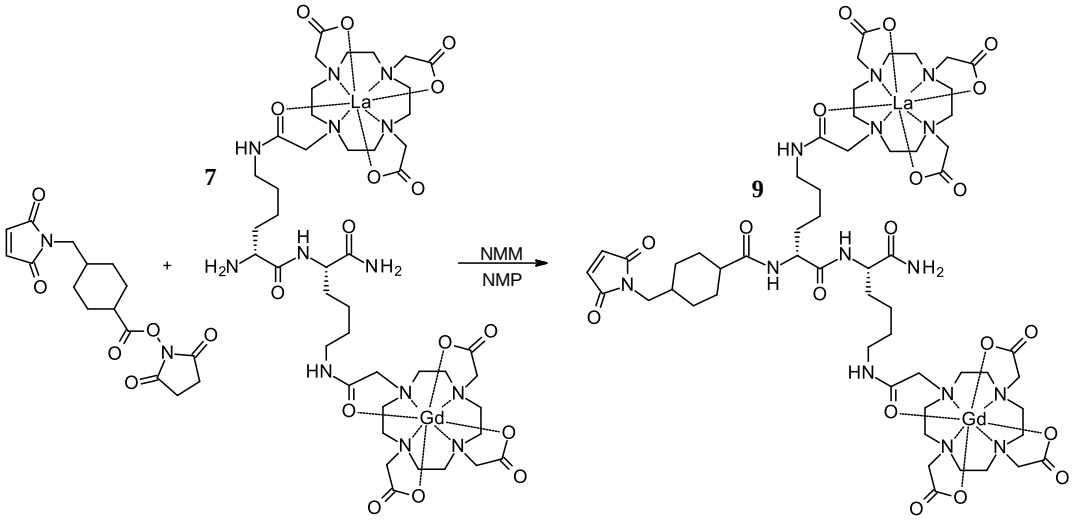

*Scheme 12. Coupling of SMCC to **7** for formation of **9**.*

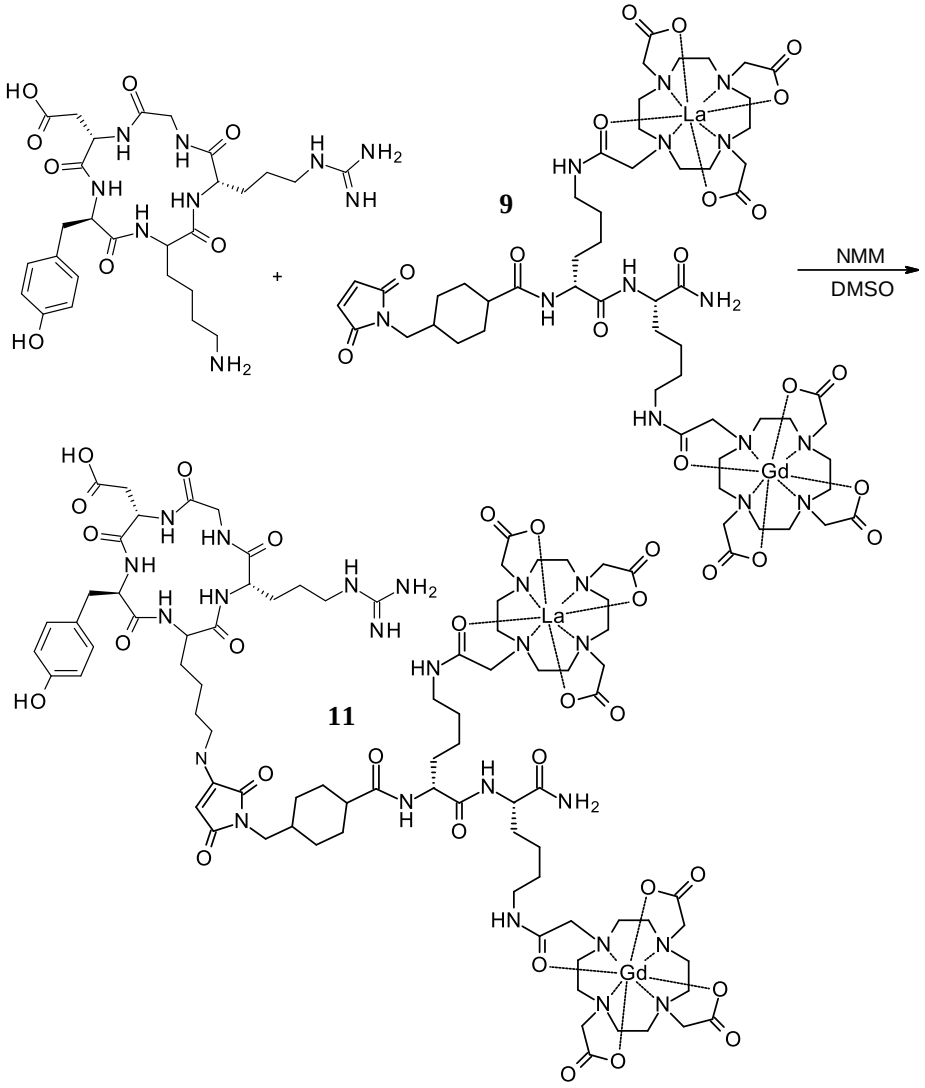

*Scheme 13. Coupling of c(RGDyK) to **9** for formation of **11**.*

3.7 Synthesis of TMIA containing DSS linker

The final couplings, both of DSS to 7 (

Scheme 14) and of c(RGDyK) to 8 (Scheme 15), were improved by carefully determining the equivalents of each reagent to use, and by the use of a syringe pump. Formation of symmetrical product was reduced by ensuring an excess of DSS in solution. However, upon addition of a targeting group to the solution, the presence of excess DSS results in formation of compounds such as c(RGDyK)-DSS-c(RGDyK) rather than the desired c(RGDyK)-DSS-dK(DOTA-La)-K(DOTA-Gd)-NH2. Because c(RGDyK) is a rather expensive peptide to purchase, it is not practical to use overly excessive amounts to counter this problem. Therefore, 1 equivalent of DSS, 0.9 equivalents of dimetal puzzle piece, and 1.2 equivalents of the targeting group were determined to be optimal for the final coupling reaction.

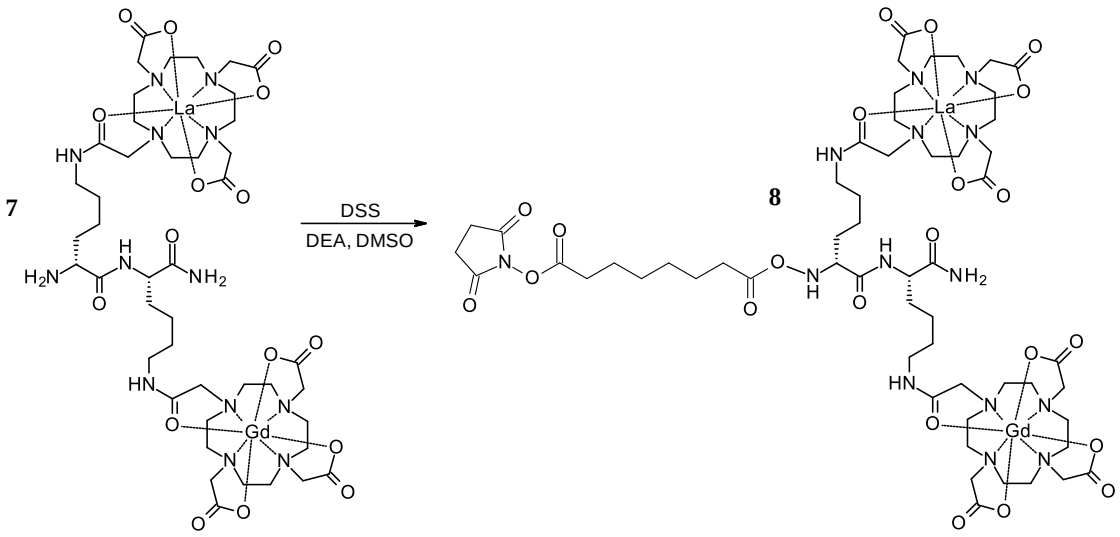

*Scheme 14. Coupling of DSS to di-metal module **7** for formation of **8.***

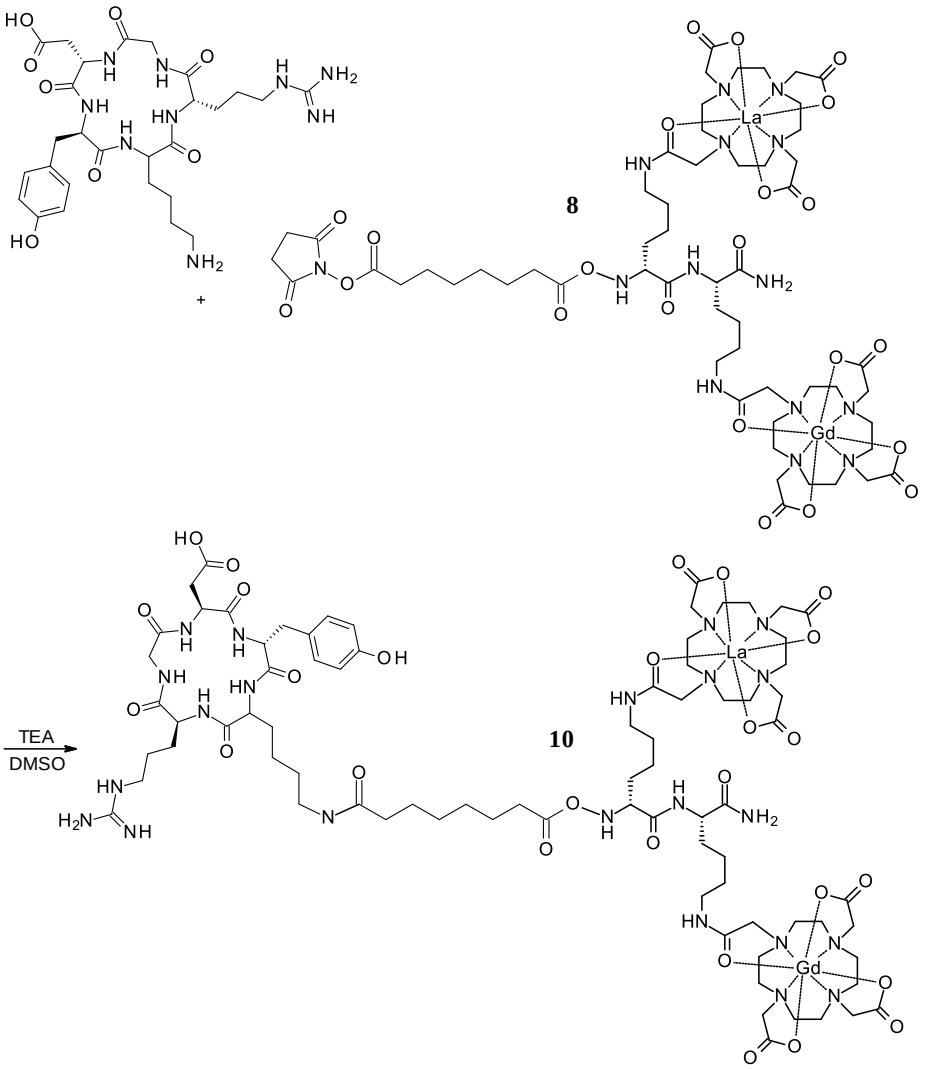

*Scheme 15. Coupling of c(RGDyK) to **8** for formation of **10**.*

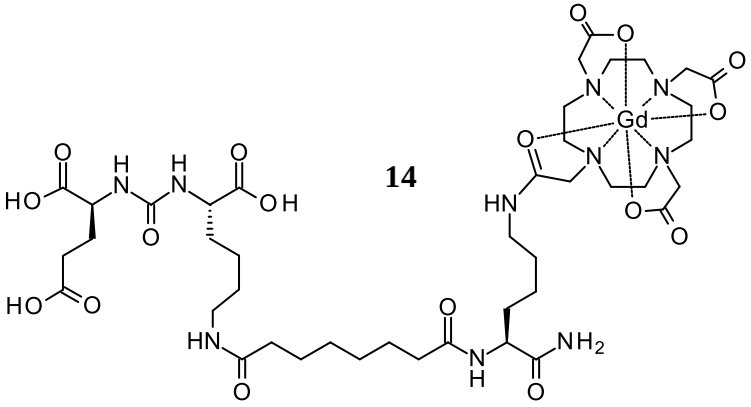

Figure 18. DCL-DSS-K(DOTA-Gd)-NH2

3.8 Convergent Synthesis of TMIA for MRI of Prostate Cancer

One of the other major considerations was the order of coupling steps: that is, should we continue in the traditional linear right-to-left method of synthesizing peptides, or would a convergent synthetic method prove more efficient? (Scheme 1 versus Scheme 2, page 21). The application of such a convergent method of synthesis was prompted by the use of a similar method for the synthesis of DCL-DSS-K(DOTA-Gd)-NH_2 (**14**), a targeted MRI contrast agent for PrCa.

During work towards the synthesis of **14**, we found that the most troublesome step of the synthesis was the final coupling of the DCL urea to the DSS linker. While small amounts of TCA were able to be synthesized this way, the reaction took a considerable amount of time to complete, and was not achieved on any scale suitable for further testing of the TCA. Therefore, we determined that the reaction could be simplified by coupling DSS to DCL first, and then coupling this component to the MRI contrast module (

Scheme 16). As of this writing, a manuscript from our group detailing the synthesis of **14** by this method is out for submission.

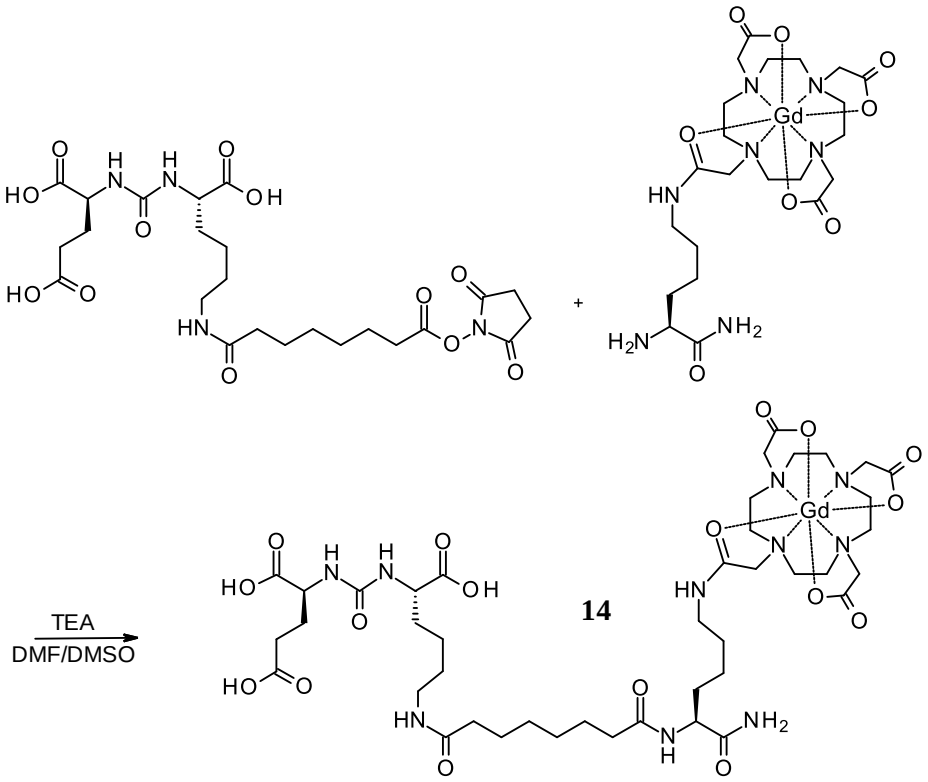

*Scheme 16. Convergent synthesis of TMIA for MRI of prostate cancer, DCL-DSS-K(DOTA-Gd)-NH_2 (**14**)*

Because a convergent method proved successful for that synthesis described above, we wondered whether it might also prove useful for the synthesis of a dual-modal PET/MRI TMIA. Further support for a convergent synthesis is found in the potential for a method of purifying c(RGDyK)-DSS prior to the addition of an imaging moiety. We have found that, though the succinimide group is reactive with water, this reactivity is reduced in acidic conditions, and, as found in the synthesis of **14**, the targeting module DCL-DSS could be successfully purified by preparative HPLC. Because the lanthanide placeholder is, by design, labile in acidic aqueous conditions, purification of **8** by preparative HPLC with acidic buffers is not suitable. If a convergent synthesis were utilized, c(RGDyK)-DSS would not be subject to those same constraints and would therefore be a preferred intermediate.

There are drawbacks to a convergent method of synthesis, however. Because we want to emphasize the practicality of applying our methods of synthesis to any of a number of targeting groups, it is desirable to maintain linear methods of synthesis, wherein the targeting moiety is coupled to the linker in the last step of synthesis. Additionally, the primary difficulty in the DCL-linker coupling described above were due to the three acids present on the targeting moiety; c(RGDyK) is much less reactive in that regard, and therefore does not suffer quite the same difficulty in coupling. As of this writing, convergent methods of synthesis have not been studied for this TMIA, but will be considered in the future for efforts to improve synthetic methods.

3.9 T_1 Relaxivity Measurements

Once an MRI T_1-contrast agent was developed, synthesized, and purified, its efficacy as an actual contrast agent had to be determined. This was done through measurement of T_1 relaxivity on a 43MHz NMR from Magritek. These experiments allowed us to measure the effects of the contrast agent on the rate of relaxation of water within a magnetic field.

Small samples of the contrast agents were weighed, and serial dilutions were used to make solutions of 0, 0.5, 1, 2, 3, and 4 mM concentrations of Gd. These were run in the NMR in melting point capillary tubes (1.6 x 90 mm), held in a standard 5mm NMR tube with an adapter. The samples were exposed to a standard inversion-recovery pulse sequence, and the time between pulses was varied. When this integration of the signal was plotted against time between pulses, a logarithmic relationship was seen. Based on equations governing relaxivity, a time constant (T_1) for each solution and the relaxivity (r_1) of each compound could be determined.

Because Gd(III) is a T_1 contrast agent – that is, it primarily affects the T_1 relaxation processes of a sample, and not the T_2 processes – we were interested only in the T_1 relaxation times. The T_1 relaxation time for a sample is related to its signal in MRI by equation (2); S is the observed signal, S_0 is the maximum signal observed, t is the time between the initial RF-pulse and the measurement, or the interval time, and T_1 is the relaxation time of interest. We graph the signal (S) as the area under curve against the interval time (t), and obtain a logarithmic function (Figure 19). SOLVER is then used to fit equation (2) to the data by solving for values of S_0 and T_1.

$$S = S_0(1 - e^{-\frac{t}{T_1}}) \qquad (2)$$

The reported relaxivity is the change in T_1 as a function of the change in concentration of contrast agent (equation 1) – in this case, it is obtained by plotting the values of $1/T_1$ (or the R_1 values) observed for a range of $[Gd^{3+}]$ values and calculating the slope of that linear relationship (Figure 20). The cumulative data from DOTA-Gd (commercially available as Dotarem) and three Gd-containing compounds synthesized in our lab (**3**, **6**, and **14**) are shown below in Figure 21.

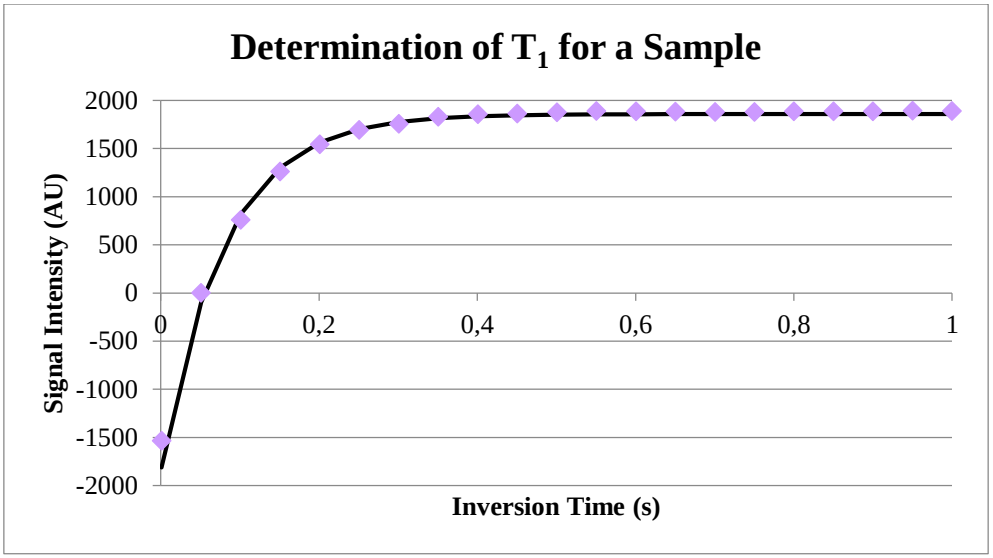

Figure 19. Sample plot used to determine T_1 and S_0 for a sample. Signal Intensity is obtained from the integration of the peak for each repetition, and the inversion time is increased for each repetition. The purple points represent the experimentally obtained data points, and the black curve represents the theoretical values obtained by equation (2).

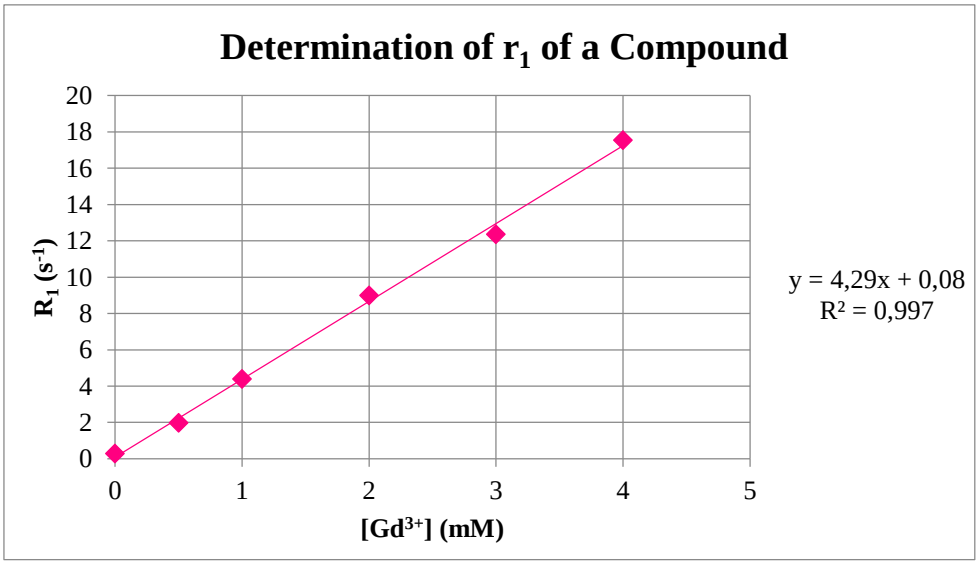

Figure 20. Sample plot used to determine the relaxivity of a contrast agent. R_1 values are taken from the solution found for each equation (2) at each concentration. Y-intercept of the linear intercept represents the R_1 for a sample of H_2O without the presence of $[Gd^{3+}]$ contrast agent; the slope yields the relaxivity of the contrast agent at a given field strength.

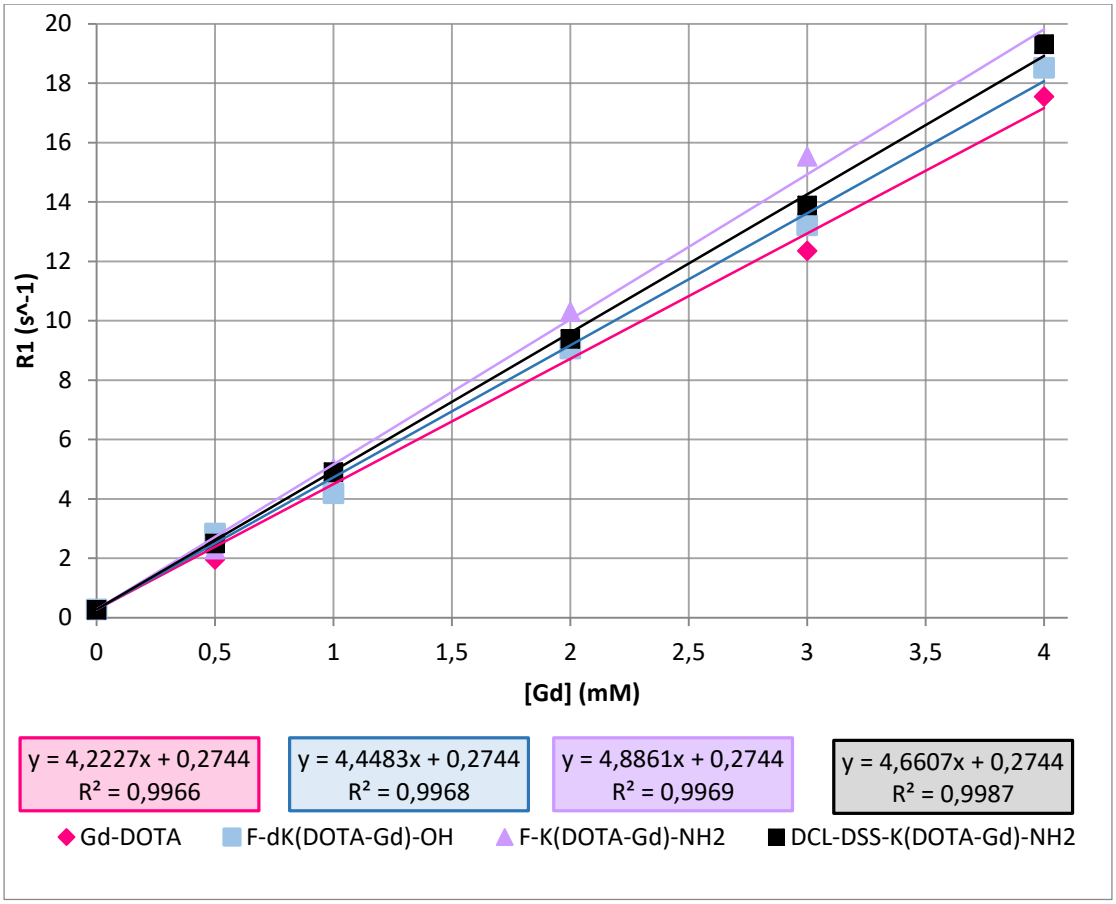

Figure 21. Showing the relaxivities of four distinct compounds as measured by inversion-recovery sequences on the 43MHz Magritek NMR.

3.10 Transmetallation of La^{3+} to Cu^{2+} Successful, Though Incomplete

The final transmetallation process is arguably the most important step in this synthesis. It is the step which renders the TMIA useful for PET imaging, and it is the step which proves the usefulness of our method of using a placeholder metal in the chelating group against than using the more frequently used protecting groups in imaging agent synthesis.

A few things were important to keep in mind for this transmetallation procedure. First, we know (thanks to J. Perez's data) that La is labile in dilute (0.05 to 0.1 M) aqueous TFA solutions, and that Gd is also labile at higher concentrations of TFA (0.5

M). Therefore, it was important to use an appropriately dilute solution of TFA such that the La-DOTA bonds could be displaced, but that the stronger Gd-DOTA coordination bonds would not be disrupted.

Additionally, it was important that the transmetallation occur relatively quickly. The half-life of ^{64}Cu is approximately 12.7 hours; if it takes that long for ^{64}Cu to replace ^{57}La in acidic solution, then the copper will hardly be useful for imaging by the end of the process and isolation of the product/TMIA. However, this is only an issue if the transmetallation is done in one step. If the process is completed in two steps, with the lanthanide being displaced overnight followed by the addition of Cu^{2+} to the solution the next day, this problem resolves itself.

Based on previous data and results from transmetallation experiments, the demetallation of the final TMIA – the displacement of La^{3+} – was expected to take perhaps a weekend in solution. We found, however, that La^{3+} was completely replaced by Cu^{2+} (in the form of $[Cu(NO_3)_2 \cdot 6H_2O]$) in 0.1M TFA aqueous solution overnight.

As of the time of this writing, the experiments for the transmetallation of a final TMIA are not finished. In the two completed trials for the transmetallation processes of both **10** to **12** and **11** to **13**, the process was expected to take several days, but HPLC-MS analysis after twelve hours showed full conversion to product. In a future repetition of this experiment, the samples will be monitored much more frequently, and the effects of variables such as temperature and concentrations of reagents would be considered, as well. Additionally, we will pursue transmetallation in two steps as described above, in order to avoid the potential for a radioactive sample of copper to decay significantly during the process.

Also not yet complete is a method to purify the final TMIA after transmetallation. An HPLC column purification is expected to be the most useful to

remove the excess $Cu(NO_3)_2$ and La from the sample, but with such small reaction scales as have been run thus far, a reverse-phase purification has not been successful. SPE methods have been successful for similar purifications following transmetallations of analogous compounds previously developed in our lab, and are expected to be useful here as well.

3.11 Preferred Methods of Purification and Analysis

As in any synthesis, purifying the product and isolating a pure sample is one of the crucial steps. Without purification, a product cannot properly be characterized. For these purifications, we focused on reverse phase (RP) chromatographic methods, including RP-HPLC and SPE. RP-HPLC and related methods were the most efficient method of purification for the compounds involved in this project due to their hydrophilic nature – they are much too polar for purification by normal phase column chromatography, and crystallization doesn't provide sufficient separation of product from undesirable byproducts or excess reagent.

Only those intermediates containing the Fmoc protecting group were suitable for analysis by UV detection during HPLC, due to the characteristic absorption of Fmoc at 264nm. In general, the compounds in this synthesis were assayed and characterized by mass spectroscopy methods that included LC-MS and flow injection-MS (also called loop injection) methods.

Historically, within our group, ACN/AmAc buffer systems were used for analysis of imaging agents and intermediates by HPLC-MS, and in most cases these were easily transferred to HPLC prep or SPE on C-18 cartridges with ACN/H2O systems. The reaction products involved here are, in most cases, significantly more

polar than any starting materials or byproducts, and this solvent system generally proved to be suitable for purification. However, towards the final stages of synthesis, this was no longer the case.

The deprotected di-lysine, H-dK(DOTA-La)-K(DOTA-Gd)-NH2 (**7**), for example, proved difficult to purify, because all compounds of interest in the reaction were water-soluble and were so polar as to hardly be retained on a C18-based HPLC column. This problem was resolved by incorporation of a dilute acidic aqueous phase, and separation with a solvent system of ACN/TFA (aq.) was successful. By protonating the acidic nuclei, the polarity was reduced, and the purification was achievable with good results. Similar problems and solutions were encountered for the penultimate compound, c(RGDyK)-DSS-dK(DOTA-La)-K(DOTA-Gd)-NH2 (**11**). The only caveat associated with the use of an acidic buffer in these cases is that the La-DOTA bonds are, as discussed previously, intentionally broken in acidic solution. Therefore, it is important to keep the acidic solution at concentrations safely below those used for transmetallation, as well as to isolate the products relatively quickly after fractionation, in order to reduce the risk of prematurely displacing the lanthanide.

3.12 Successful Synthesis of Several TMIAs by a Modular Approach

Over the course of this project, our modular approach to the synthesis of TMIAs for both single- and dual-modal imaging was proven to be useful. Two TMIAs (**12** and **13**) featuring c(RGDyK) as a targeting moiety and two DOTA-metal groups were synthesized and observed by both HPLC-MS and HRMS, although further work on a larger scale will be required before the relaxivities of those compounds can be measured.

The single modal TMIA for MRI of PrCa, compound **14,** was successfully synthesized and isolated; the relaxivity of this compound was measured and found to be comparable to, if not better than, that of the commercially-available Dotarem. This work provided a facile method for the preparation of a copper-containing analogue to **14**, DCL-DSS-K(DOTA-Cu)-NH_2, which would be useful as a metal-based radiotracer for PET of PrCa.

Chapter 4. Conclusion

The usefulness and applicability of our group's modular method for the synthesis of amino-acid-based TMIAs has been shown by the synthesis of two related TMIAs, one for PET-MRI of cancer, and one for MRI of prostate cancer. Furthermore, our method of utilizing a La as a placeholder metal to be later replaced by Cu for PET in the presence of Gd was demonstrated on a final TMIA, although these processes and purification methods have yet to be optimized.

One-pot syntheses were utilized for each lysine-based imaging module, and TMIAs were synthesized from these modular components. During synthesis, compounds were characterized by HPLC-MS, HRMS, and NMR. Those compounds useful for MRI were tested by NMR to determine their effectiveness as MRI T_1 contrast agents, and our compounds were found to be comparable and even slightly better than current commercially available non-targeted Gd-based contrast agents.

The solubility of intermediates was the most critical factor in the modular synthesis of dual modal TMIAs. The use of a metal as a placeholder and protecting group for DOTA was proven to be useful and effective, and the La placeholder was easily displaced in dilute TFA and replaced with Cu. Methods for dual-modal imaging agent synthesis were optimized to provide consistent results.

Results from this work present an effective means of synthesizing a variety of dual-modal TMIAs for combined PET and MRI studies, which may utilize a broad range of targeting moieties. The method is also applicable to imaging agents containing dyes that may be designed for PAI, fluorescence or optical imaging, and photodynamic therapy. Additionally, future research in our lab will explore modifications to the MRI contrast modules for the development of high-relaxivity TMIAs for use in MRI.

Chapter 5. Experimental Procedures

General Considerations

Chemicals were purchased from VWR (Radnor, PA), Sigma Aldrich (St. Louis, MO), Alfa Aesar (Ward Hill, MA), TCI (Tokyo, Japan), and Acros Organics (Morris Plains, NY), and were used as received unless otherwise stated. All were HPLC or American Chemical Society grade. Amino acid starting materials were purchased from Bachem (Bubendorf, Switzerland), and Chem-Impex Int'l Inc. (Wood Dale, IL). 1,4,7,10-Tetraazacyclododecane-1,4,7,10-tetraacetic acid (DOTA) was purchased from Macrocyclics (Houston, TX).

The HPLC-MS instrument used was a Waters 2695 Alliance HPLC with a Waters 2998 Diode Array Detector and a Waters 3100 SQ Mass Spectrometer. HPLC columns used included an Agilent XDB C18 column (3 mm x 100 mm, 3µ) and a Waters XBridge C18 column (50 mm x 3 mm, 3µ). Mass spectra were recorded at unit resolution with positive and negative switching mode at either 35 or 50 V cone voltages. HPLC methods utilized 0.5mL/min flow rates and solvent systems of ACN or MeOH with a 0.1M ammonium acetate aqueous phase.

Preparative HPLC was carried out with a Waters 600E system controller, and Waters 600 multi-solvent delivery system using a 30 mL/min flow rate. For SPE purification, Varian Mega Bond Elute C18 cartridges were utilized, of appropriate size for the scale of the reaction. Preparative HPLC methods utilized a column from Keystone Scientific, Inc. Hyperprep C18 BDS (250mm x 20 mm, 8µ).

Chromatographic gradients for preparative HPLC, and SPE are denoted as (X/Y:A-B), where X is the organic mobile phase and Y is the organic mobile phase, and A and B are the initial and final concentrations of X, respectively. In the case of SPE, 5% intervals were used.

High resolution mass spectra (HRMS) were obtained on a Waters Synapt G2Si (School of Chemical Sciences, University of Illinois at Urbana-Champaign) using the following parameters: Flow injection at flow rate of 0.1 ml/min, H_2O/ACN/0.1% Formic Acid, positive and negative mode ESI, Cone voltage = 25, capillary voltage = 3.0, ion source temperature = - 100°C, desolation temperature = 180°C, nebulizing gas (N_2) flow = 200 L/h, cone gas (N_2) flow = 5L/h.

F-K(DOTA-OtBu3)-NH_2 (1) Fmoc-Lys(H)-NH_2 (467mg, 0.97mmol) was dissolved in a mixture of DCM:DMF (1:1, 4mL total volume). Into a separate flask containing DCM (5mL) was added DOTA-OtBu (500.mg, 0.87mmol), HOBt (26.2mg, 0.19mmol), TBTU (373.7mg, 1.16mmol), and DIPEA (752.2mg, 5.82mmol). The two solutions were combined and stirred 1 hour under inert conditions. Solvent was removed by rotary evaporation and vacuum pump. The crude product was purified by liquid-liquid extraction with EtOAC and DI H_2O; organic layer was rotary evaporated and dried briefly under high vacuum. MS (HR, ESI) calc. for $C_{47}H_{75}N_7O_{10}$ 922.5654 [M+H], found 922.5624 [M+H].

F-K(DOTA)-NH_2 (2) Compound **1** (894mg, 0.969mmol) was dissolved in TFA (15mL) with the addition of 0.3mL H_2O and stirred, loosely capped, for two hours. TFA was removed by diluting the reaction solution with hexanes, then removing both solvents by rotary evaporation, and repeating this process three times. Once dried under vaccum, this crude product was brought forth to the next reaction without further

purification. MS (HR, ESI) calc. for $C_{37}H_{50}N_7O_{10}$ 752.36192 [M-H], found 752.36240 [M-H].

F-K(DOTA-Gd)-NH_2 (3, method A) Compound **2** (730.mg, 0.968mmol) was dissolved in DMF (10mL). Gadolinium (III) acetate (983.2mg, 2.42mmol) was added to the solution. The reaction stirred under ambient conditions 1 hour. Crude product was isolated by rotary evaporation. Pure product was obtained by SPE (ACN/H2O:10-60). Yield: 414.9mg (47%).

F-K(DOTA-Gd)-NH_2 (3, method B) Commercially-available DOTA (500.0mg, 0.813mmol) was stirred into suspension in a solution of NMM (1233.4mg, 1.22mmol) in anhydrous DMF (35mL). This solution was heated briefly to promote solvation, then allowed to cool back to room temperature. A solution of TSTU (489.6mg, 1.63mmol) in DMF (10mL) was added to the reaction flask over 30 minutes with the use of a syringe pump, followed by the addition of a solution of Fmoc-Lys(H)-NH2 (380.0mg, 0.81mmol) in the same manner. Immediately following the dropwise addition of this reagent, $Gd(OAc)_3$ (495.5mg, 1.22mmol) was added to the reaction flask as a crystalline salt. The reaction was stirred another ten minutes. Crude product was precipitated from the solution by the addition of ethyl ether and isolated by decanting the organic solvent after centrifugation. Purification by SPE (ACN/H2O:10-60) yielded the desired product. Yield: 200.8mg (27%). MS (HR, ESI) calc. for $C_{37}H_{48}GdN_7O_{10}Na$ 931.26014 [M+Na], found 931.2566 [M+Na].

H-K(DOTA-Gd)-NH_2 (4) Compound **3** (50.0mg, 0.055mmol) was dissolved in anhydrous DMF (7mL). DEA (80.5mg, 1.10mmol) was added to this solution. The reaction stirred under inert atmosphere one (1) hour. Crude product was precipitated by addition of ethyl ether to the reaction solution, and organic solvent was decanted after centrifugation. Pure product was isolated by liquid-liquid extraction with ethyl acetate and H2O, with product found in the aqueous layer. Yield: 35.8mg (95%). MS (HR, ESI) calc. for $C_{22}H_{37}GdN_7O_8$ 685.19447 [M-H], found 685.19477 [M-H].

F-dK(DOTA-La)-OH (5) Commercially-available DOTA (500.2mg, 0.98mmol) was stirred into suspension in a solution of NMM (1139.2mg, 11.3mmol) in anhydrous DMF (30mL). This solution was heated briefly to promote solvation, then allowed to cool back to room temperature. A solution of TSTU (452.1mg, 1.50mmol) in DMF (10mL) was added to the reaction flask over 30 minutes with the use of a syringe pump, followed by the addition of a solution of Fmoc-dLys(H)-OH (304.0mg, 0.75mmol) in the same manner. Immediately following the dropwise addition of this reagent, La(NO3) (650.2mg, 1.50mmol) was added to the reaction flask as a crystalline salt. The reaction was stirred another ten minutes. Crude product was precipitated from the solution by the addition of ethyl ether and isolated by decanting the organic solvent after centrifugation. Purification by SPE (ACN/H2O 10-60) yielded the desired product. Yield: 200.0mg (30%). MS (HR, ESI) calc. for $C_{37}H_{48}LaN_6O_{11}$ 891.24457 [M+H], found 891.2431 [M+H].

F-dK(DOTA-Gd)-OH (6) Commercially-available DOTA (478.6mg, 0.934mmol) was stirred into suspension in a solution of NMM (1180.7mg, 11.7mmol) in anhydrous DMF (30mL). This solution was heated briefly to promote solvation, then allowed to cool back to room temperature. A solution of TSTU (468.6mg, 1.56mmol) in DMF

(10mL) was added to the reaction flask over 30 minutes with the use of a syringe pump, followed by the addition of a solution of Fmoc-dLys(H)-OH (315.0mg, 0.778mmol) in the same manner. Immediately following the dropwise addition of this reagent, Gd(OAc)3 (650.2mg, 1.50mmol) was added to the reaction flask as a crystalline salt. The reaction was stirred another ten minutes. Crude product was precipitated from the solution by the addition of ethyl ether and isolated by decanting the organic solvent after centrifugation. Purification by SPE (ACN/H2O 10-60) yielded the desired product. Yield: 205.5mg (27.8%). MS (HR, ESI) calc. for $C_{37}H_{48}GdN_6O_{11}$ 910.26233 [M+H], found 910.2621 [M+H].

F-dK(DOTA-La)-K(DOTA-Gd)-NH_2 (7) Compound **5** (35.0mg, 3.93x10-2mmol) was dissolved in NMP (3mL) and to this solution was added triethylamine (39.8mg, 0.393mmol) and a solution of TSTU (118.3mg, 0.393mmol) in NMP (3mL). This reaction stirred under argon 1hr and was monitored by HPLC-MS after treating a sample with 0.1% aqueous butylamine. Upon completion of this portion of the reaction, crude intermediate product was precipitated by the addition of EtOAc and diethyl ether, and after centrifugation the organic layer was decanted and the crude solid dried briefly under argon. Compound (4) (44.5mg, 6.48x10-2mmol) was dissolved in 2mL DMSO. To this solution was added triethylamine (39.8mg, 0.393mmol), followed by the previously isolated crude product which had been reconstituted in NMP (3mL). This reaction ran 1hr. Crude product was precipitated by the addition of ethyl ether, and the organic layer was decanted after centrifugation. Pure product was obtained by preparatory HPLC (ACN/0.1% acetic acid aqueous, 30-60%). Fractions containing pure product were collected, concentrated by rotary evaporation, and freeze dried. Yield: 16.2mg, 26.5%. MS (HR, ESI) calc. for $C_{59}H_{85}GdLaN_{13}O_{18}$ 780.22212 [M+2H/2], found 780.223 [M+2H/2].

H-dK(DOTA-La)-K(DOTA-Gd)-NH_2 (8) Compound **7** (16.2mg, 1.04x10-3mmol) was dissolved in DMF (2mL) followed by the addition of diethylamine (15.21mg, 0.208mmol). Reaction ran 1hr. Crude product was precipitated by the addition of diethyl ether. This was centrifuged and the organic layer decanted; the crude solid was triturated with EtOAc to remove Fmoc byproduct, and was again centrifuged and the organic layer, decanted. Yield: 12.9mg (92.8%). MS (HR, ESI) calc. for $C_{44}H_{74}GdLaN_{13}O_{16}$ 1337.36822 [M+H], found 1337.369 [M+H].

DSS-dK(DOTA-La)-K(DOTA-Gd)-NH_2 (9) Commercial DSS (7.3mg, 1.98x10-2 mmol) was dissolved in DMSO (2mL) and to this was added NMM (13.4mg, 0.132mmol). Compound **8** (17.7mg, 1.32x10-2 mmol) was dissolved in DMSO (2mL) and was added to the first solution dropwise over 30 minutes with the use of a syringe pump. After the completion of this addition, the reaction stirred under argon an additional 30 minutes before a small aliquot was treated with butylamine and monitored by HPLC-MS. Crude product was isolated by precipitation with anhydrous diethyl ether and centrifugation with the organic solvent discarded. This crude product was dried under high vacuum and was not further purified before use in the next reaction.

SMCC-dK(DOTA-La)-K(DOTA-Gd)-NH_2 (10) Compound **8** (12.9mg, 9.56x10-3mmol) was dissolved in DMSO (2mL). To this was added triethylamine (9.77mg, 9.65x10-2mmol) and SMCC (16.0mg, 4.34x10-2mmol). Reaction ran under argon 2hr.

Crude product was precipitated by the addition of diethyl ether, and the organic layer was decanted after centrifugation and the solid was dried under argon.

c(RGDyK)-DSS-dK(DOTA-La)-K(DOTA-Gd)-NH_2 (11) Compound **9** (17.0mg, $1.07x10^{-2}$mmol) was dissolved in DMSO (1mL). To this was added a solution of NMM (10.82mg, 0.107mmol) and commercial c(RGDyK) (13.3mg, $2.14x10^{-2}$mmol) in DMSO (1mL). Reaction stirred under argon 1hr. Crude product was precipitated by the addition of diethyl ether, and organic solvent was decanted after centrifugation. The crude product was dried under argon and was not further purified before continuing. MS (HR, ESI) calculated for $C_{79}H_{124}GdLaN_{22}O_{26}$ 1045.860141 m/z [M-2H/2], found 1045.8607 m/z [M-2H/2].

c(RGDyK)-SMCC-dK(DOTA-La)-K(DOTA-Gd)-NH_2 (12) Compound **8** (1.3mg, $8.36x10^{-4}$ mmol) was dissolved in DMSO (1mL). To this was added a solution of NMM (0.57mg, $8.36x10^{-3}$ mmol) and commercial c(RGDyK) (0.85mg, $9.19x10^{-4}$ mmol) in DMSO (1mL). Reaction stirred under argon 2 days. Crude product was precipitated by the addition of diethyl ether, and organic solvent was decanted after centrifugation. The crude product was dried under argon and was not further purified before continuing. MS (HR, ESI) calc. for $C_{83}H_{125}GdLaN_{23}O_{27}$ 1086.37099 [M-2H/2], found 1086.3707 [M-2H/2].

c(RGDyK)-DSS-dK(DOTA-Cu)-K(DOTA-Gd)-NH_2 (13) Compound **11** (20.0mg, 1.26x10-2 mmol) was dissolved in aqueous TFA solution (0.1M, 2mL). To this solution was added $Cu(NO_3)_2$ (23.6mg, 0.126mmol). This reaction stirred 24 hours at ambient conditions. The solvent was removed by rotary evaporation. MS (HR, ESI) calc. for $C_{79}CuH_{127}GdN_{22}O_{26}Na_2$ 688.92081 [M+H+2Na/3], found 688.9243 [M+H+2Na/3].

c(RGDyK)-SMCC-dK(DOTA-Cu)-K(DOTA-Gd)-NH_2 (14) Compound **12** (2.0mg, 9.19x10-4 mmol) was dissolved in aqueous TFA solution (0.1M, 2mL). To this solution was added $Cu(NO_3)_2$ (1.72mg, $9.19x10^{-3}$mmol). This reaction stirred 24 hours at ambient conditions. The solvent was removed by rotary evaporation. MS (HR, ESI) calc. for $C_{83}CuH_{125}GdN_{23}O_{27}Na_2$ 1071.37238 [M-2H+2Na/2], found 1071.3698 [M-2H+2Na/2].

DSS-K(DOTA-Gd)-NH2 (15) Commercial DSS (10.7mg, 2.92x10-2 mmol) was dissolved in DMSO:DMF (1:1, 2mL) and to this was added NMM (29.5mg, 0.292mmol). Compound **4** (20.0mg, 2.92x10-2 mmol) was dissolved in DMSO (2mL) and was added to the first solution dropwise over 30 minutes with the use of a syringe pump. After the completion of this addition, the reaction stirred under argon an additional 30 minutes before a small aliquot was treated with butylamine and monitored by HPLC-MS. Crude product was isolated by precipitation with anhydrous diethyl ether and centrifugation with the organic solvent discarded. This crude product was dried under high vacuum and was not further purified before use in the next reaction.

DCL-DSS-K(DOTA-Gd)-NH_2 (16a) Compound **15** (5.0mg, $5.32x10^{-3}$mmol) was dissolved in DMSO (1mL). To this solution was added NMM (34.4mg, 0.266mmol) and DCL urea (8.5mg, $2.66x10^{-2}$mmol). The reaction was stirred 3 hours in an oil bath at 35C and under argon gas. Crude product was isolated by precipitation with anhydrous

diethyl ether and centrifugation with the organic solvent discarded. This crude product was used to experiment with HPLC and SPE purification methods.

DCL-DSS-K(DOTA-Gd)-NH2 (16b) Compound **4** (35.9mg, $5.24x10^{-2}$mmol) was dissolved in DMSO (2mL). To this was added TEA (67.7mg, 0.524mmol) and a solution of DCL-DSS (30.0mg, $5.24x10^{-2}$mmol) in DMSO (0.7mL). The reaction was stirred under argon 1hr. Crude product was isolated by precipitation with diethyl ether and centrifugation, with the organic solvent discarded. Purification by preparative HPLC (ACN/0.1% TFA in H2O, 5-40%) yielded pure product. Yield: 16.8mg, 28%. MS (HR, ESI) calc. for $C_{42}H_{70}GdN_{10}O_{17}$ 1144.41614, found 1144.4150.

References

(1) Cancer today http://gco.iarc.fr/today/home (accessed Nov 7, 2017).

(2) Cancer Statistics https://www.cancer.gov/about-cancer/understanding/statistics (accessed Nov 7, 2017).

(3) Cooper, G. M. The Development and Causes of Cancer. **2000**.

(4) Chemotherapy Side Effects https://www.cancer.org/treatment/treatments-and-side-effects/treatment-types/chemotherapy/chemotherapy-side-effects.html (accessed Apr 2, 2019).

(5) Gonda, K.; Hamada, Y.; Kitamura, N.; Tada, H.; Miyashita, M.; Kamei, T.; Ishida, T.; Ohuchi, N. Highly Sensitive Imaging of Cancer with Functional Nanoparticles. *J. Photopolym. Sci. Technol.* **2015**, *28* (6), 731–736. https://doi.org/10.2494/photopolymer.28.731.

(6) Shahbazi-Gahrouei, D. Novel MR Imaging Contrast Agents for Cancer Detection. *J. Res. Med. Sci. Off. J. Isfahan Univ. Med. Sci.* **2009**, *14* (3), 141–147.

(7) Gao, Y.; Hernandez, C.; Yuan, H.-X.; Lilly, J.; Kota, P.; Zhou, H.; Wu, H.; Exner, A. A. Ultrasound Molecular Imaging of Ovarian Cancer with CA-125 Targeted Nanobubble Contrast Agents. *Nanomedicine Nanotechnol. Biol. Med.* **2017**, *13* (7), 2159–2168. https://doi.org/10.1016/j.nano.2017.06.001.

(8) Baltzer, P. A. T.; Kapetas, P.; Marino, M. A.; Clauser, P. New Diagnostic Tools for Breast Cancer. *Memo - Mag. Eur. Med. Oncol.* **2017**, *10* (3), 175–180. https://doi.org/10.1007/s12254-017-0341-5.

(9) Bohunicky, B.; Mousa, S. A. Biosensors: The New Wave in Cancer Diagnosis. *Nanotechnol. Sci. Appl.* **2010**, *4*, 1–10. https://doi.org/10.2147/NSA.S13465.

(10) Sivasubramanian, M.; Hsia, Y.; Lo, L.-W. Nanoparticle-Facilitated Functional and Molecular Imaging for the Early Detection of Cancer. *Front. Mol. Biosci.* **2014**, *1*. https://doi.org/10.3389/fmolb.2014.00015.

(11) Lin, E. C. Radiation Risk From Medical Imaging. *Mayo Clin. Proc.* **2010**, *85* (12), 1142–1146. https://doi.org/10.4065/mcp.2010.0260.

(12) Theerasilp, M.; Sunintaboon, P.; Sungkarat, W.; Nasongkla, N. Glucose-Installed, SPIO-Loaded PEG-b-PCL Micelles as MR Contrast Agents to Target Prostate Cancer Cells. *Appl. Nanosci.* **2017**, 1–11. https://doi.org/10.1007/s13204-017-0610-y.

(13) Hu, L. Y.; Kelly, K. A.; Sutcliffe, J. L. High-Throughput Approaches to the Development of Molecular Imaging Agents. *Mol. Imaging Biol.* **2017**, *19* (2), 163–182. https://doi.org/10.1007/s11307-016-1016-z.

(14) Ding, F.; Chen, S.; Zhang, W.; Tu, Y.; Sun, Y. UPAR Targeted Molecular Imaging of Cancers with Small Molecule-Based Probes. *Bioorg. Med. Chem.* **2017**, *25* (20), 5179–5184. https://doi.org/10.1016/j.bmc.2017.08.034.

(15) Huang, H. W. and J. PEGylated Peptide-Based Imaging Agents for Targeted Molecular Imaging http://www.eurekaselect.com/138211/article (accessed Nov 7, 2017).

(16) Le Joncour, V.; Laakkonen, P. Seek & Destroy, Use of Targeting Peptides for Cancer Detection and Drug Delivery. *Bioorg. Med. Chem.* **2017**. https://doi.org/10.1016/j.bmc.2017.08.052.

(17) Moon, S.-H.; Yang, B. Y.; Kim, Y. J.; Hong, M. K.; Lee, Y.-S.; Lee, D. S.; Chung, J.-K.; Jeong, J. M. Development of a Complementary PET/MR Dual-

Modal Imaging Probe for Targeting Prostate-Specific Membrane Antigen (PSMA). *Nanomedicine Nanotechnol. Biol. Med.* **2016**, *12* (4), 871–879. https://doi.org/10.1016/j.nano.2015.12.368.

(18) Chen, Y.; Chatterjee, S.; Lisok, A.; Minn, I.; Pullambhatla, M.; Wharram, B.; Wang, Y.; Jin, J.; Bhujwalla, Z. M.; Nimmagadda, S.; et al. A PSMA-Targeted Theranostic Agent for Photodynamic Therapy. *J. Photochem. Photobiol. B* **2017**, *167* (Supplement C), 111–116. https://doi.org/10.1016/j.jphotobiol.2016.12.018.

(19) Zhang, H.; Liu, X.; Wu, F.; Qin, F.; Feng, P.; Xu, T.; Li, X.; Yang, L. A Novel Prostate-Specific Membrane-Antigen (PSMA) Targeted Micelle-Encapsulating Wogonin Inhibits Prostate Cancer Cell Proliferation via Inducing Intrinsic Apoptotic Pathway. *Int. J. Mol. Sci.* **2016**, *17* (5), 676. https://doi.org/10.3390/ijms17050676.

(20) Chatzisideri, T.; Thysiadis, S.; Katsamakas, S.; Dalezis, P.; Sigala, I.; Lazarides, T.; Nikolakaki, E.; Trafalis, D.; Gederaas, O. A.; Lindgren, M.; et al. Synthesis and Biological Evaluation of a Platinum(II)-c(RGDyK) Conjugate for Integrin-Targeted Photodynamic Therapy. *Eur. J. Med. Chem.* **2017**, *141* (Supplement C), 221–231. https://doi.org/10.1016/j.ejmech.2017.09.058.

(21) Danhier, F.; Le Breton, A.; Préat, V. RGD-Based Strategies To Target Alpha(v) Beta(3) Integrin in Cancer Therapy and Diagnosis. *Mol. Pharm.* **2012**, *9* (11), 2961–2973. https://doi.org/10.1021/mp3002733.

(22) Chen, Y.; Foss, C. A.; Byun, Y.; Nimmagadda, S.; Pullambhatla, M.; Fox, J. J.; Castanares, M.; Lupold, S. E.; Babich, J. W.; Mease, R. C.; et al. Radiohalogenated Prostate-Specific Membrane Antigen (PSMA)-Based Ureas as Imaging Agents for Prostate Cancer. *J. Med. Chem.* **2008**, *51* (24), 7933–7943. https://doi.org/10.1021/jm801055h.

(23) Jayaprakash, S.; Wang, X.; Heston, W. D.; Kozikowski, A. P. Design and Synthesis of a PSMA Inhibitor–Doxorubicin Conjugate for Targeted Prostate Cancer Therapy. *ChemMedChem* **2006**, *1* (3), 299–302. https://doi.org/10.1002/cmdc.200500044.

(24) Nan, F.; Bzdega, T.; Pshenichkin, S.; Wroblewski, J. T.; Wroblewska, B.; Neale, J. H.; Kozikowski, A. P. Dual Function Glutamate-Related Ligands: Discovery of a Novel, Potent Inhibitor of Glutamate Carboxypeptidase II Possessing MGluR3 Agonist Activity. *J. Med. Chem.* **2000**, *43* (5), 772–774. https://doi.org/10.1021/jm9905559.

(25) Kozikowski, A. P.; Nan, F.; Conti, P.; Zhang, J.; Ramadan, E.; Bzdega, T.; Wroblewska, B.; Neale, J. H.; Pshenichkin, S.; Wroblewski, J. T. Design of Remarkably Simple, Yet Potent Urea-Based Inhibitors of Glutamate Carboxypeptidase II (NAALADase). *J. Med. Chem.* **2001**, *44* (3), 298–301. https://doi.org/10.1021/jm000406m.

(26) Davis, M. I.; Bennett, M. J.; Thomas, L. M.; Bjorkman, P. J. Crystal Structure of Prostate-Specific Membrane Antigen, a Tumor Marker and Peptidase. *Proc. Natl. Acad. Sci. U. S. A.* **2005**, *102* (17), 5981–5986. https://doi.org/10.1073/pnas.0502101102.

(27) Schülke, N.; Varlamova, O. A.; Donovan, G. P.; Ma, D.; Gardner, J. P.; Morrissey, D. M.; Arrigale, R. R.; Zhan, C.; Chodera, A. J.; Surowitz, K. G.; et al. The Homodimer of Prostate-Specific Membrane Antigen Is a Functional Target for Cancer Therapy. *Proc. Natl. Acad. Sci.* **2003**, *100* (22), 12590–12595. https://doi.org/10.1073/pnas.1735443100.

(28) Eder, M.; Schäfer, M.; Bauder-Wüst, U.; Hull, W.-E.; Wängler, C.; Mier, W.; Haberkorn, U.; Eisenhut, M. ^{68} Ga-Complex Lipophilicity and the Targeting Property of a Urea-Based PSMA Inhibitor for PET Imaging. *Bioconjug. Chem.* **2012**, *23* (4), 688–697. https://doi.org/10.1021/bc200279b.

(29) Sanna, V.; Pintus, G.; Bandiera, P.; Anedda, R.; Punzoni, S.; Sanna, B.; Migaleddu, V.; Uzzau, S.; Sechi, M. Development of Polymeric Microbubbles Targeted to Prostate-Specific Membrane Antigen as Prototype of Novel Ultrasound Contrast Agents. *Mol. Pharm.* **2011**, *8* (3), 748–757. https://doi.org/10.1021/mp100360g.

(30) Soudy, R.; Gill, A.; Sprules, T.; Lavasanifar, A.; Kaur, K. Proteolytically Stable Cancer Targeting Peptides with High Affinity for Breast Cancer Cells. *J. Med. Chem.* **2011**, *54* (21), 7523–7534. https://doi.org/10.1021/jm200750x.

(31) Gros, C. P.; Eggenspiller, A.; Nonat, A.; Barbe, J.-M.; Denat, F. New Potential Bimodal Imaging Contrast Agents Based on DOTA-like and Porphyrin Macrocycles. *MedChemComm* **2011**, *2* (2), 119–125. https://doi.org/10.1039/C0MD00205D.

(32) Jennings, L. E.; Long, N. J. 'Two Is Better than One'—Probes for Dual-Modality Molecular Imaging. *Chem. Commun.* **2009**, *0* (24), 3511–3524. https://doi.org/10.1039/B821903F.

(33) Fahnert, J.; Purz, S.; Jarvers, J.-S.; Heyde, C.-E.; Barthel, H.; Stumpp, P.; Kahn, T.; Sabri, O.; Friedrich, B. Use of Simultaneous 18F-FDG PET/MRI for the Detection of Spondylodiskitis. *J. Nucl. Med.* **2016**, *57* (9), 1396–1401. https://doi.org/10.2967/jnumed.115.171561.

(34) Beiderwellen, K.; Geraldo, L.; Ruhlmann, V.; Heusch, P.; Gomez, B.; Nensa, F.; Umutlu, L.; Lauenstein, T. C. Accuracy of [18F]FDG PET/MRI for the Detection of Liver Metastases. *PLOS ONE* **2015**, *10* (9), e0137285. https://doi.org/10.1371/journal.pone.0137285.

(35) Portnow, L. H.; Vaillancourt, D. E.; Okun, M. S. The History of Cerebral PET Scanning. *Neurology* **2013**, *80* (10), 952–956. https://doi.org/10.1212/WNL.0b013e318285c135.

(36) Catana, C.; Drzezga, A.; Heiss, W.-D.; Rosen, B. R. PET/MRI for Neurologic Applications. *J. Nucl. Med. Off. Publ. Soc. Nucl. Med.* **2012**, *53* (12), 1916–1925. https://doi.org/10.2967/jnumed.112.105346.

(37) Fei, B.; Muzic, R. F.; Lee, Z.; Flask, C. A.; Morris, R. L.; Duerk, J. L.; Oleinick, N.; Wilson, D. L. Registration of Micro-PET and High-Resolution MR Images of Mice for Monitoring Photodynamic Therapy; International Society for Optics and Photonics, 2004; Vol. 5369, pp 371–380. https://doi.org/10.1117/12.535465.

(38) Beyer, T.; Townsend, D. W.; Brun, T.; Kinahan, P. E.; Charron, M.; Roddy, R.; Jerin, J.; Young, J.; Byars, L.; Nutt, R. A Combined PET/CT Scanner for Clinical Oncology. *J. Nucl. Med.* **2000**, *41* (8), 1369–1379.

(39) Sawicki, L. M.; Grueneisen, J.; Buchbender, C.; Schaarschmidt, B. M.; Gomez, B.; Ruhlmann, V.; Wetter, A.; Umutlu, L.; Antoch, G.; Heusch, P. Comparative Performance of 18F-FDG PET/MRI and 18F-FDG PET/CT in Detection and Characterization of Pulmonary Lesions in 121 Oncologic Patients. *J. Nucl. Med.* **2016**, *57* (4), 582–586. https://doi.org/10.2967/jnumed.115.167486.

(40) Spick, C.; Herrmann, K.; Czernin, J. 18F-FDG PET/CT and PET/MRI Perform Equally Well in Cancer: Evidence from Studies on More Than 2,300 Patients. *J. Nucl. Med.* **2016**, *57* (3), 420–430. https://doi.org/10.2967/jnumed.115.158808.

(41) Karakatsanis, N. A.; Fokou, E.; Tsoumpas, C. Dosage Optimization in Positron Emission Tomography: State-of-the-Art Methods and Future Prospects. *Am. J. Nucl. Med. Mol. Imaging* **2015**, *5* (5), 527–547.
(42) Parry, D. A.; Booth, T.; Roland, P. S. Advantages of Magnetic Resonance Imaging over Computed Tomography in Preoperative Evaluation of Pediatric Cochlear Implant Candidates. *Otol. Neurotol. Off. Publ. Am. Otol. Soc. Am. Neurotol. Soc. Eur. Acad. Otol. Neurotol.* **2005**, *26* (5), 976–982.
(43) Eiber, M.; Rauscher, I.; Souvatzoglou, M.; Maurer, T.; Schwaiger, M.; Holzapfel, K.; Beer, A. J. Prospective Head-to-Head Comparison of 11C-Choline-PET/MR and 11C-Choline-PET/CT for Restaging of Biochemical Recurrent Prostate Cancer. *Eur. J. Nucl. Med. Mol. Imaging* **2017**, 1–10. https://doi.org/10.1007/s00259-017-3797-y.
(44) Hornak, J. *The Basics of MRI*; Interactive Learning Software: Henrietta, NY, 1997.
(45) MRI: The Dance of the Whirling Protons – The Alcohol Pharmacology Education Partnership.
(46) Chilla, S. N. M.; Henoumont, C.; Elst, L. V.; Muller, R. N.; Laurent, S. Importance of DOTA Derivatives in Bimodal Imaging. *Isr. J. Chem.* **2017**, *57* (9), 800–808. https://doi.org/10.1002/ijch.201700024.
(47) Rogosnitzky, M.; Branch, S. Gadolinium-Based Contrast Agent Toxicity: A Review of Known and Proposed Mechanisms. *Biometals* **2016**, *29*, 365–376. https://doi.org/10.1007/s10534-016-9931-7.
(48) Sherry, A. D.; Caravan, P.; Lenkinski, R. E. Primer on Gadolinium Chemistry. *J. Magn. Reson. Imaging JMRI* **2009**, *30* (6), 1240–1248. https://doi.org/10.1002/jmri.21966.
(49) Zhou, Z.; Lu, Z.-R. Gadolinium-Based Contrast Agents for MR Cancer Imaging. *Wiley Interdiscip. Rev. Nanomed. Nanobiotechnol.* **2013**, *5* (1), 1–18. https://doi.org/10.1002/wnan.1198.
(50) Paans, A. M. J. Positron Emission Tomography. **2006**.
(51) *Positron Emission Tomography: Basic Sciences*; Bailey, D. L., Townsend, D. W., Valk, P. E., Maisey, M. N., Eds.; Springer-Verlag: London, 2005.
(52) Li, Z.; Conti, P. S. Radiopharmaceutical Chemistry for Positron Emission Tomography. *Adv. Drug Deliv. Rev.* **2010**, *62* (11), 1031–1051. https://doi.org/10.1016/j.addr.2010.09.007.
(53) Rohren, E. M.; Turkington, T. G.; Coleman, R. E. Clinical Applications of PET in Oncology. *Radiology* **2004**, *231* (2), 305–332. https://doi.org/10.1148/radiol.2312021185.
(54) Anderson, C. J.; Ferdani, R. Copper-64 Radiopharmaceuticals for PET Imaging of Cancer: Advances in Preclinical and Clinical Research. *Cancer Biother. Radiopharm.* **2009**, *24* (4), 379–393. https://doi.org/10.1089/cbr.2009.0674.
(55) Nudat 2 https://www.nndc.bnl.gov/nudat2/chartNuc.jsp (accessed May 13, 2019).
(56) Voráčová, I.; Vaněk, J.; Pasulka, J.; Střelcová, Z.; Lubal, P.; Hermann, P. Dissociation Kinetics Study of Copper(II) Complexes of DO3A, DOTA and Its Monosubstituted Derivatives. *Polyhedron* **2013**, *61*, 99–104. https://doi.org/10.1016/j.poly.2013.05.042.
(57) Schmitthenner, H. F.; Beach, S.; Weidman, C.; Barrett, T. Modular Imaging Agents Containing Amino Acids and Peptides. US20150038672 A1, February 5, 2015.

(58) Azhdarinia, A.; Wilganowski, N.; Robinson, H.; Ghosh, P.; Kwon, S.; Lazard, Z. W.; Davis, A. R.; Olmsted-Davis, E.; Sevick-Muraca, E. M. Characterization of Chemical, Radiochemical and Optical Properties of a Dual-Labeled MMP-9 Targeting Peptide. *Bioorg. Med. Chem.* **2011**, *19* (12), 3769–3776. https://doi.org/10.1016/j.bmc.2011.04.054.

(59) Cacheris, W. P.; Nickle, S. K.; Sherry, A. D. Thermodynamic Study of Lanthanide Complexes of 1,4,7-Triazacyclononane-N,N',N"-Triacetic Acid and 1,4,7,10-Tetraazacyclododecane-N,N',N",N'''-Tetraacetic Acid. *Inorg. Chem.* **1987**, *26* (6), 958–960. https://doi.org/10.1021/ic00253a038.

(60) Pasha, A.; Tircsó, G.; Benyó, E. T.; Brücher, E.; Sherry, A. D. Synthesis and Characterization of DOTA-(Amide)4 Derivatives: Equilibrium and Kinetic Behavior of Their Lanthanide(III) Complexes. *Eur. J. Inorg. Chem.* **2007**, *2007* (27), 4340–4349. https://doi.org/10.1002/ejic.200700354.

(61) Chang, C. A.; Liu, Y.-L. Dissociation Kinetics of Cerium(Lll) Complexes of Macrocyclic Polyaza Polycarboxylate Ligands TETA and DOTA. *J. Chin. Chem. Soc.* **2000**, *47* (4B), 1001–1006. https://doi.org/10.1002/jccs.200000139.

Appendix I. HPLC-MS & HRMS Data

Compound **1** *Fmoc-Lys(DOTA-OtBu$_3$)-NH$_2$*

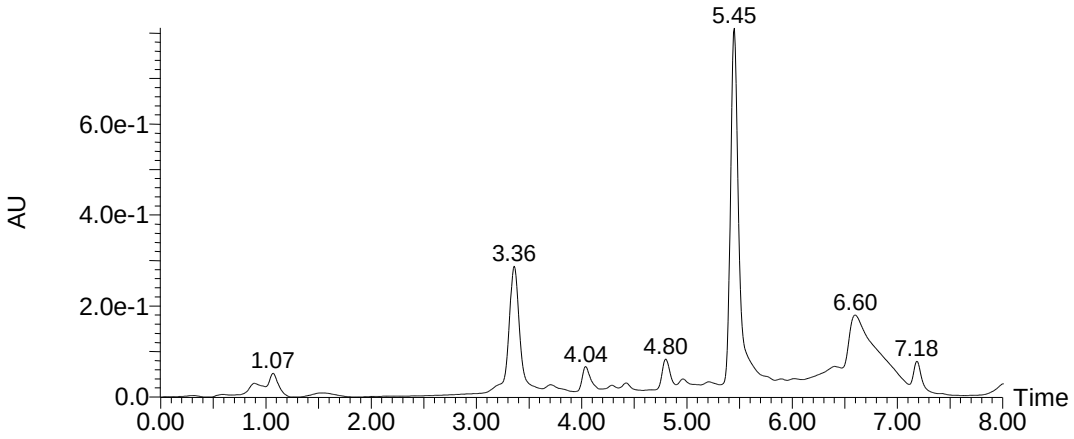

Extracted wavelength chromatogram of 265nm for crude reaction mixture

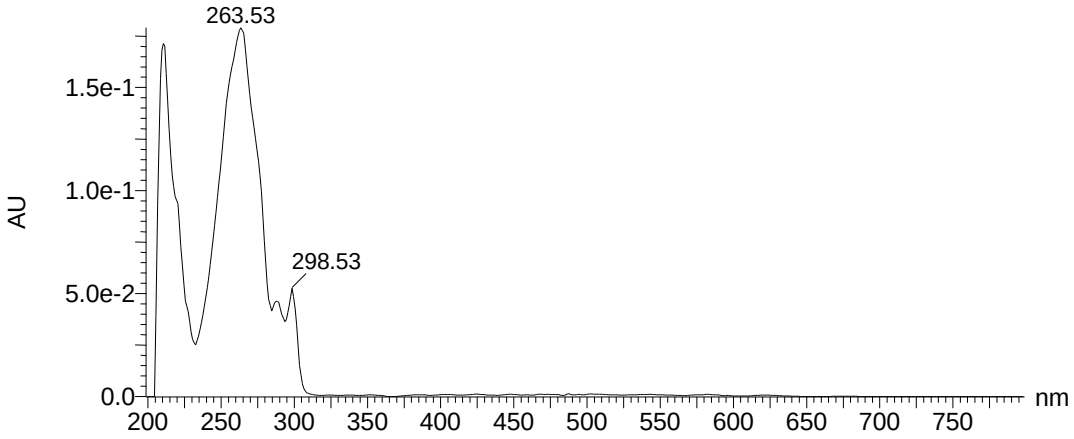

UV-Vis absorption spectrum at 6.60min with characteristic peak at 263nm for Fmoc protecting group

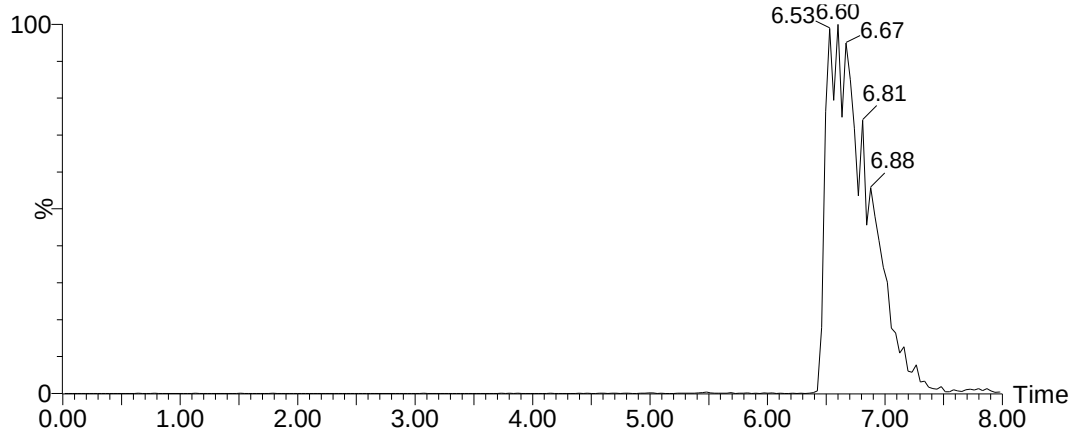

Extracted ion chromatogram (XIC) of 921.8 m/z

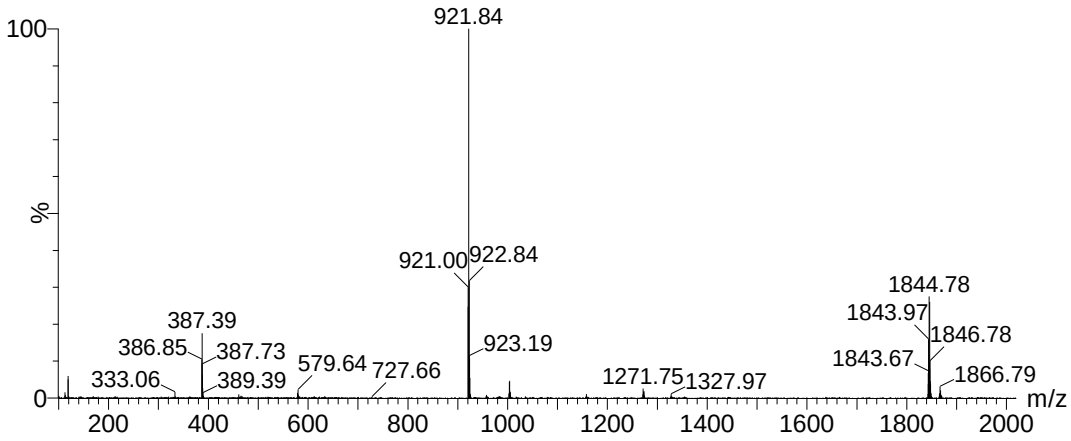

Mass spectrum at 6.60min, 921.8 m/z [M-H]

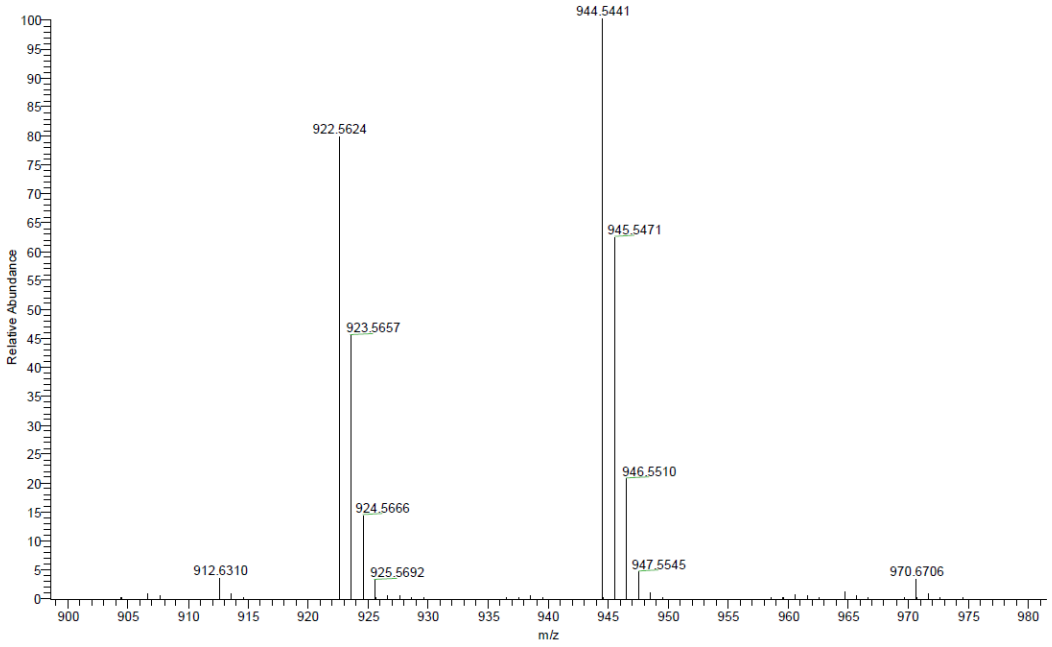

HRMS spectrum of **1**. 922.5624 m/z [M+H]

Compound **2** *Fmoc-Lys(DOTA)-NH₂*

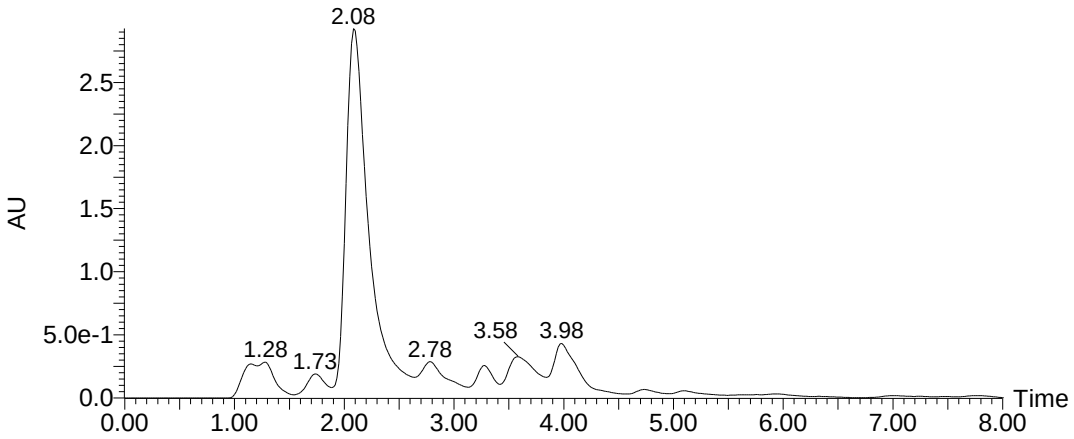

Extracted wavelength chromatogram of 264nm for crude reaction mixture

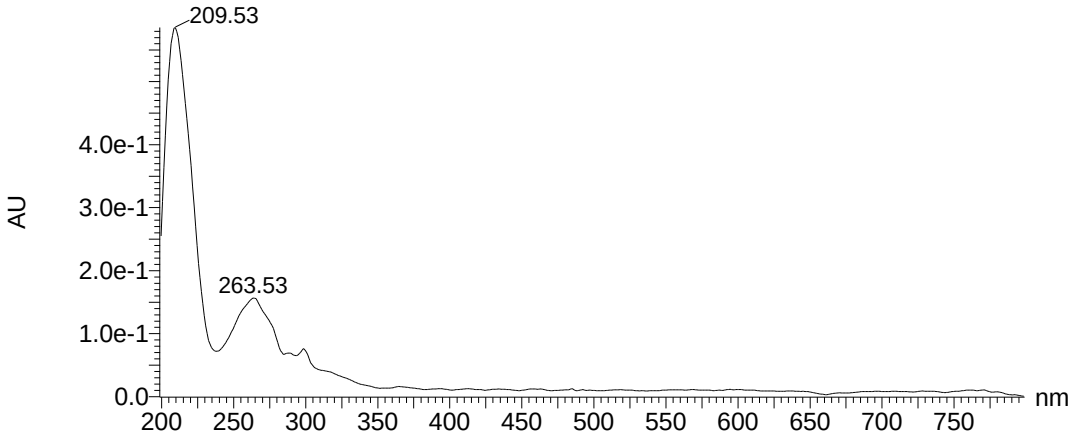

UV-Vis absorption spectrum at 1.93 min with characteristic peak at 263nm for Fmoc protecting group

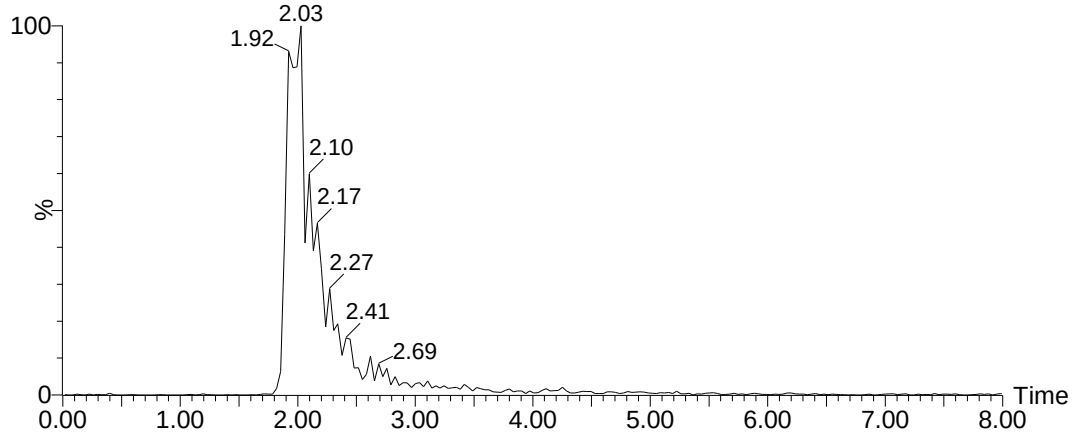

XIC of 752.6 m/z

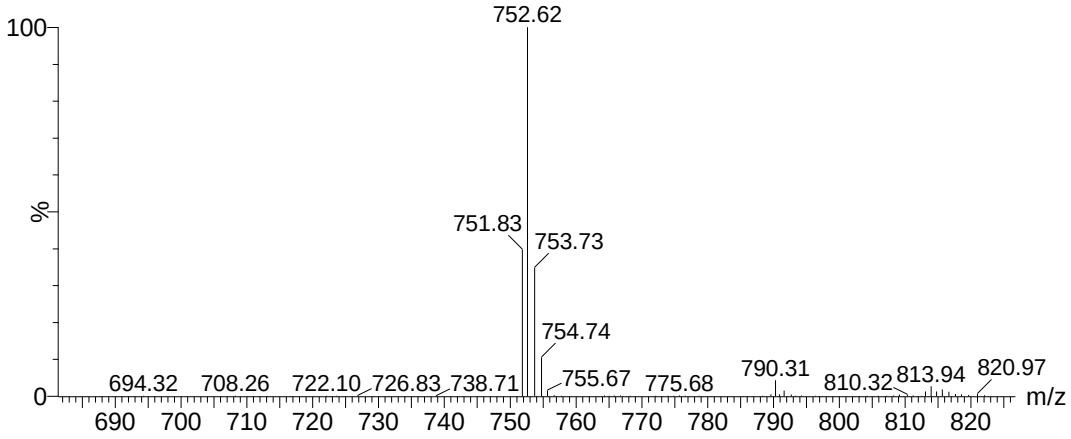

Mass spectrum at 1.99 minutes. 752.6 m/z [M-H]

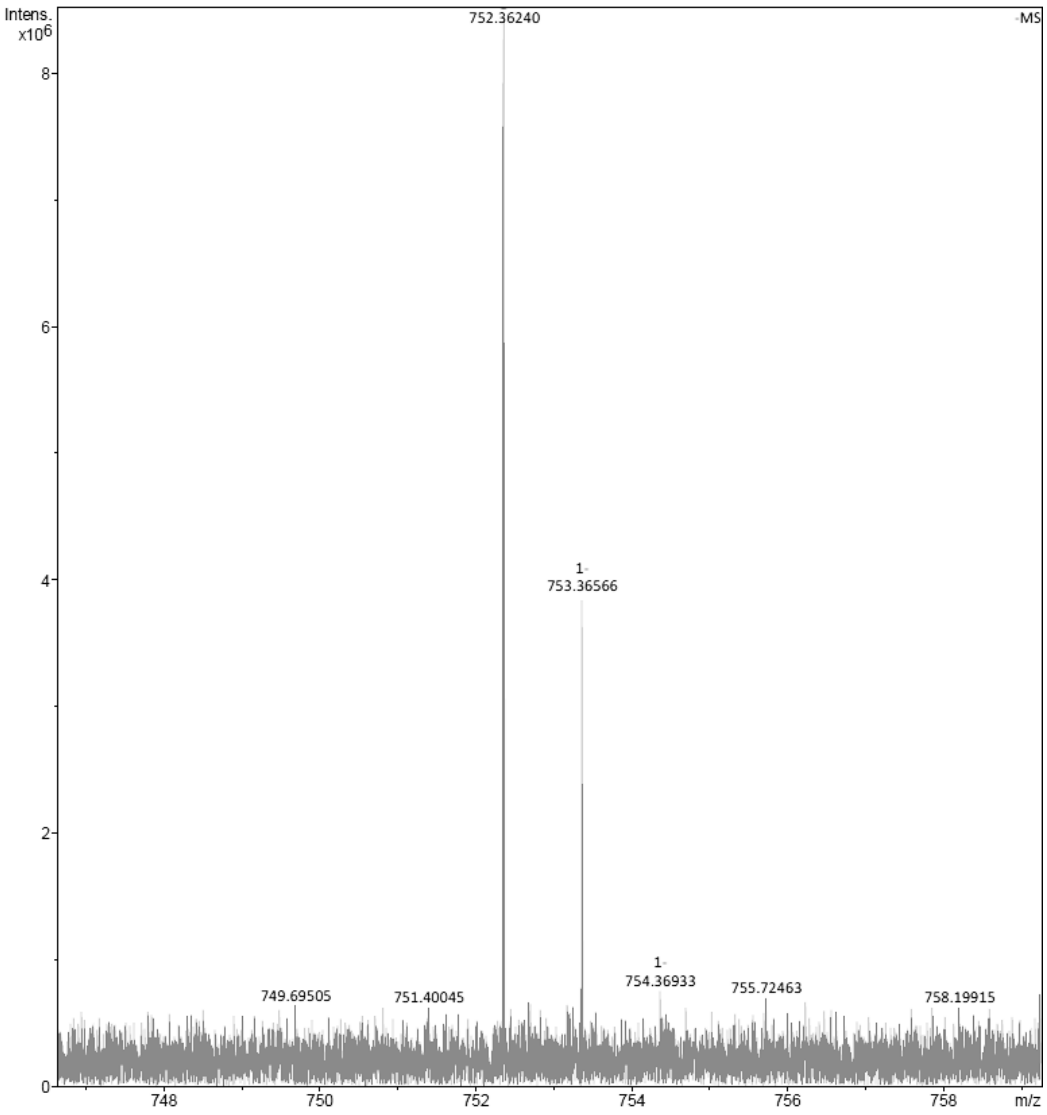

HRMS of **2**. 752.3624 m/z [M-H]

Compound **3a** *Fmoc-Lys(DOTA-Gd)-NH₂*

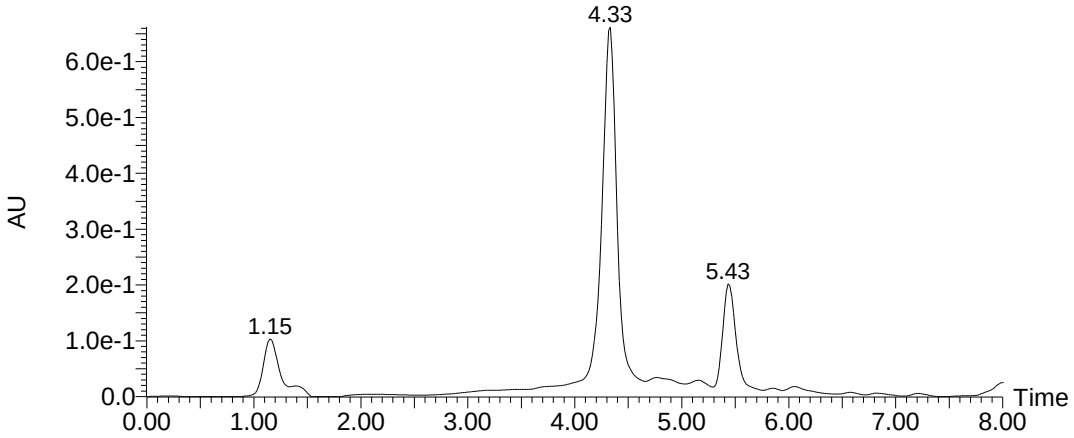

Extracted wavelength chromatogram of 263 nm for crude reaction mixture

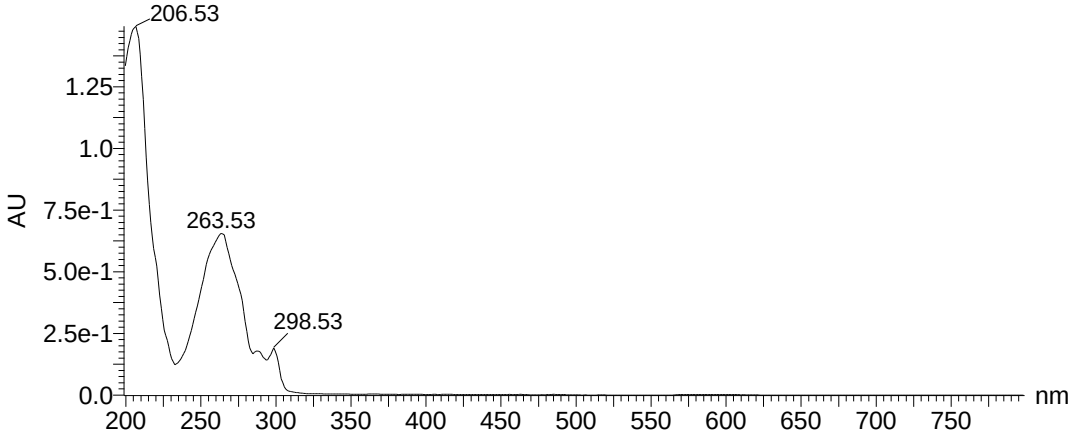

UV-Vis absorption spectrum at 4.32 min with characteristic peak at 263nm for Fmoc protecting group

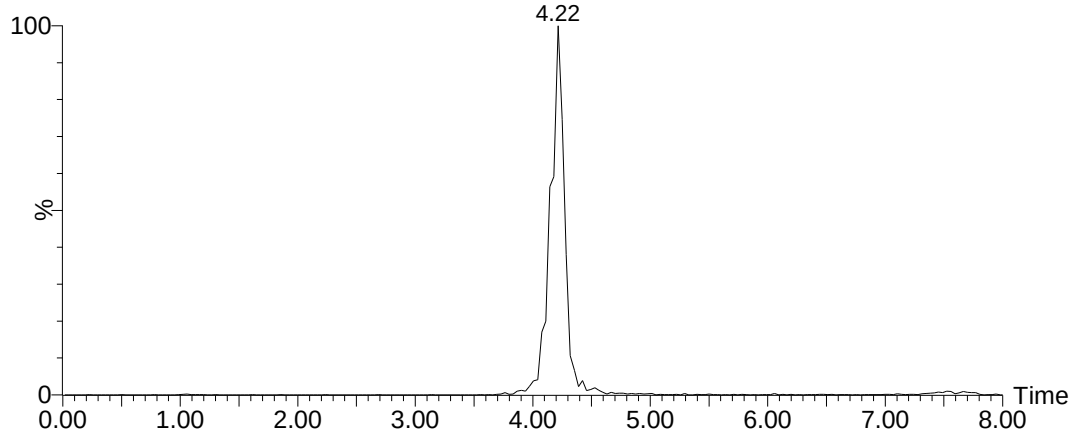

XIC of mass range of 904.1 to 909.7 m/z

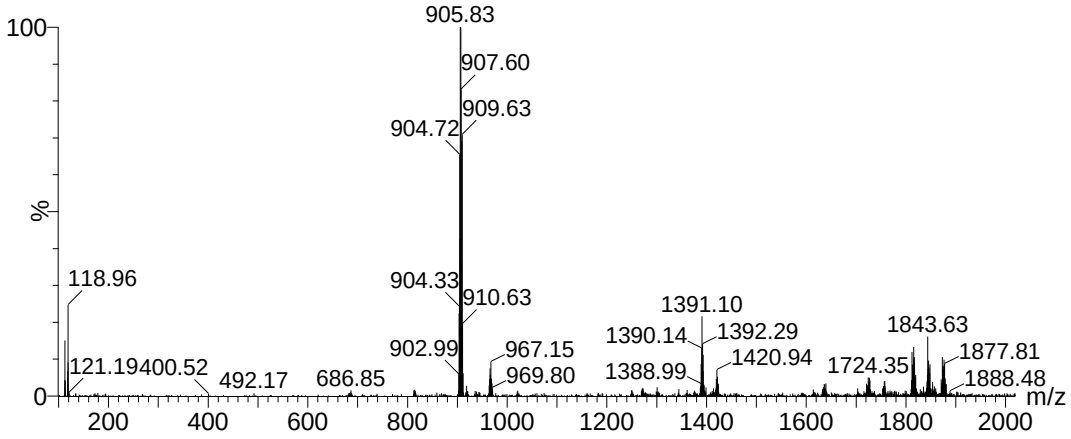

Mass spectrum at 4.21 minutes. 905.8 m/z [M-H]

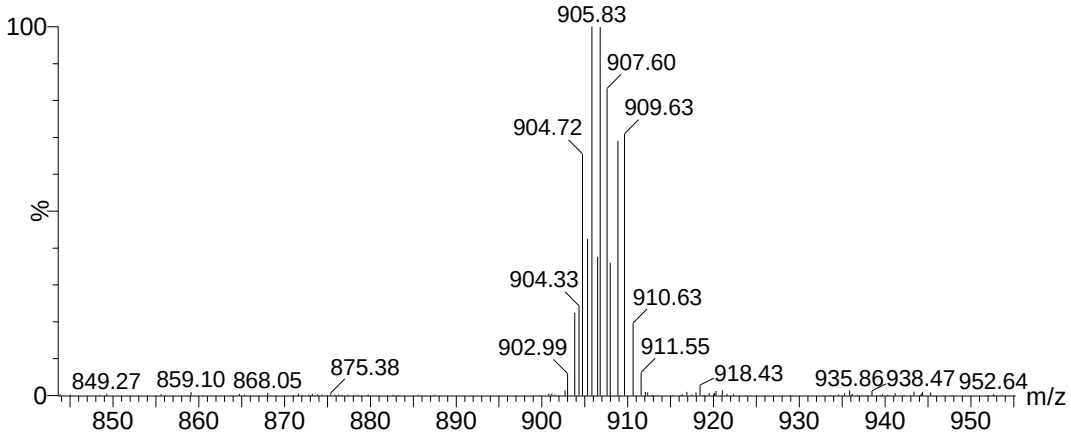

Expanded parent ion from spectrum above, demonstrating Gd isotope pattern

Compound **3b** *Fmoc-Lys(DOTA-Gd)-NH₂*

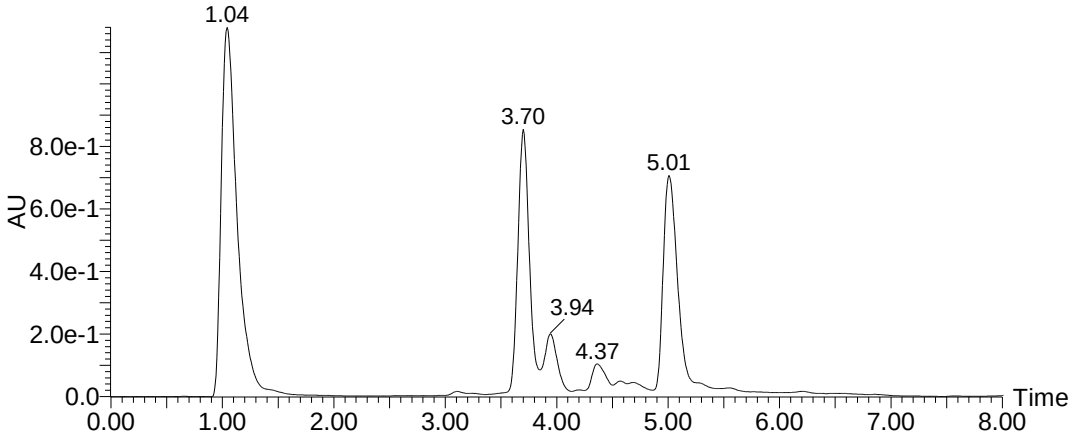

Extracted wavelength chromatogram of 263 nm for crude reaction mixture

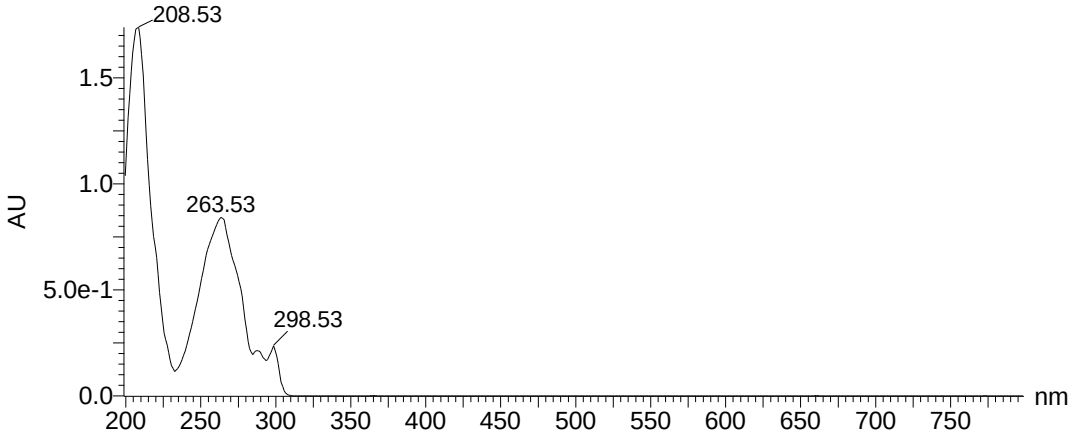

UV-Vis absorption spectrum at 3.70 min with characteristic peak at 263nm for Fmoc protecting group

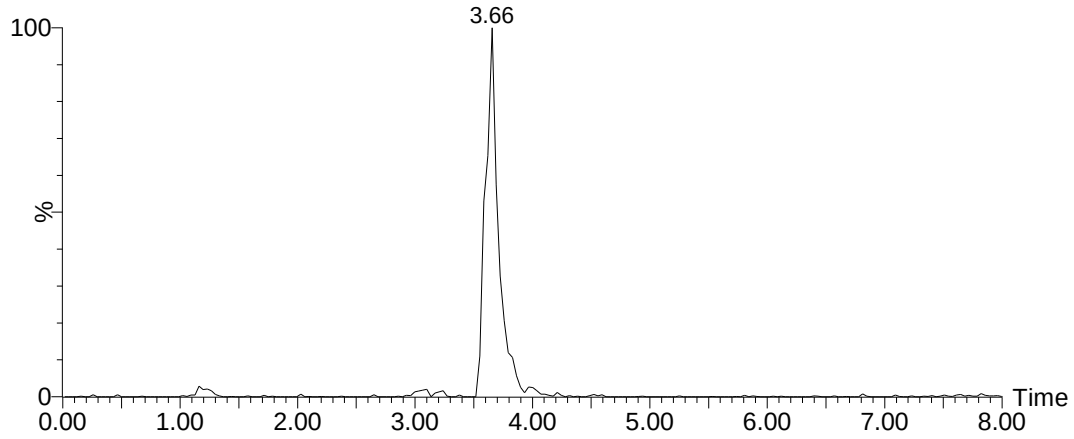

XIC of mass range of 905.3 to 909.7 m/z

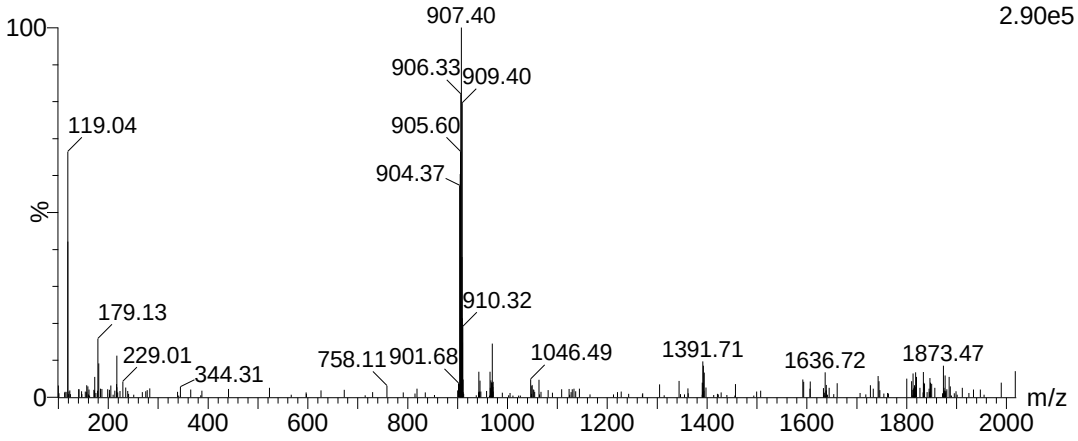

Mass spectrum at 3.59 minutes. 907.4 m/z [M-H]

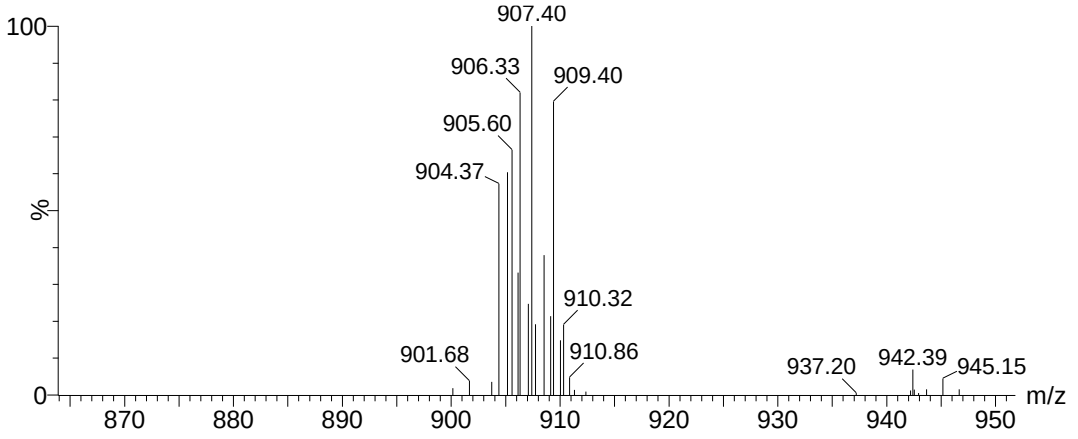

Expanded parent ion from spectrum above, demonstrating Gd isotope pattern

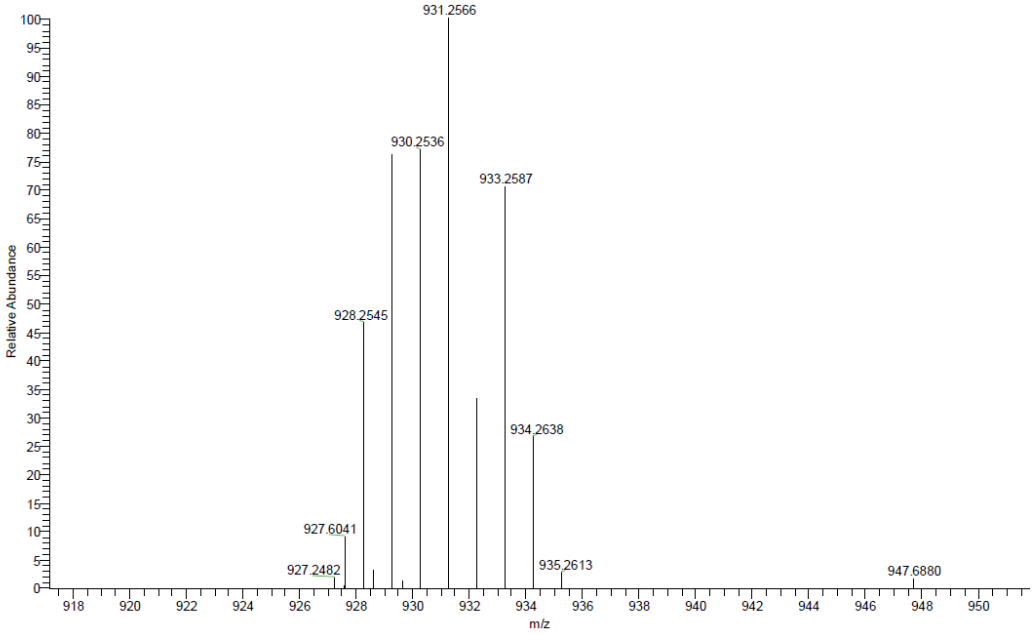

HRMS of **3b**. 931.2566 m/z [M+Na]

Compound **4** *H-Lys(DOTA-Gd)-NH₂*

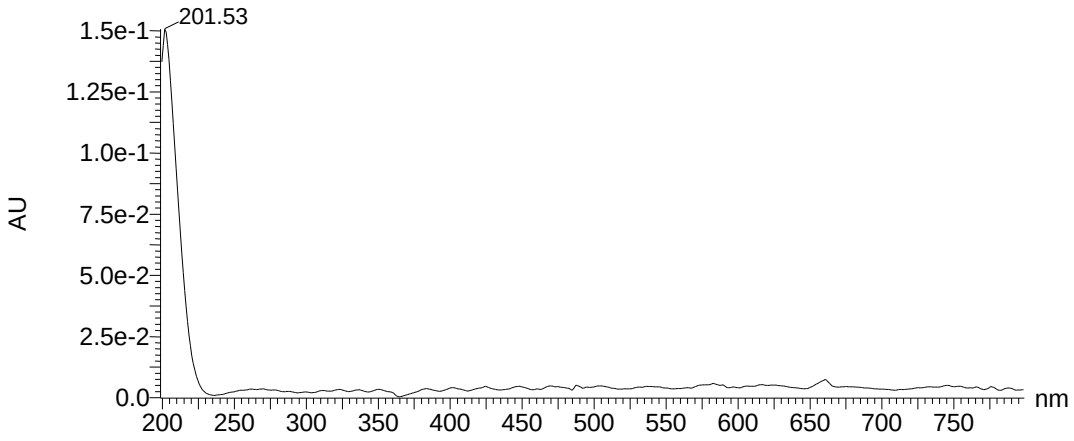

UV-Vis absorption spectrum at 1.23 minutes, demonstrating the lack of characteristic Fmoc absorption

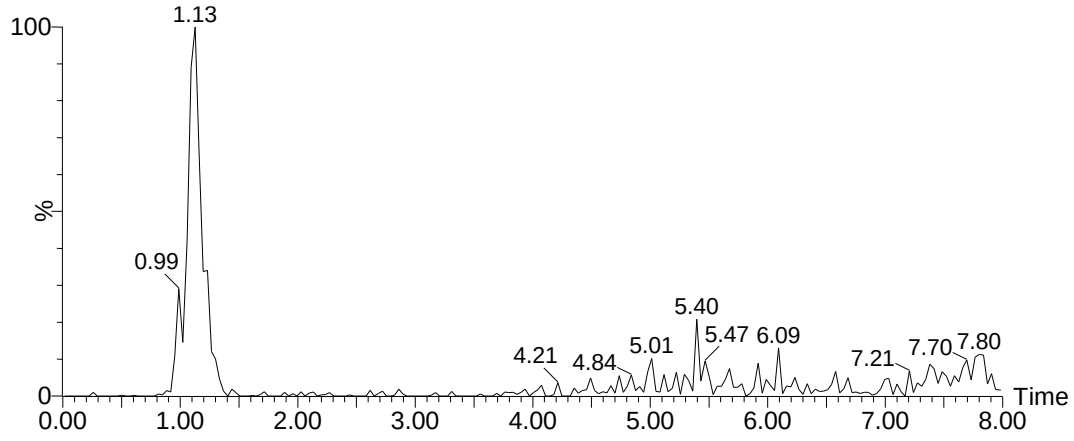

XIC of mass range of 682.0 to 687.6 m/z

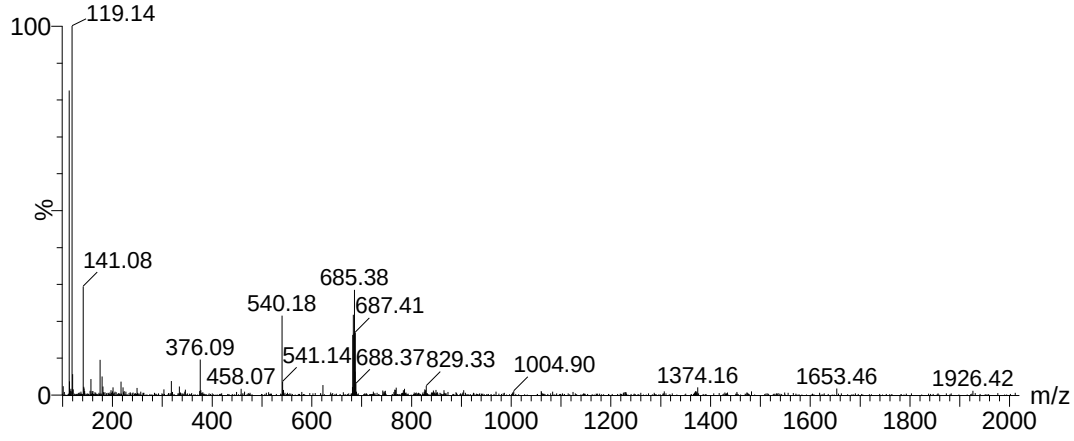

Mass spectrum at 1.13 minutes, 685.4 m/z [M-H]

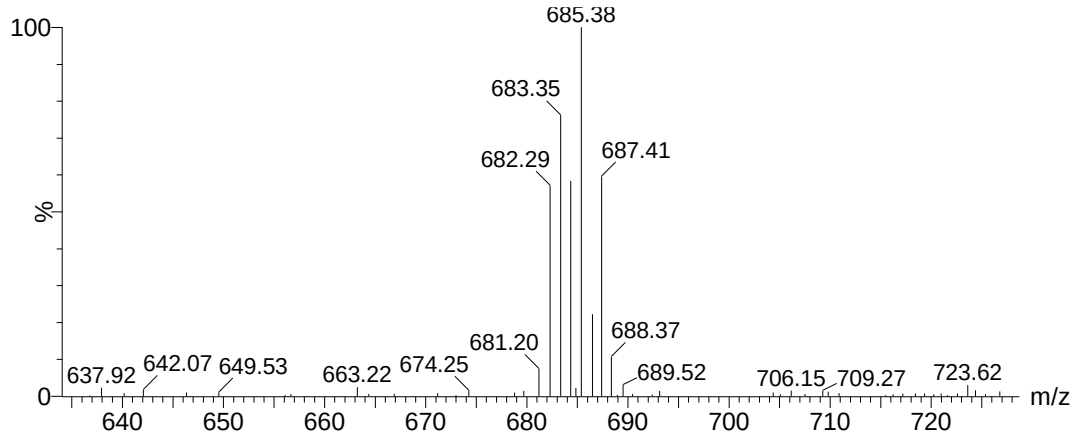

Expanded parent ion from spectrum above, demonstrating Gd isotope pattern

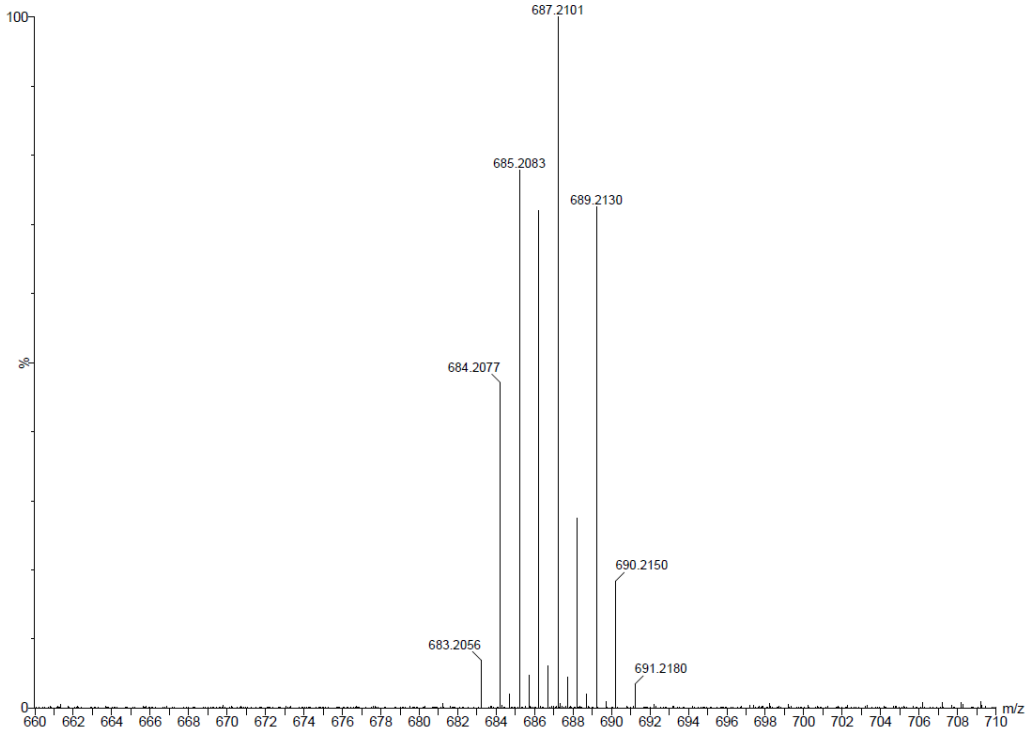

HRMS of **4**. 687.2101 m/z [M+H]

Compound **5** *Fmoc-dLys(DOTA-La)-OH*

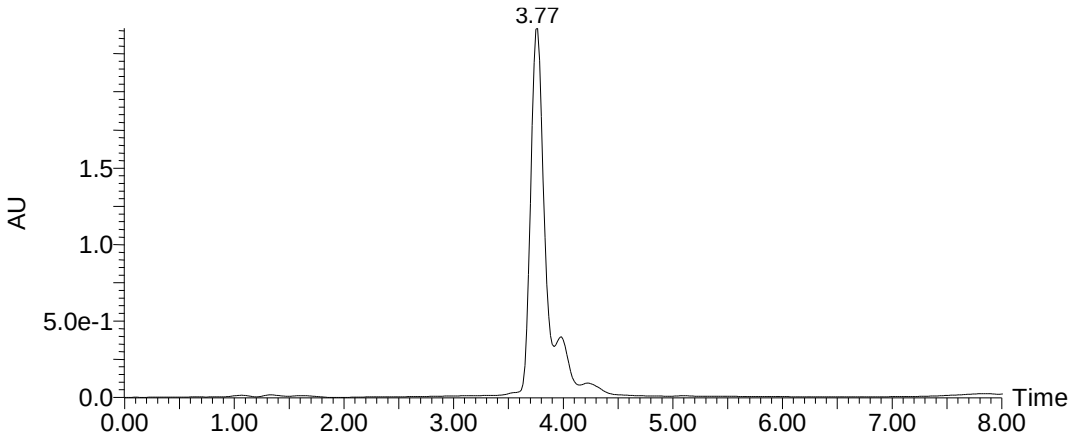

Extracted wavelength chromatogram of 263nm for purified sample of **5**

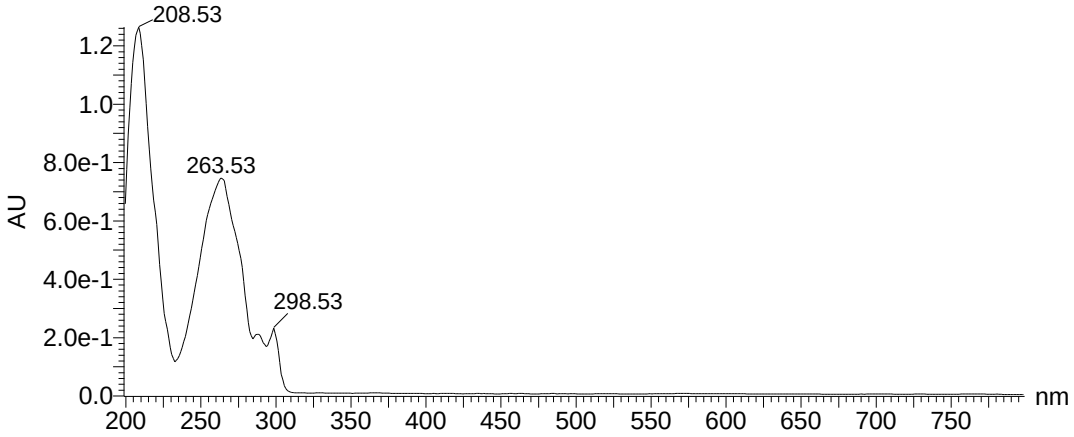

UV-Vis absorption spectrum at 3.85 min with characteristic peak at 263nm for Fmoc protecting group

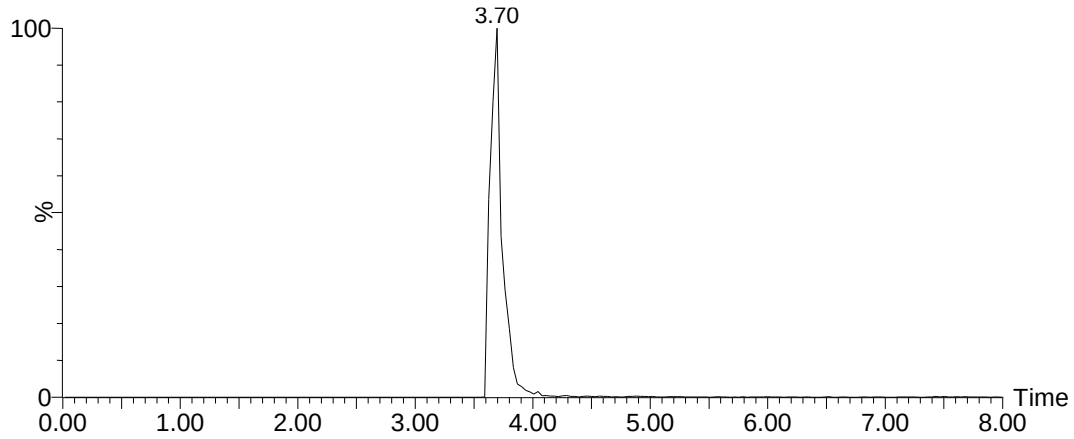

XIC of 889.4 m/z

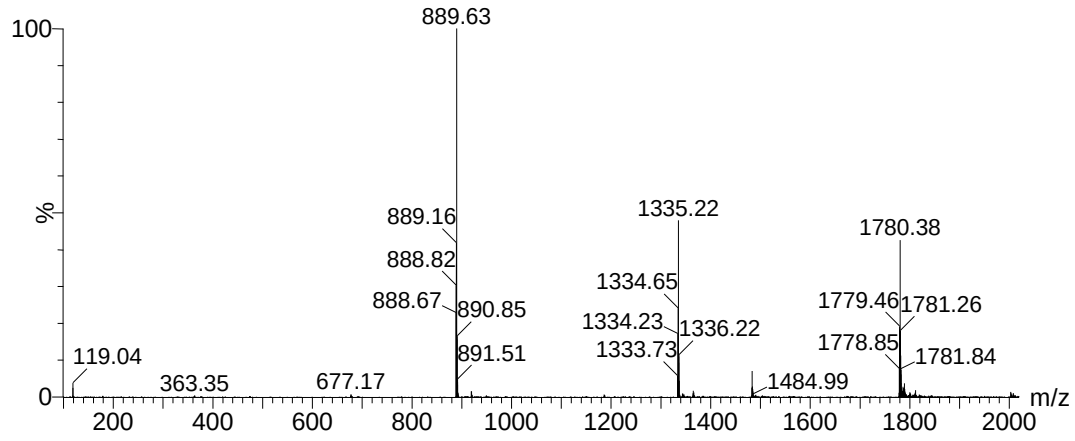

Mass spectrum at 3.70 minutes, 889.6 m/z [M-H].

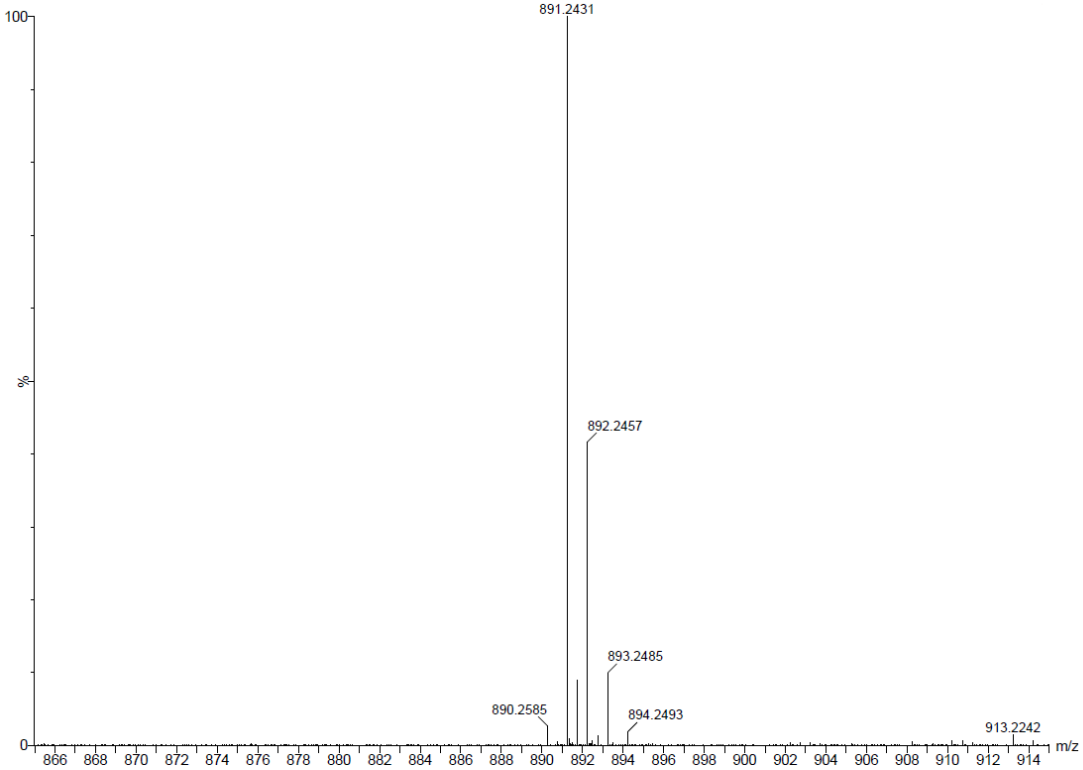

HRMS of **5**. 891.2431 m/z [M+H]

Compound **6** *Fmoc-dLys(DOTA-Gd)-OH*

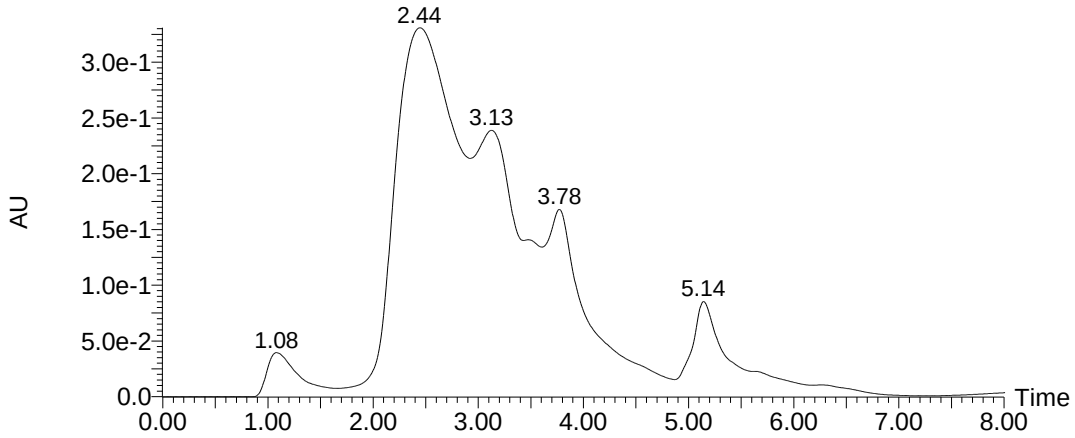

Extracted wavelength chromatogram for 266nm of crude reaction mixture

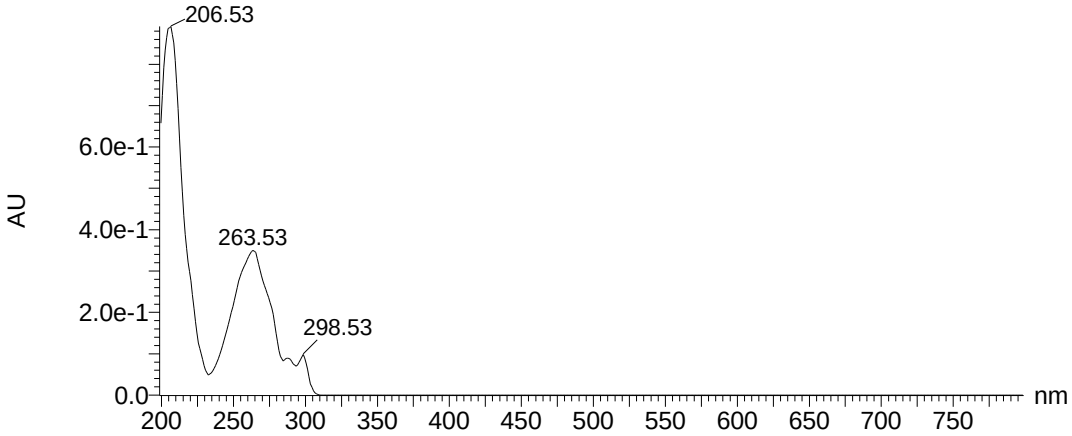

UV-Vis absorption at 2.12 minutes with characteristic peak at 263nm for Fmoc protecting group

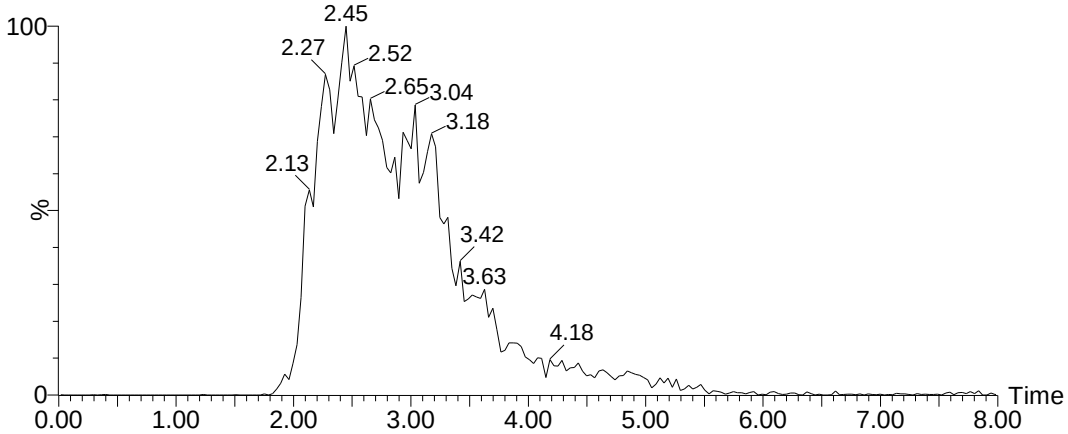

XIC of mass range 905.6 to 911.8 m/z [M-H]

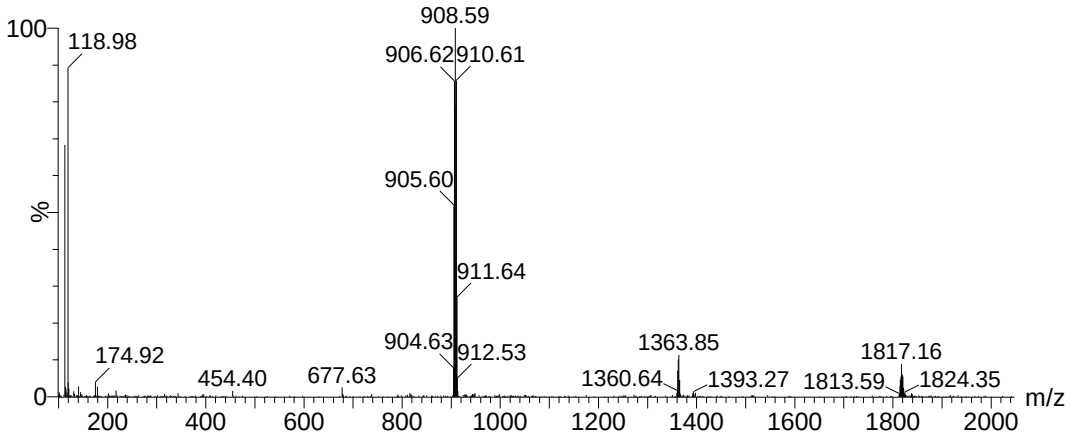

Mass spectrum at 2.00 minutes, 906.7 m/z [M-H]

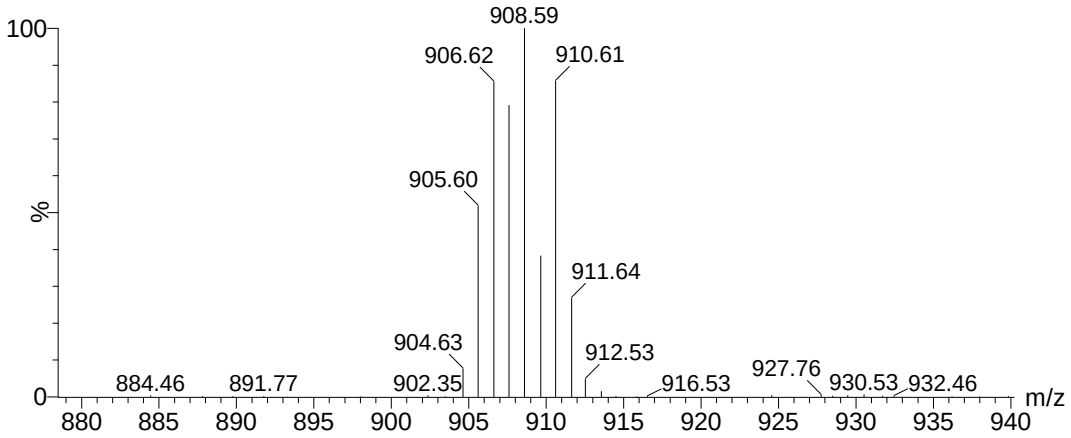

Expanded parent ion of mass spectrum above, demonstrating Gd isotope pattern

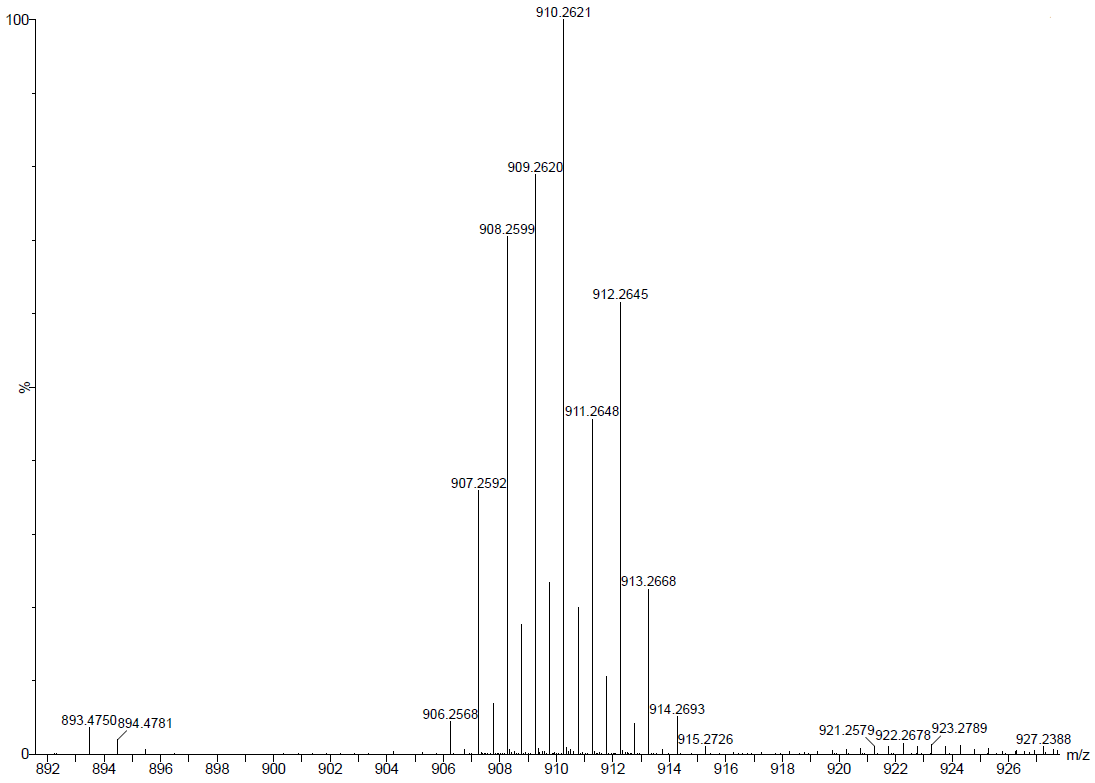

HRMS of **6**. 910.2621 m/z [M+H]

Compound **7** *Fmoc-dLys(DOTA-La)-K(DOTA-Gd)-NH_2*

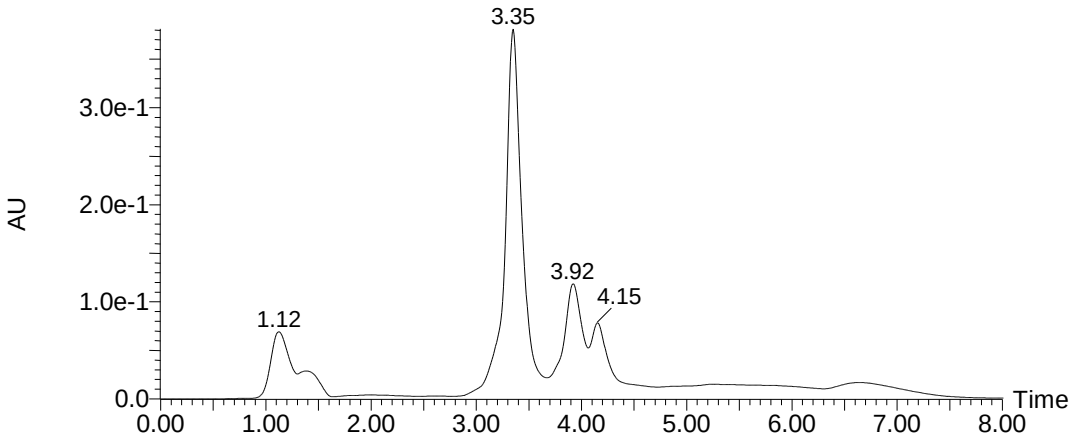

Extracted wavelength chromatogram of 263nm for crude reaction mixture

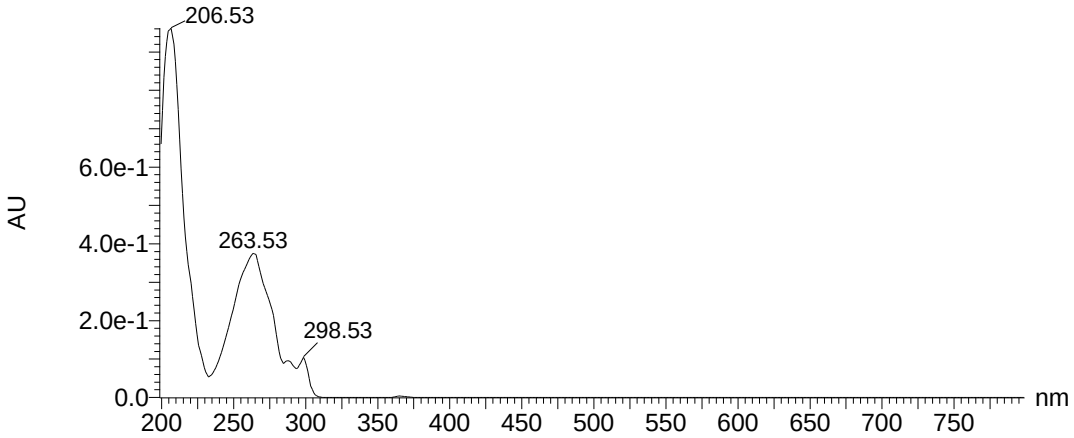

UV-Vis absorption spectrum at 3.35min with characteristic peak at 263nm for Fmoc protecting group

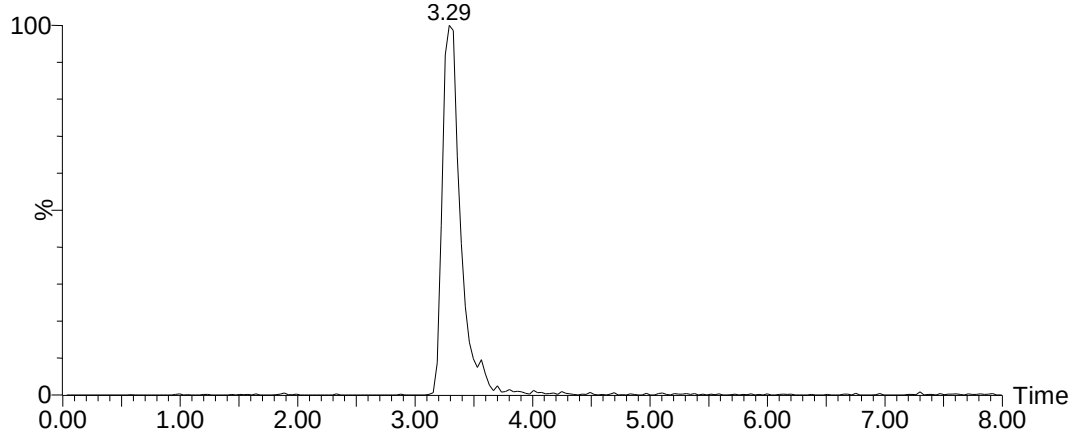

XIC of mass range 778.9 to 781.9 m/z

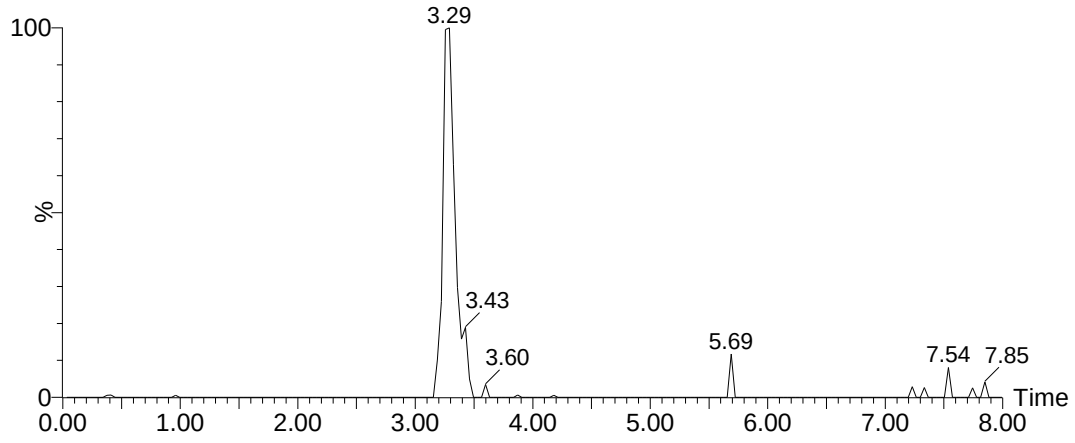

XIC of mass range 1558.0 to 1562.3 m/z

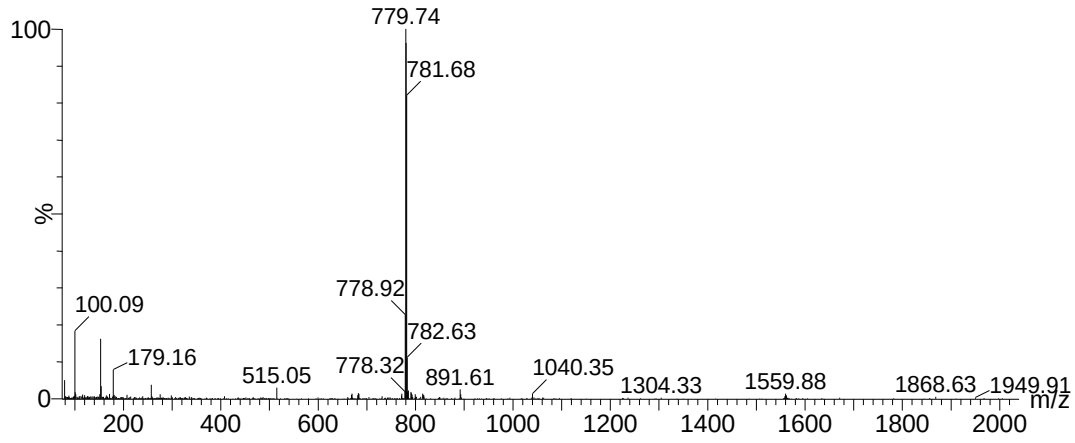

Mass spectrum at 3.26 minutes, 779.7 m/z [M+2H/2], 1559.9 [M+H]

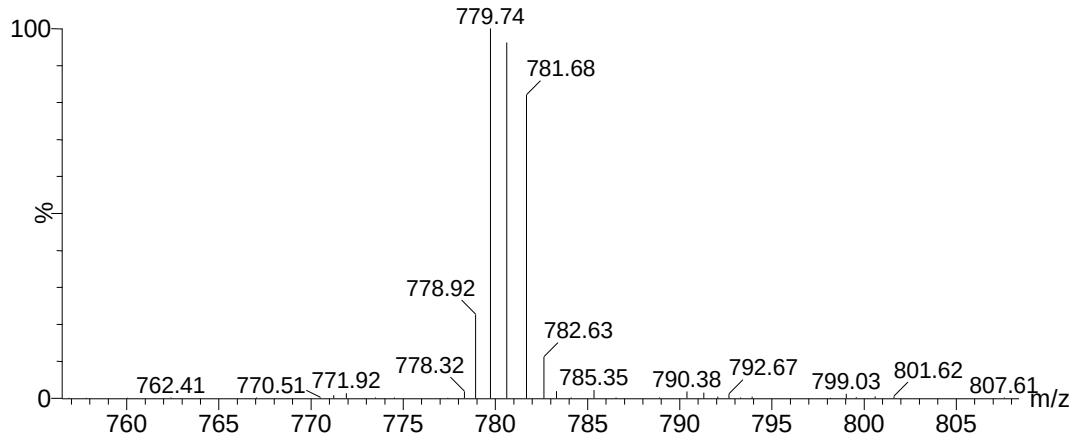

Expanded half-mass ion from spectrum above demonstrating Gd + La isotope pattern

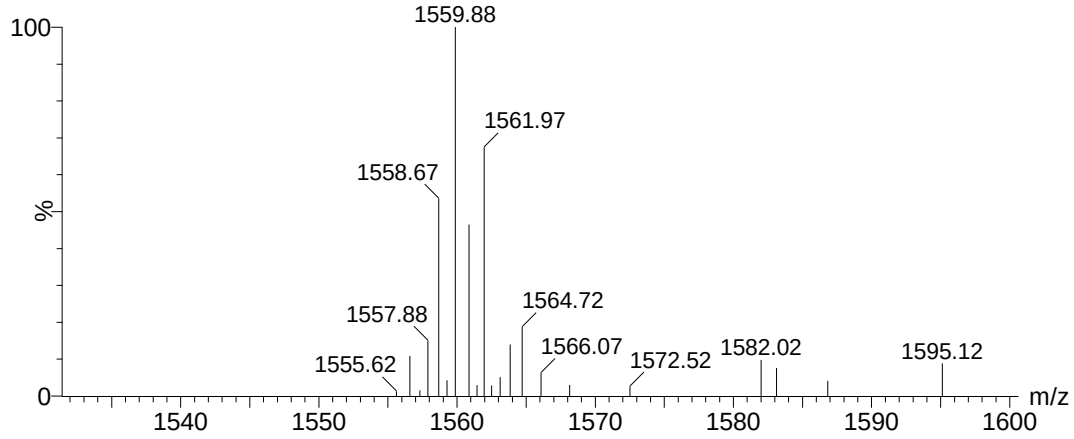

Expanded parent ion from spectrum above demonstrating Gd + La isotope pattern

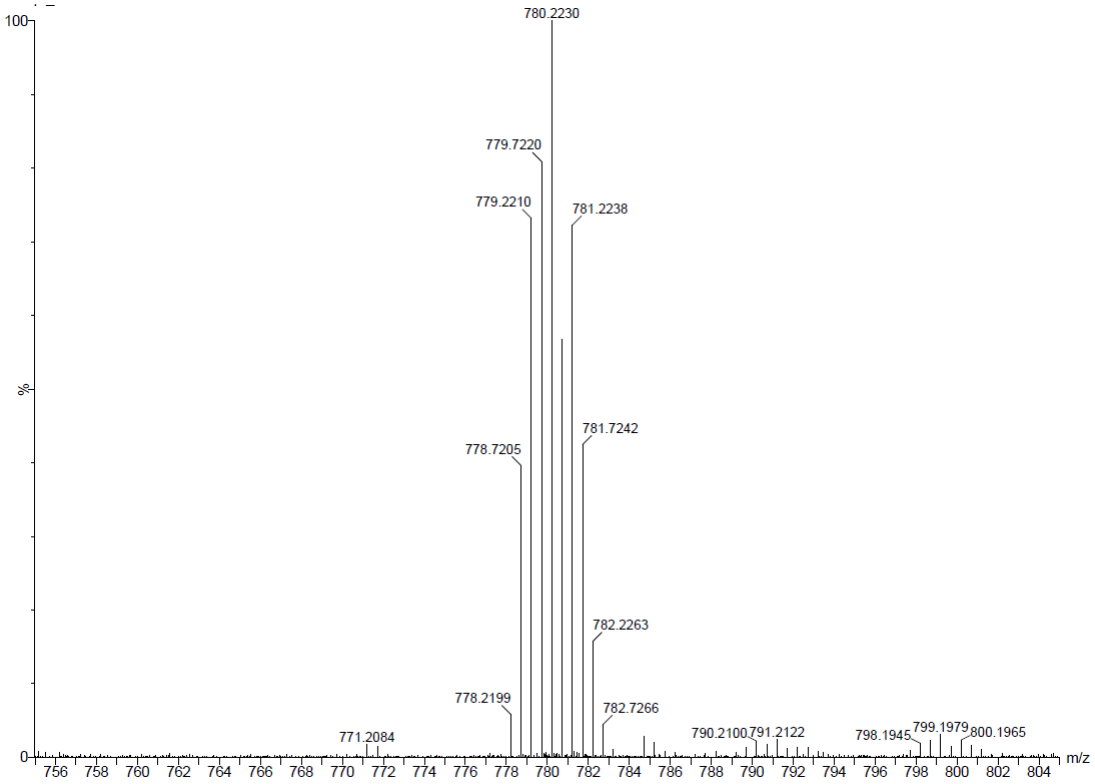

HRMS of **7**. 780.2230 m/z [M+2H/2]

Compound **8** *H-dLys(DOTA-La)-K(DOTA-Gd)-NH₂*

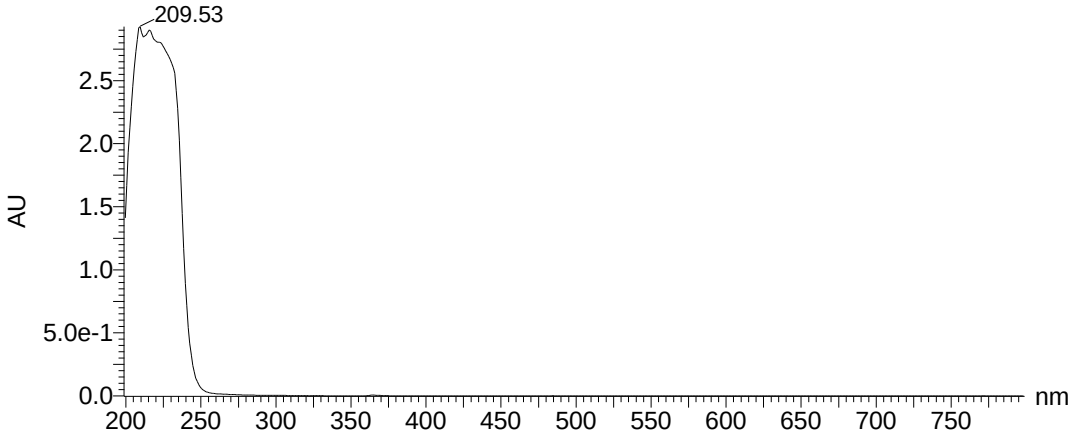

UV-Vis absorption spectrum at 1.25 minutes, demonstrating the lack of characteristic Fmoc absorption

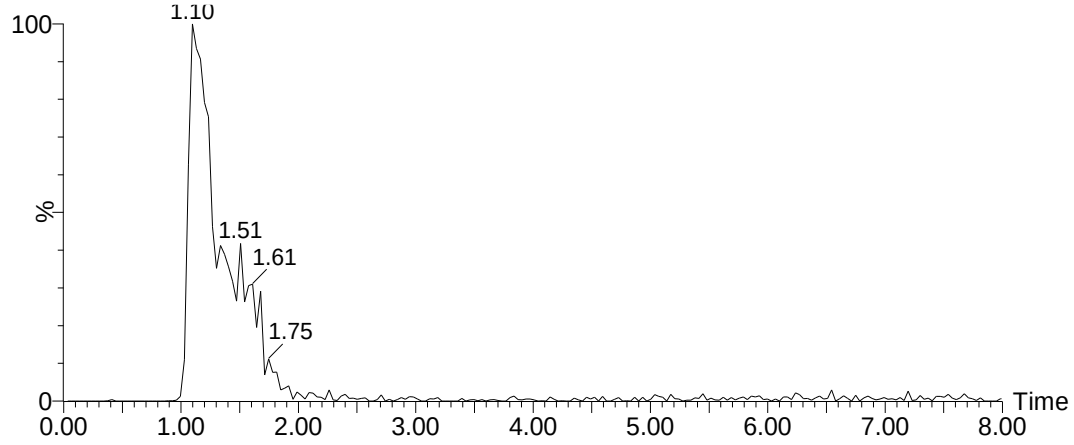

XIC of mass range 667.8 to 671.0 m/z

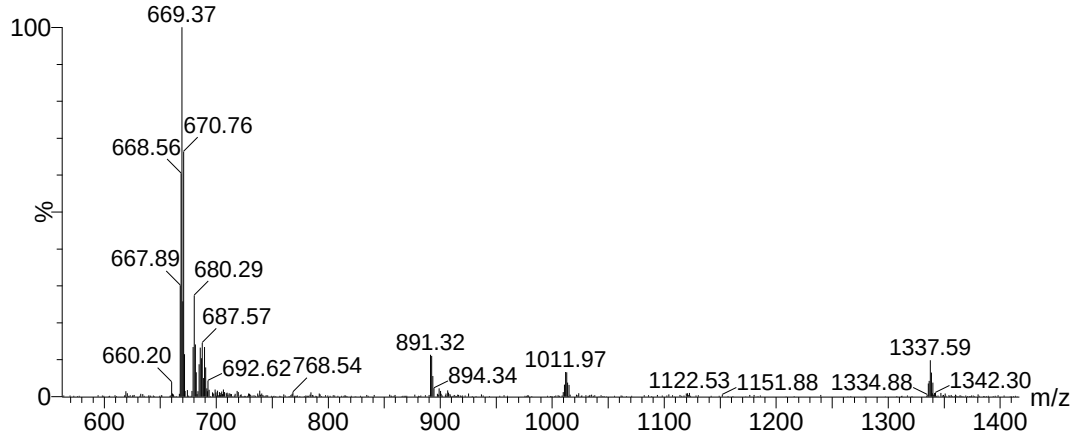

Mass spectrum at 1.20 minutes, 669.4 m/z [M+2H/s], 1337.6 m/z [M+H]

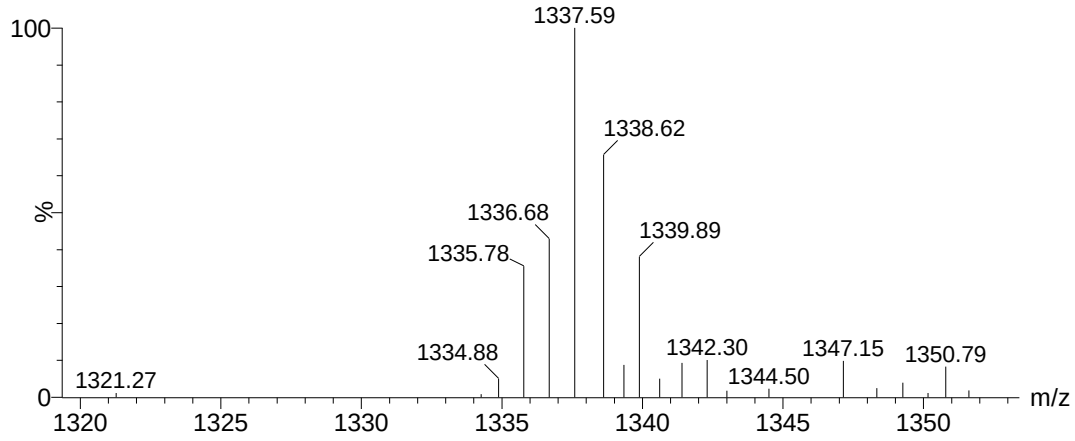

Expanded parent ion from spectrum above, demonstrating Gd + La isotope pattern

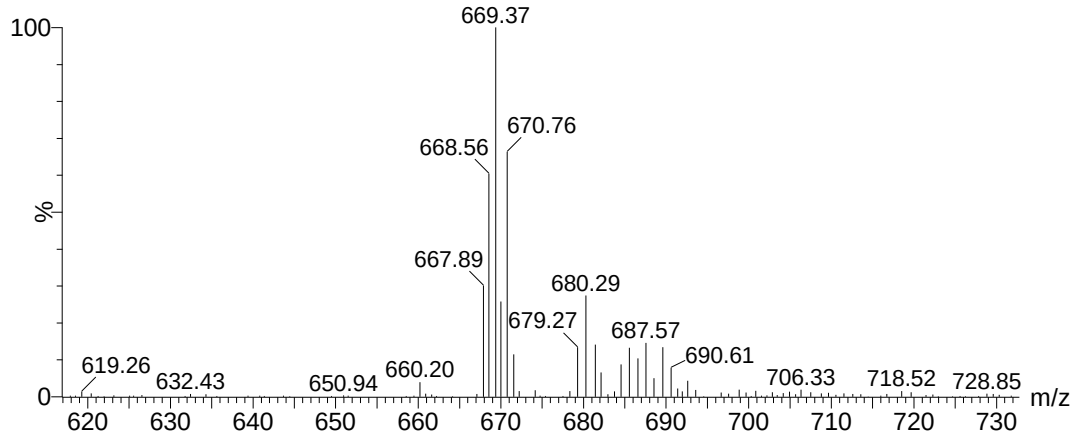

Expanded half-mass ion from spectrum above, demonstrating Gd + La isotope pattern

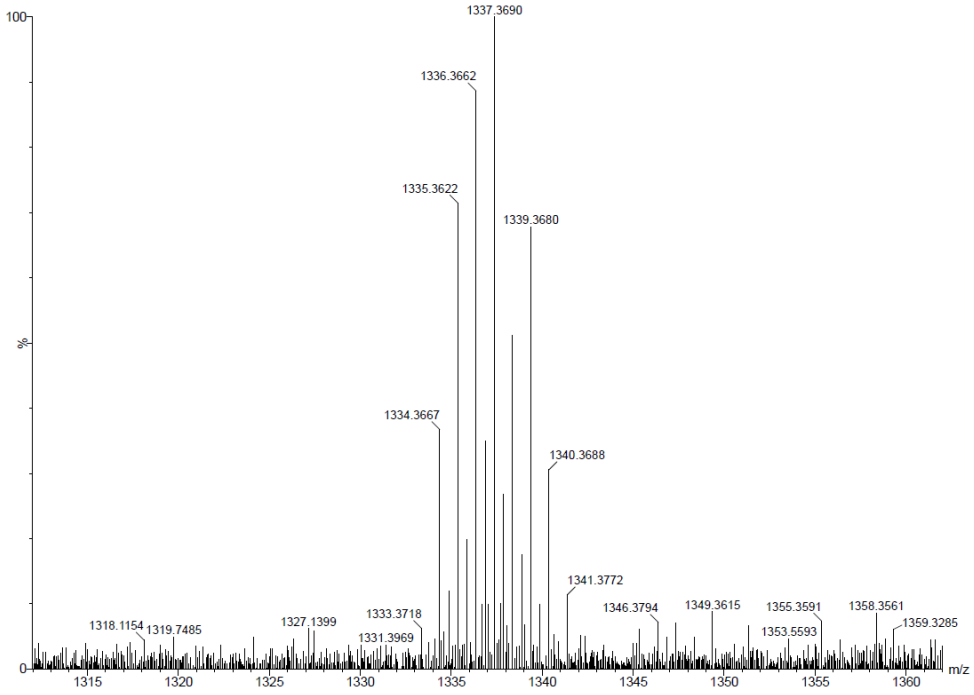

HRMS of **8**. 1337.3690 m/z [M+H]

Compound **9** *DSS-dLys(DOTA-La)-Lys(DOTA-Gd)-NH₂*

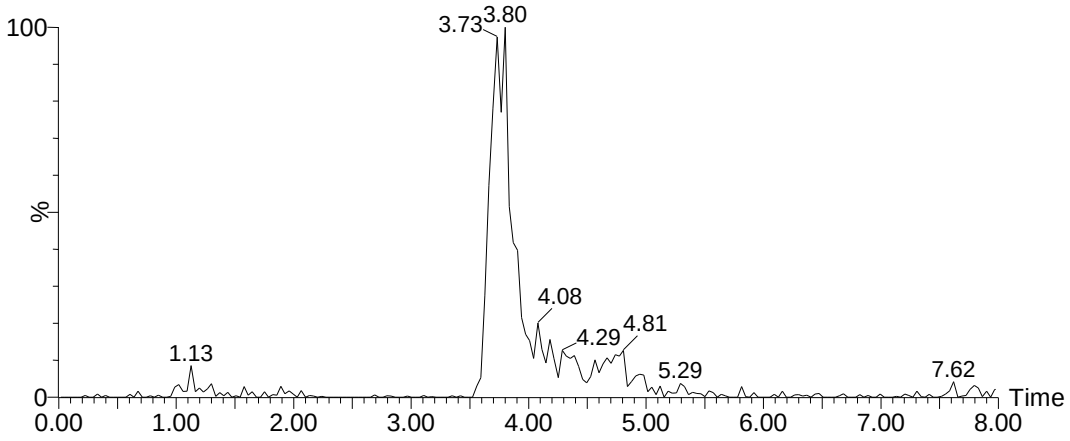

XIC of mass range 1543.6 to 1550.1 m/z

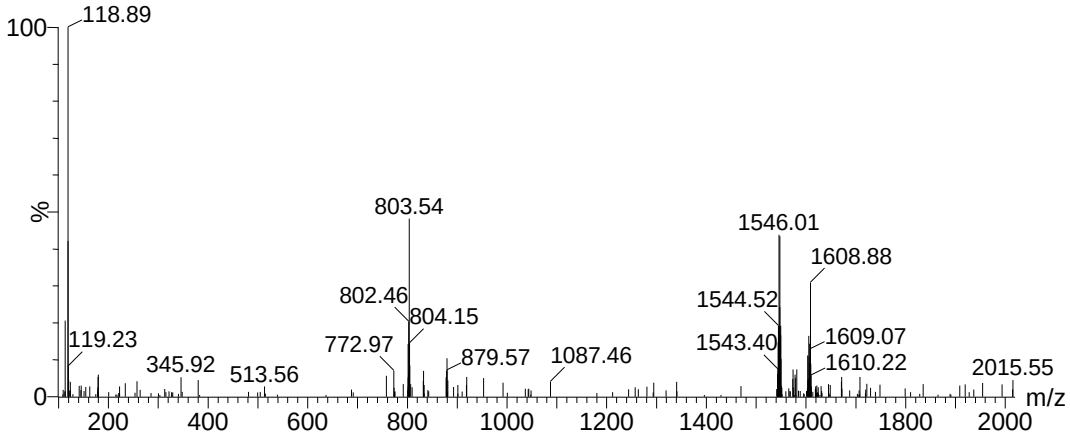

Mass spectrum at 3.73 minutes, 1546.0 m/z [M-H] of **9** after treatment with butylamine

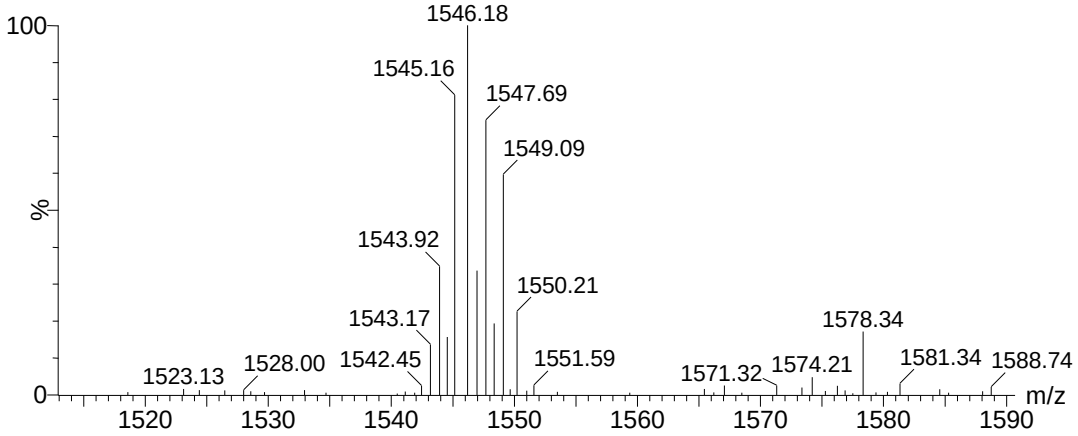

Expanded parent ion from mass spectrum above, demonstrating Gd + La isotope pattern

Compound **10** *SMCC-dLys(DOTA-La)-K(DOTA-Gd)-NH₂*

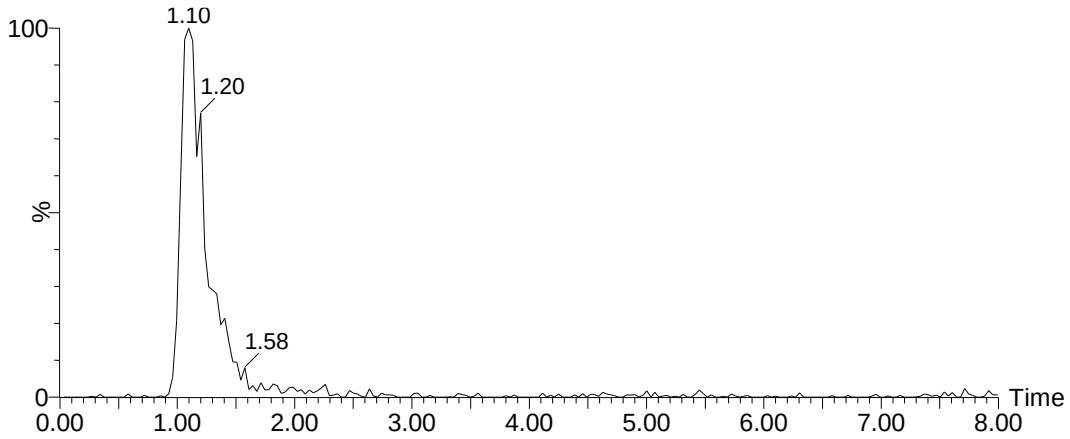

XIC of mass range 777.3 to 780.6 m/z

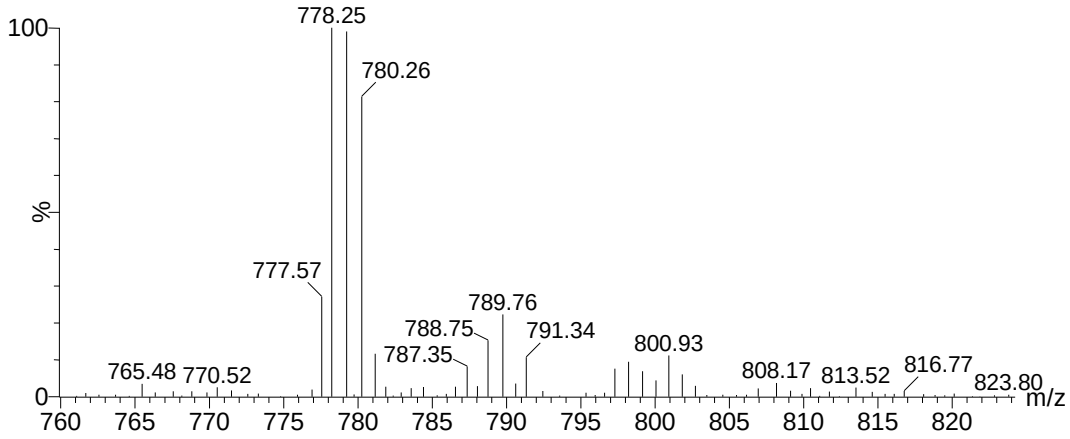

Mass spectrum at 1.12 minutes, 778.3 [M+2H/2]

Compound **11** *c(RGDyK)-DSS-K(DOTA-Gd)-NH₂*

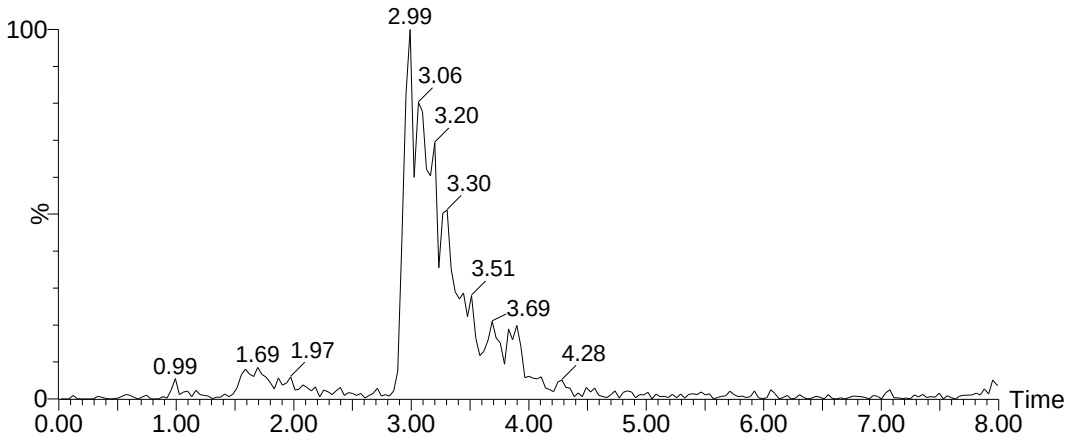

XIC of mass range 1044.4 to 1047.9 m/z

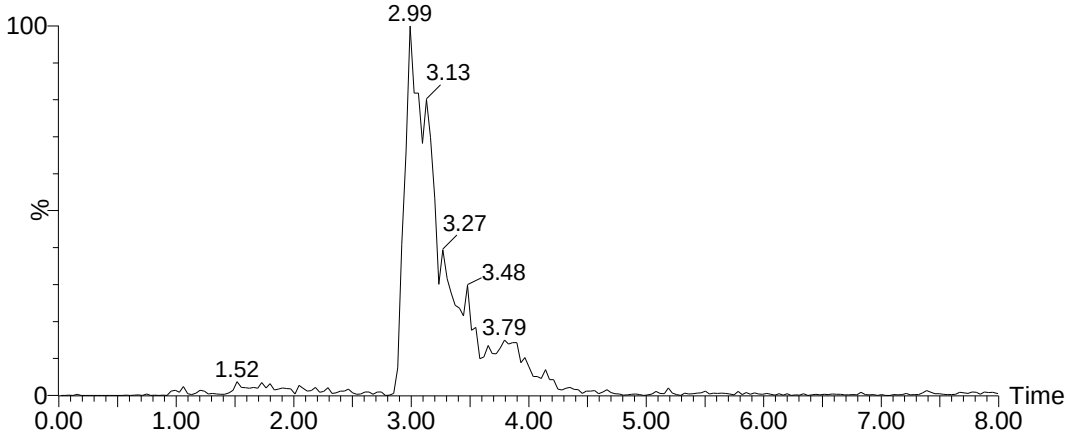

XIC of mass range 1074.1 to 2078.8 m/z

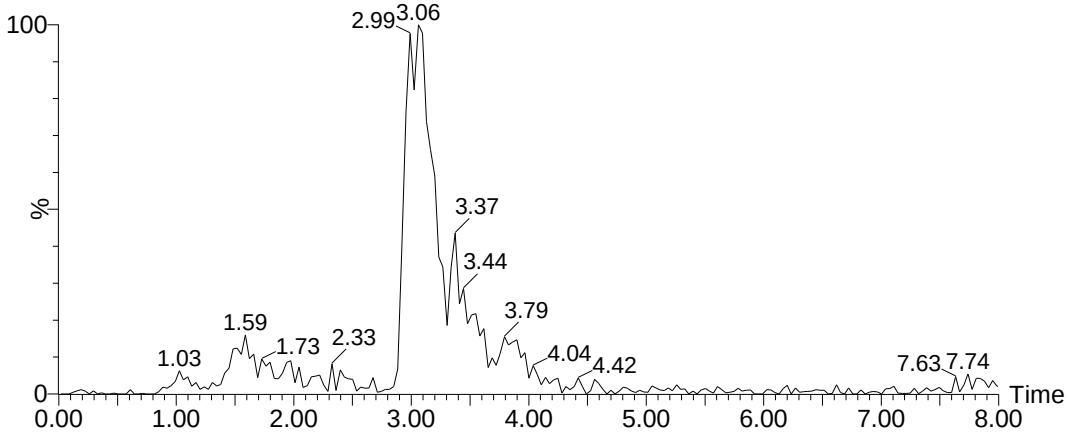

XIC of mass range 1103.9 to 1108.1 m/z

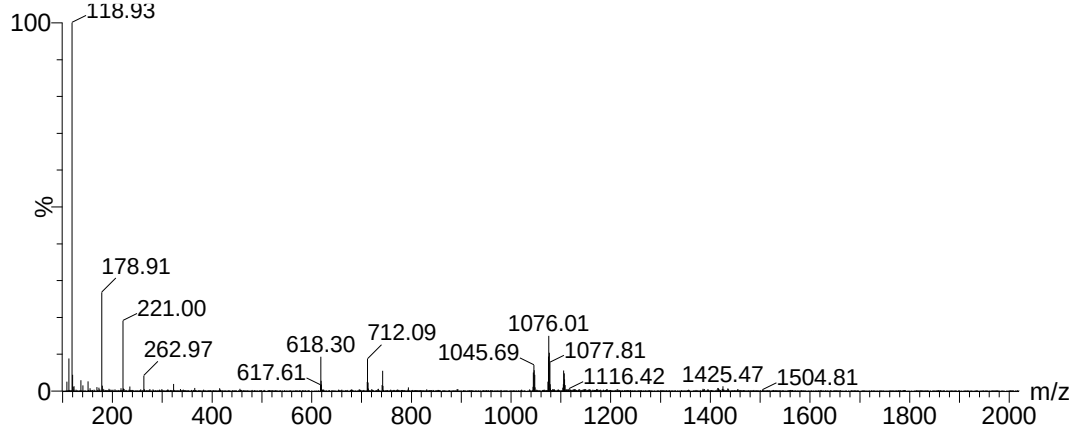

Mass spectrum at 2.99 minutes, 1045.7 m/z [M-2H/2]

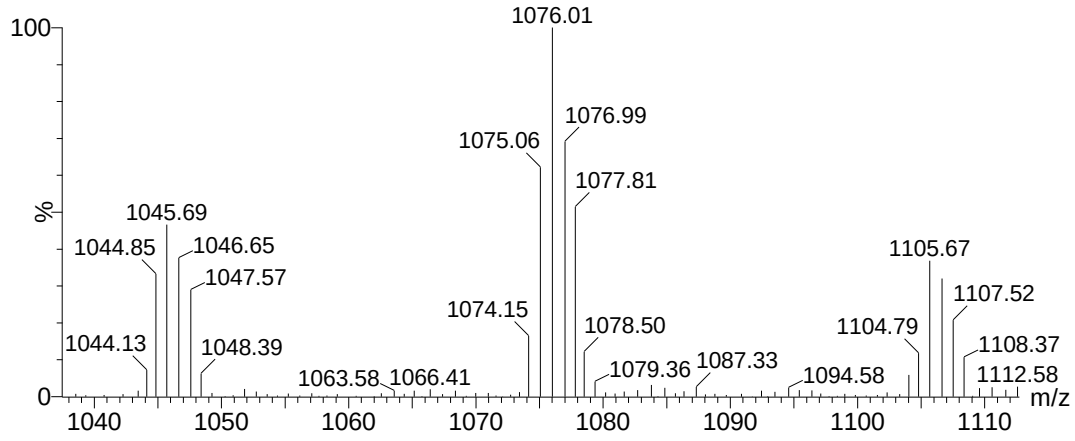

Expanded half mass and adduct ions from spectrum above, 1045.7 m/z [M-2H/2], 1076.0 m/z [M-H+OAc$^-$/2], 1105.7 m/z [M+2OAc$^-$/2]

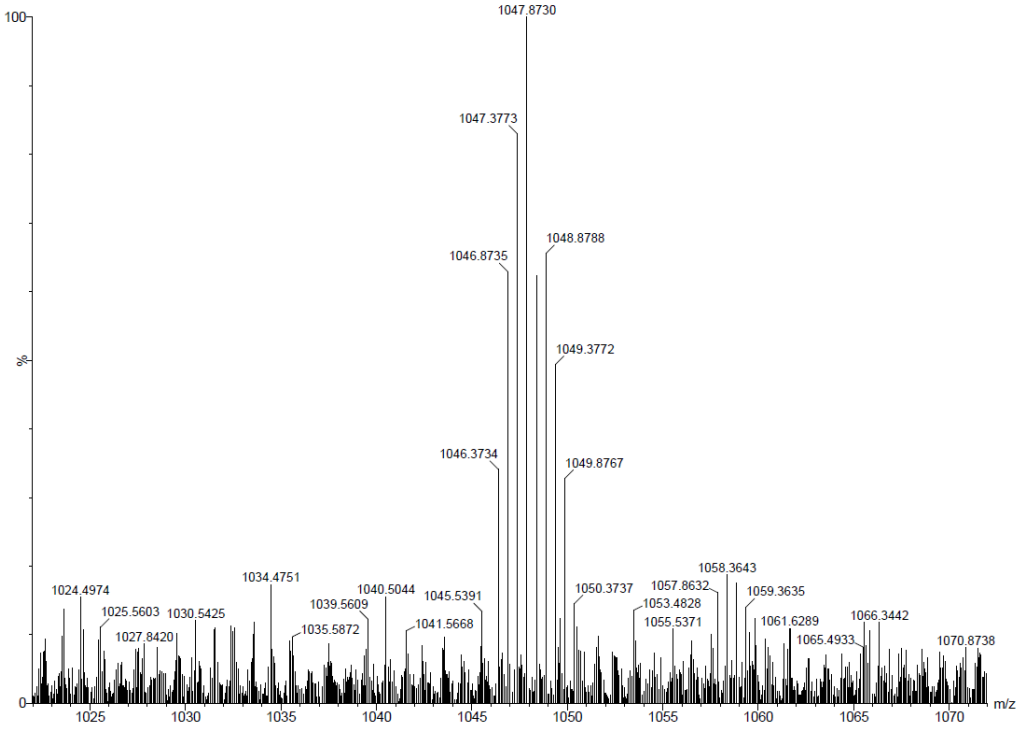

HRMS of **11**, 1047.8730 m/z [M+2H/2]

Compound **12** *c(RGDyK)-SMCC-dLys(DOTA-La)-Lys(DOTA-Gd)-NH₂*

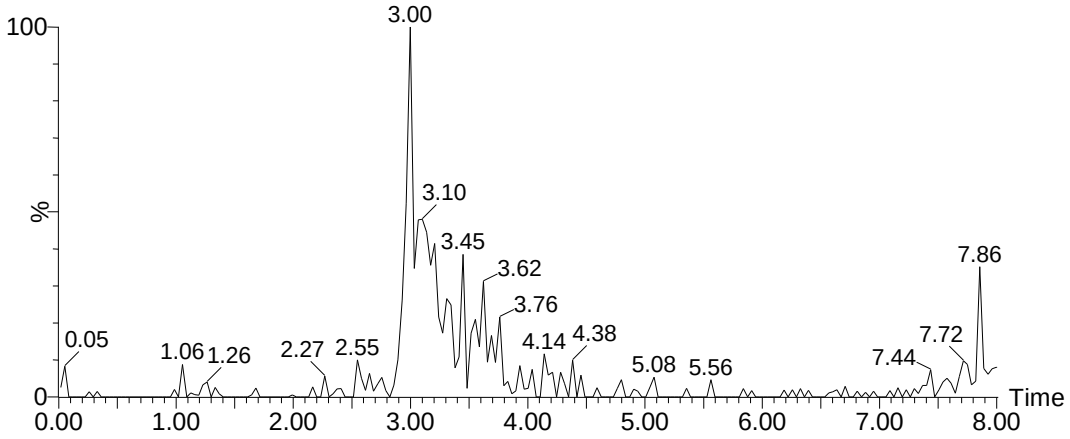

XIC of mass range 1085.1 to 1089.4 m/z

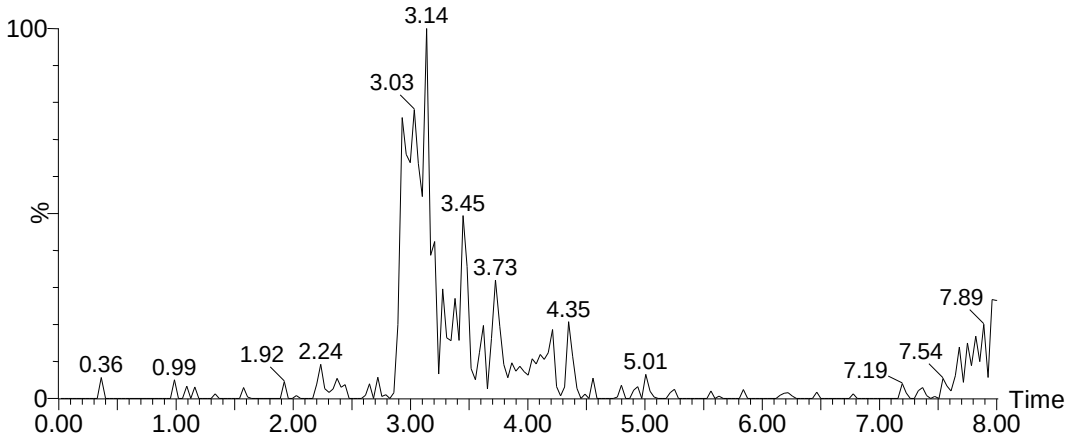

XIC of mass range 1114.7 to 1119.7 m/z

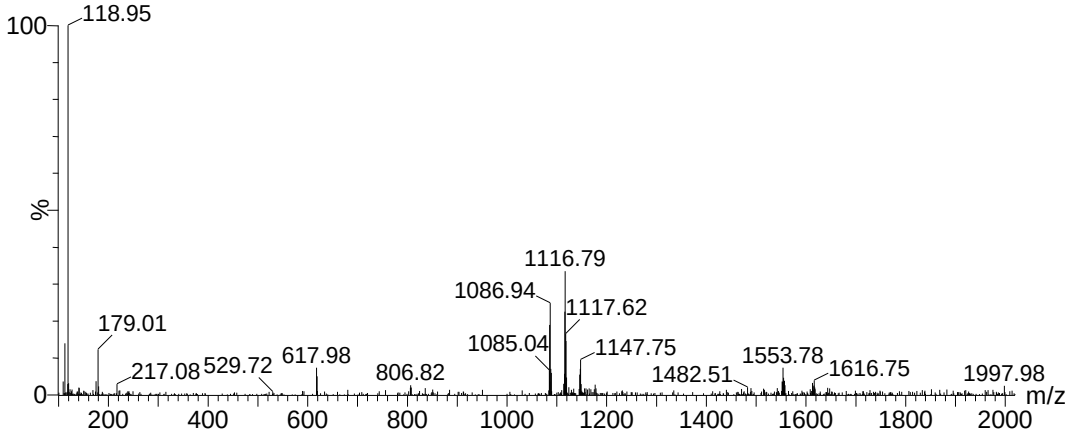

Mass spectrum at 3.03 minutes, 1086.9 m/z [M-2H/2], 1116.8 m/z [M-H+OAc$^-$/2]

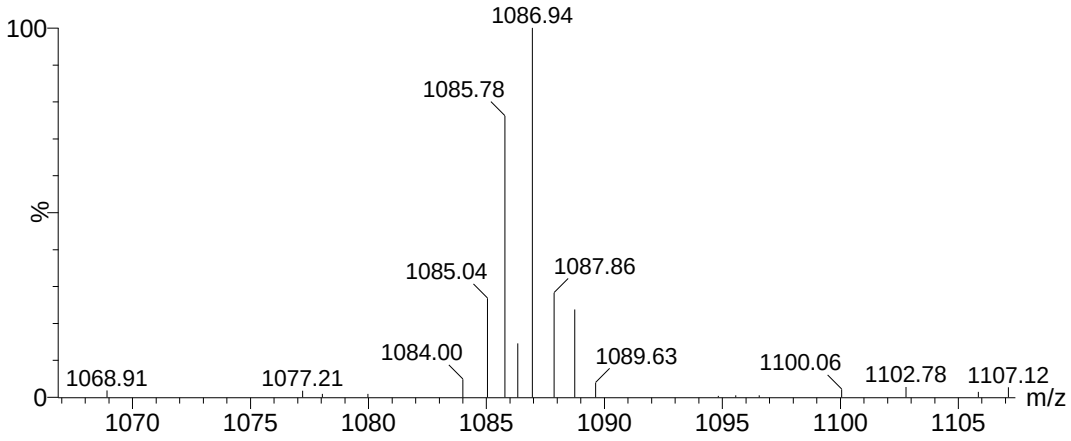

Expanded half-mass ion from spectrum above

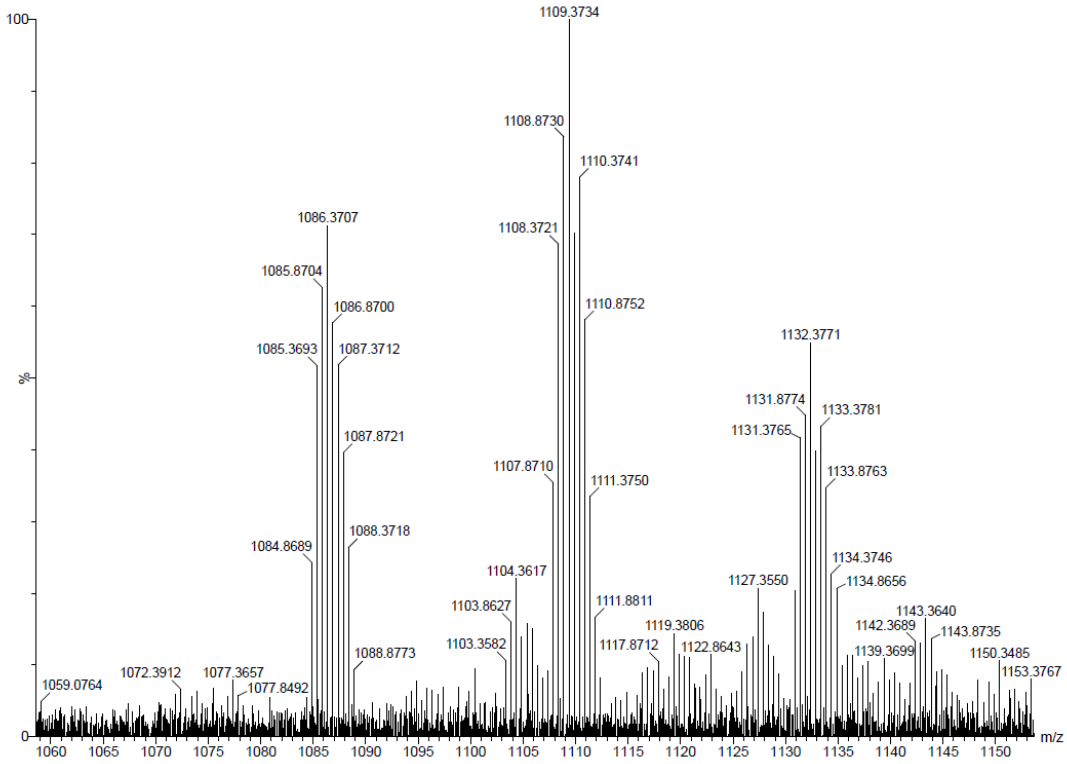

HRMS of **12**, 1086.3701 [M-2H/2], 1109.3734 [M-3H+Na/2],

Compound **13** *c(RGDyK)-DSS-dLys(DOTA-Cu)-Lys(DOTA-Gd)-NH₂*

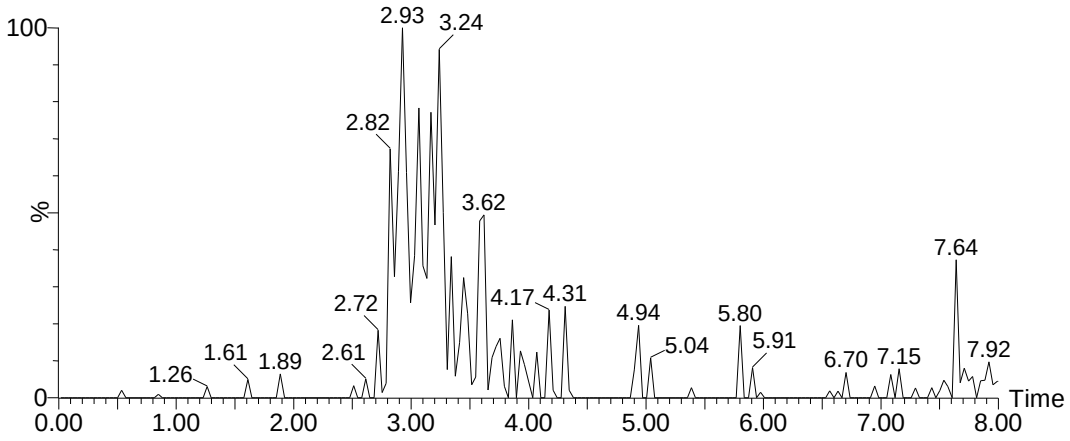

XIC of mass range 1007.8 to 1011.3 m/z

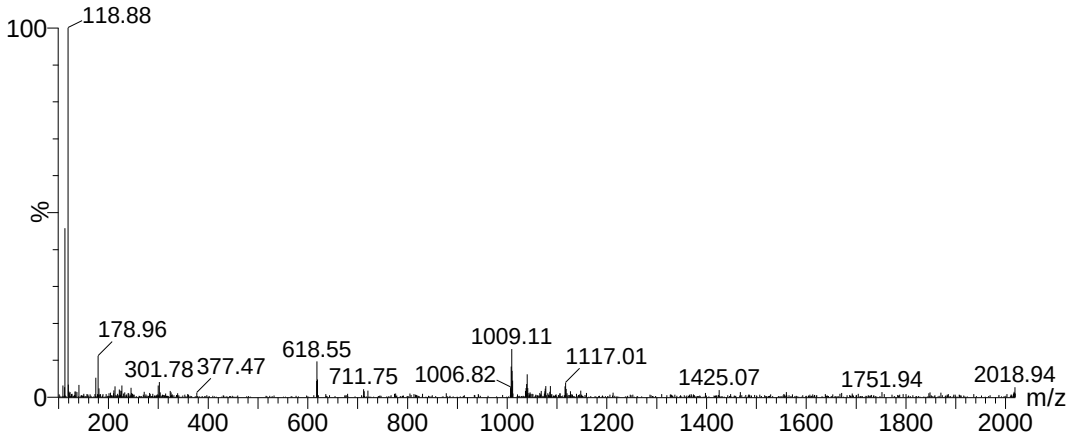

Mass spectrum at 2.96 minutes, 1009.1 m/z [M-2H/2]

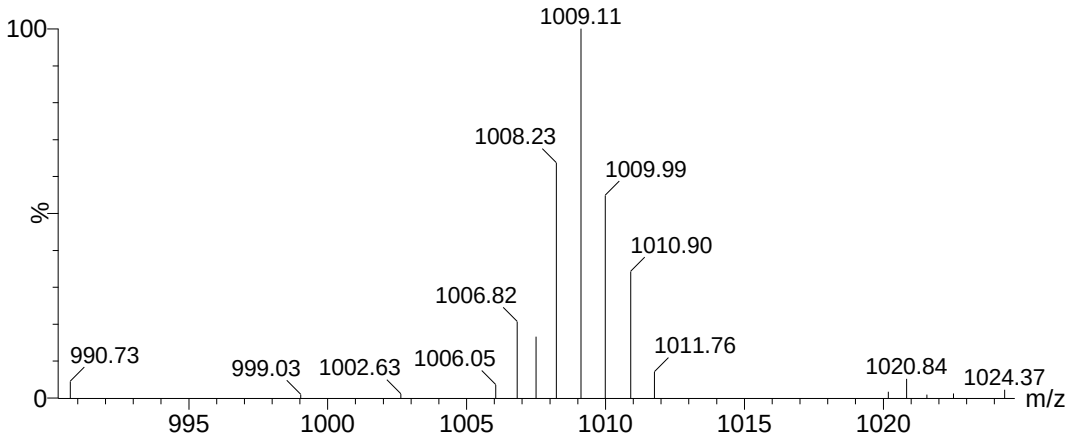

Expanded half-mass ion from spectrum above

Compound **14** *c(RGDyK)-SMCC-dLys(DOTA-Cu)-Lys(DOTA-Gd)-NH₂*

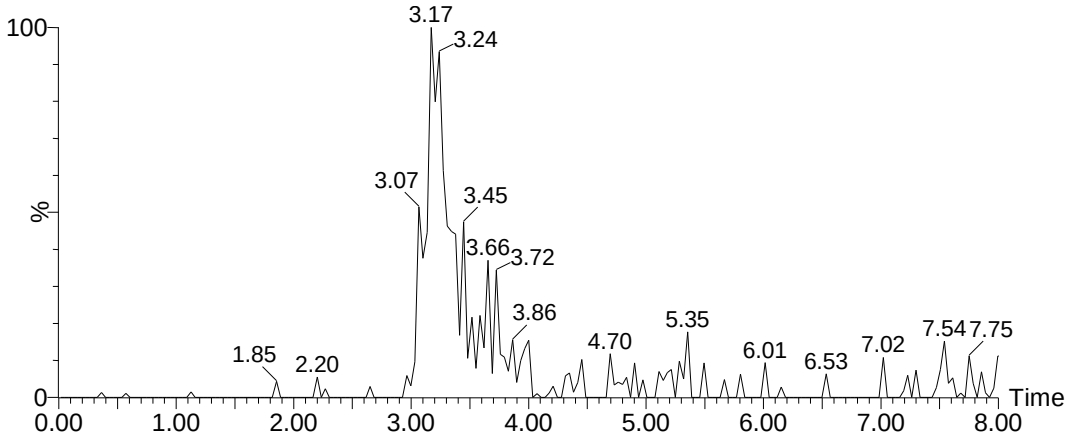

XIC of mass range 1047.2 to 1051.8 m/z

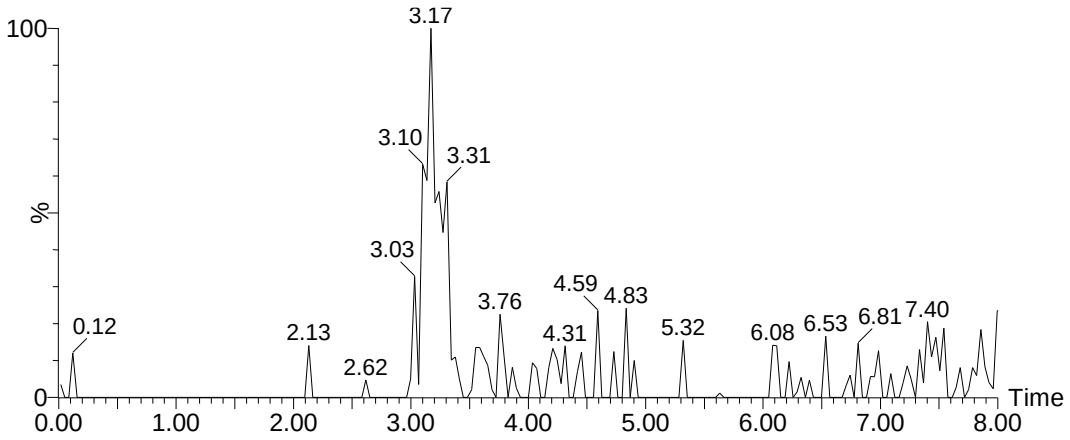

XIC of mass range 1077.7 to 1082.1 m/z

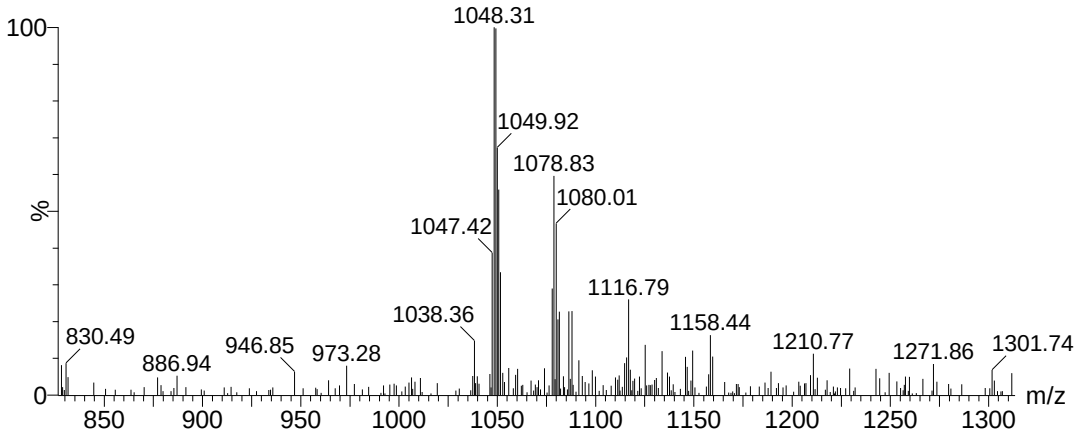

Mass spectrum at 3.24 minutes, 1048.3 m/z [M-2H/2], 1078.8 m/z [M-H+OAc⁻/2]

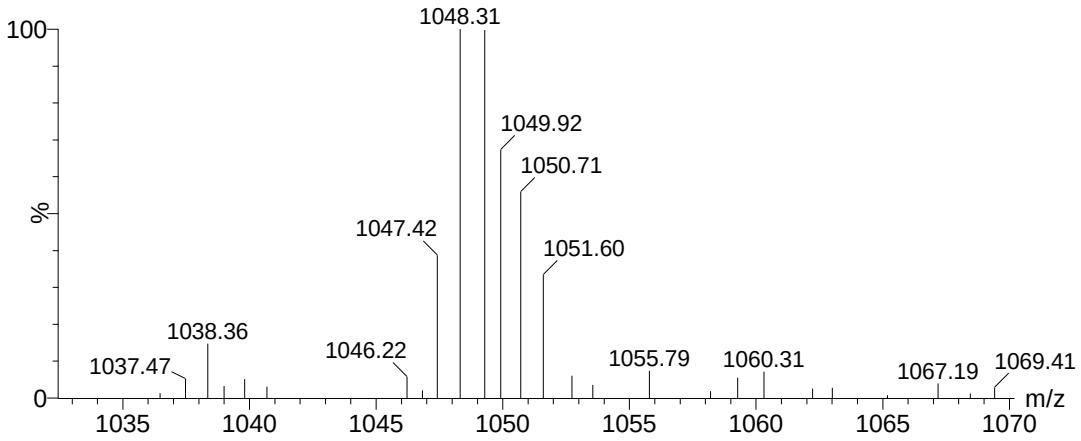

Expanded half-mass ion from spectrum above

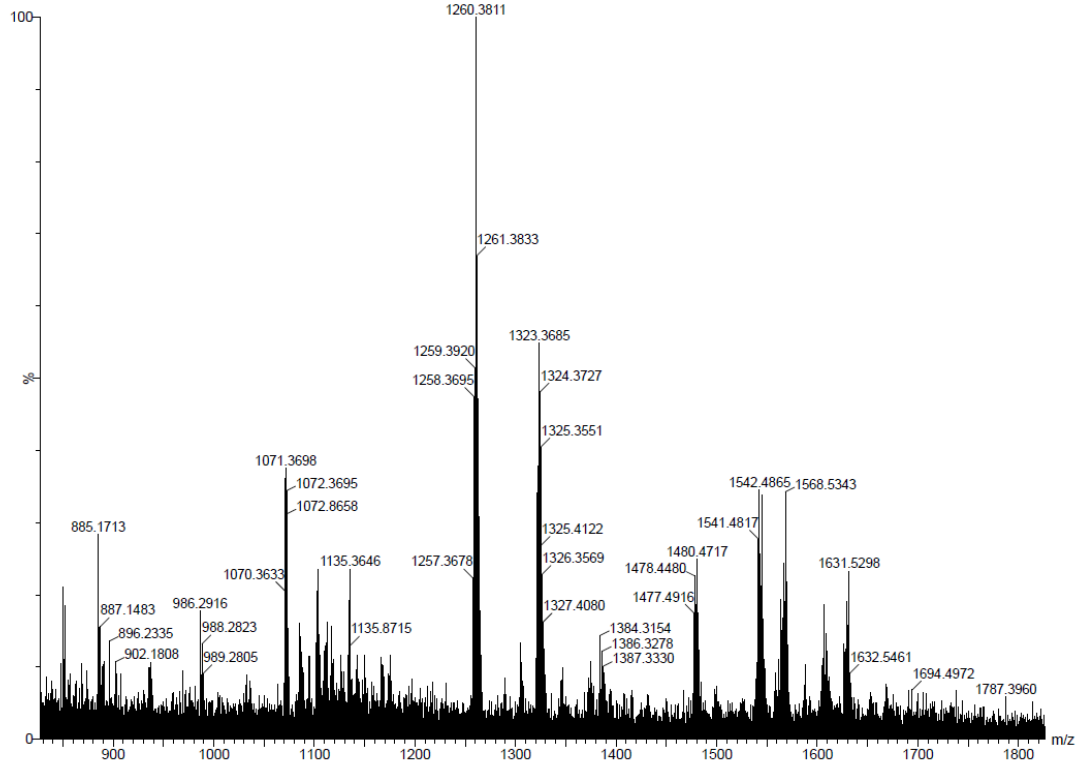

HRMS of **14**, 1071.3698 m/z [M+2Na/2]

Compound **15** *DSS-Lys(DOTA-Gd)-NH₂*

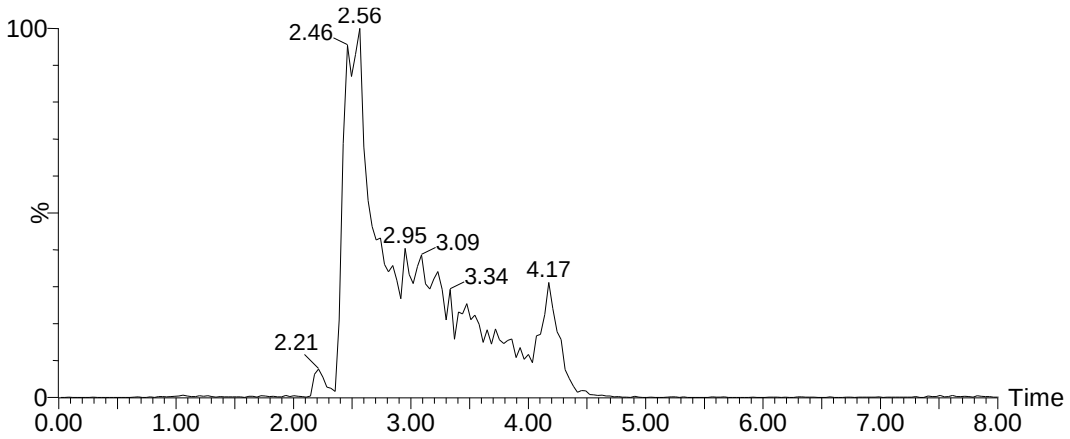

XIC of mass range 894.1 to 897.8 m/z

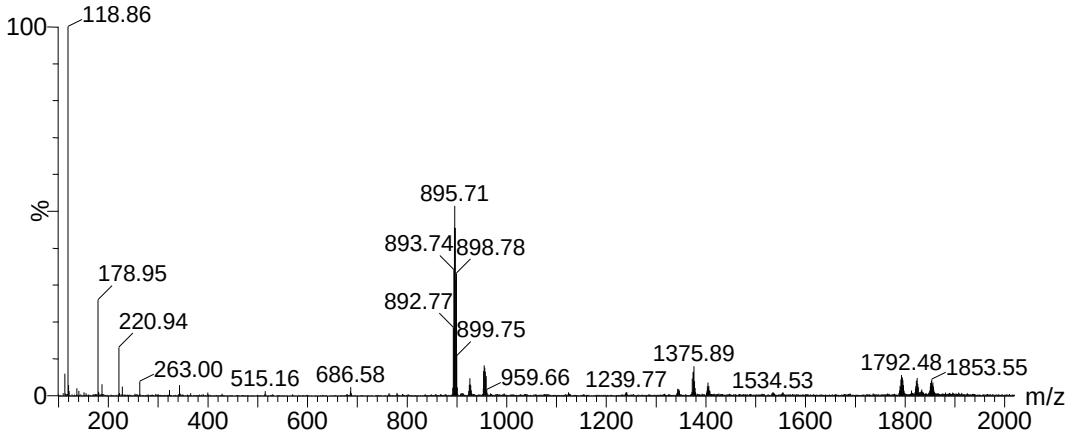

Mass spectrum at 2.49 minutes, 895.7 m/z [M-H] of **15** after treatment with butylamine

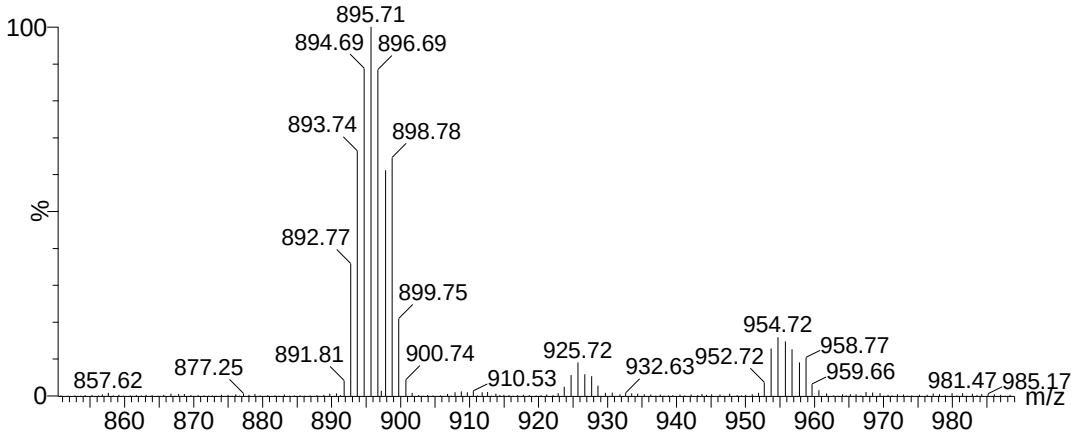

Expanded parent ion from spectrum above

Compound **16a** *DCL-DSS-Lys(DOTA-Gd)-NH₂*

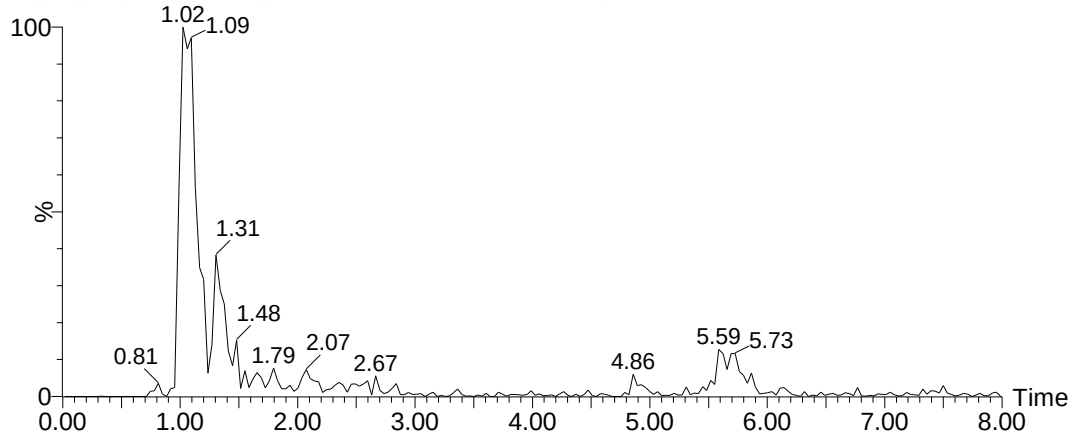

XIC of mass range 568.9 to 572.6 m/z

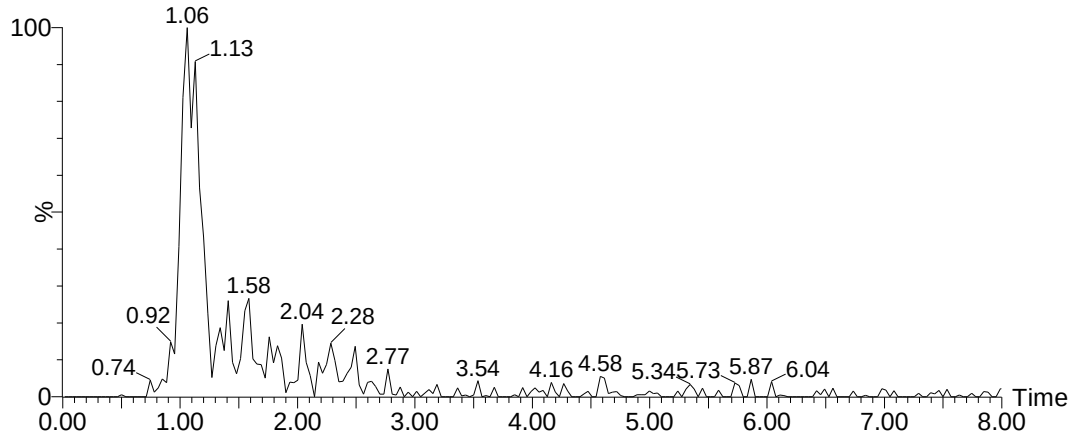

XIC of mass range 1140.1 to 1144.3 m/z

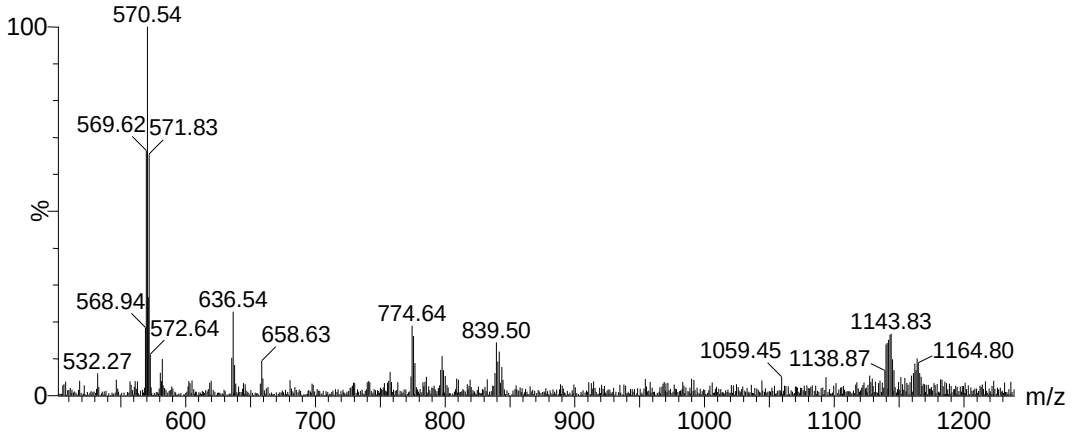

Mass spectrum at 1.06 minutes, 570.5 m/z [M-2H/2], 1143.8 m/z [M-H]

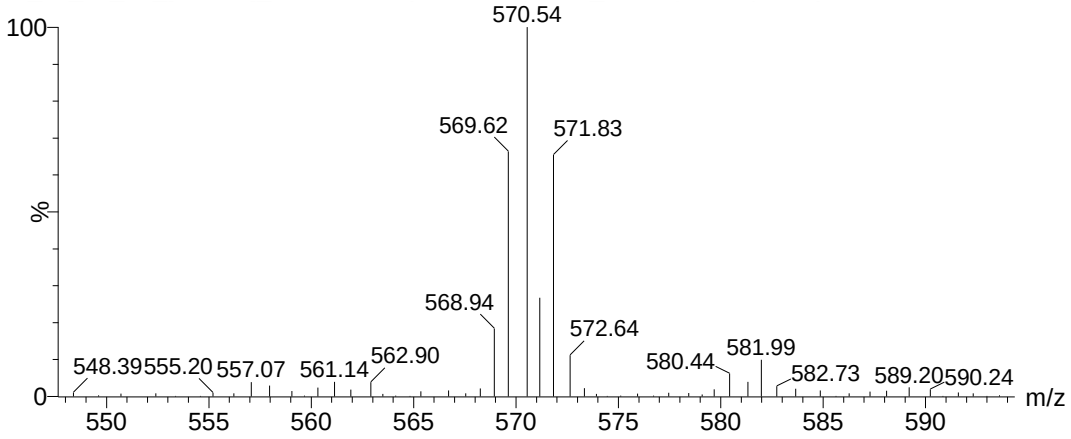

Expanded half-mass ion from spectrum above

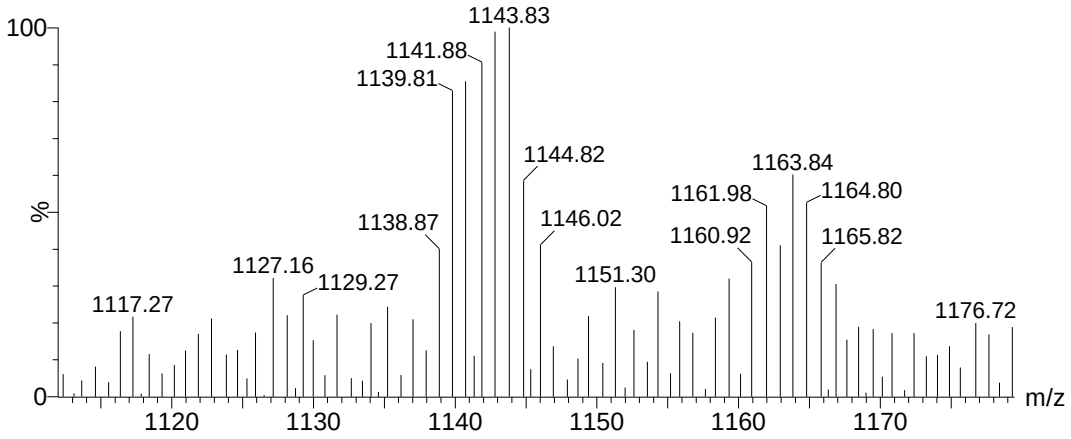

Expanded parent ion from spectrum above

Compound **16b** *DCL-DSS-Lys(DOTA-Gd)-NH₂*

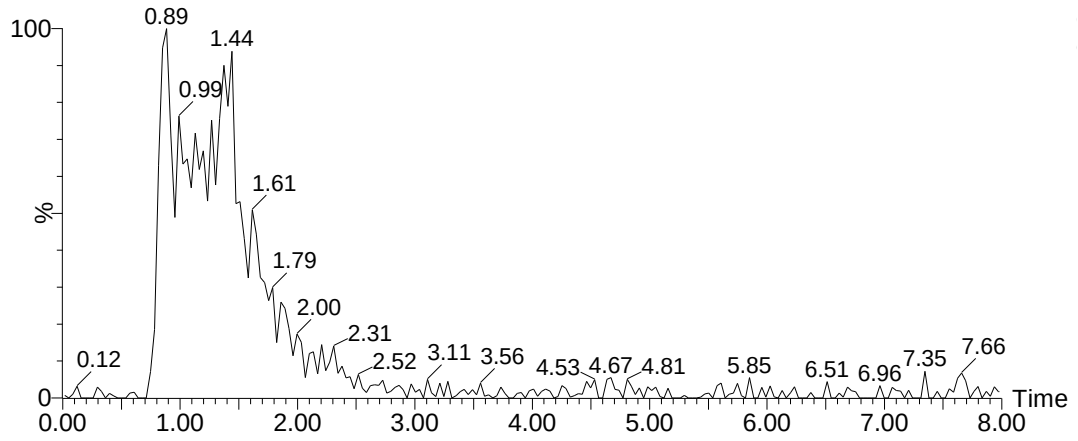

XIC of mass range 1140.2 to 1145.3 m/z

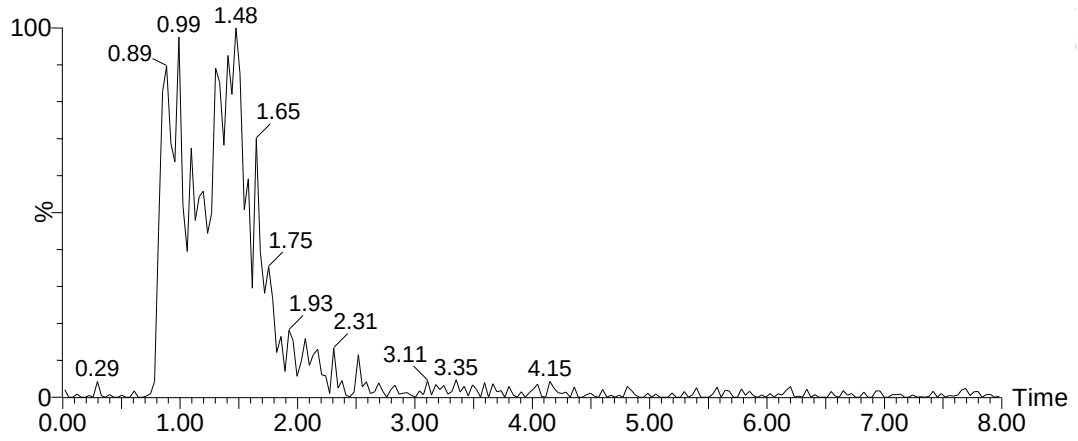

XIC of mass range 569.0 to 572.7 m/z

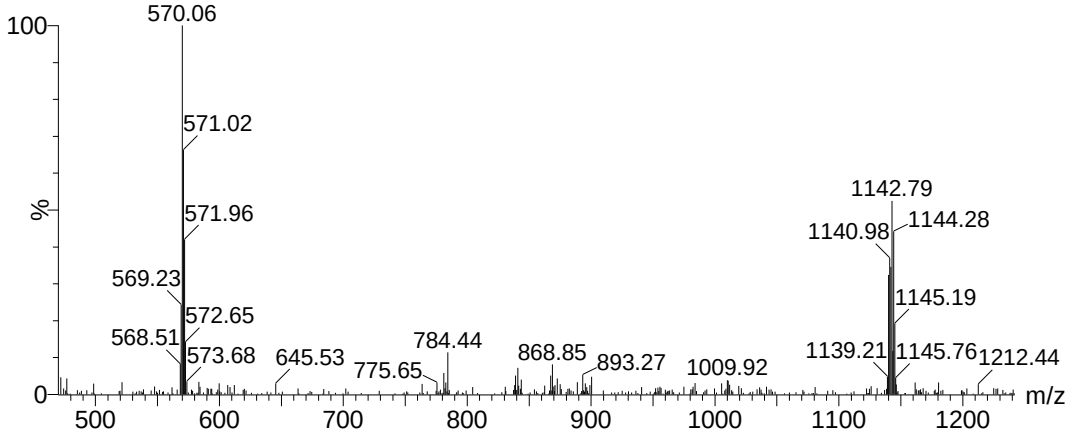

Mass spectrum at 1.09 minutes, 570.1 m/z [M-2H/2], 1142.8 m/z [M-2H/2]

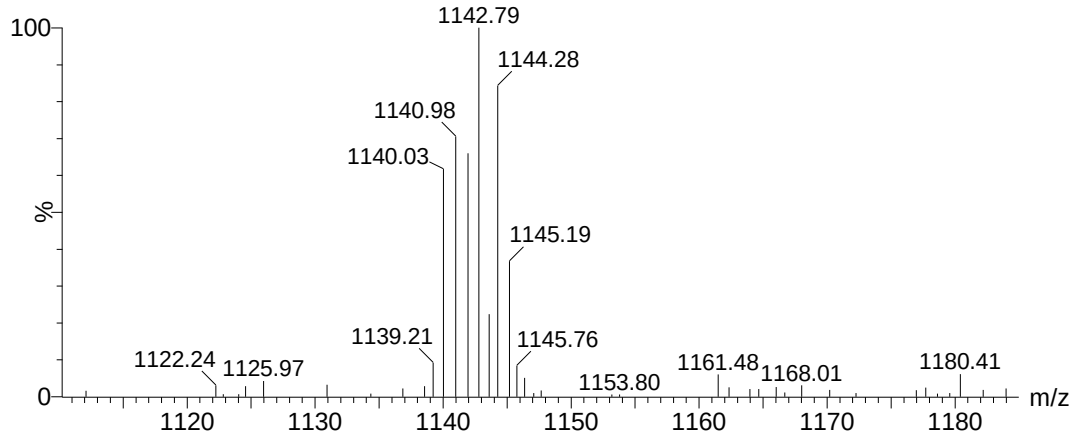

Expanded parent ion from spectrum above

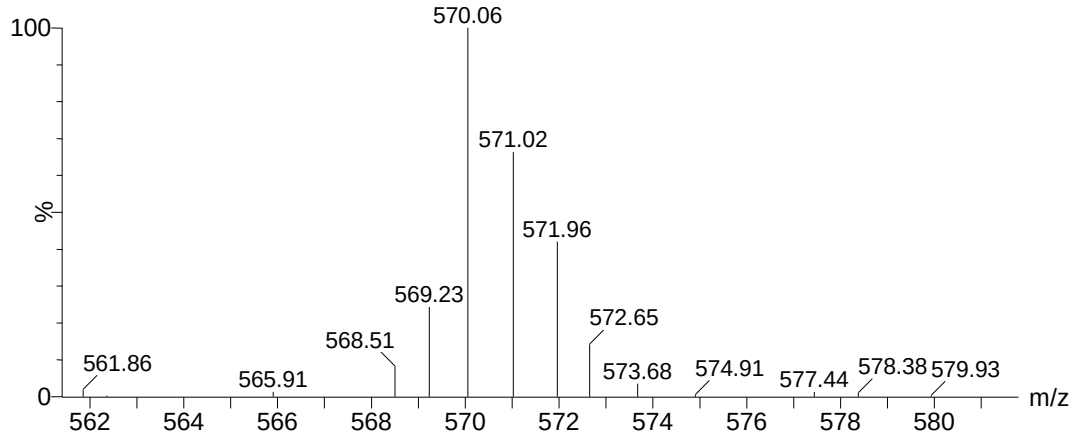

Expanded half mass ion from spectrum above

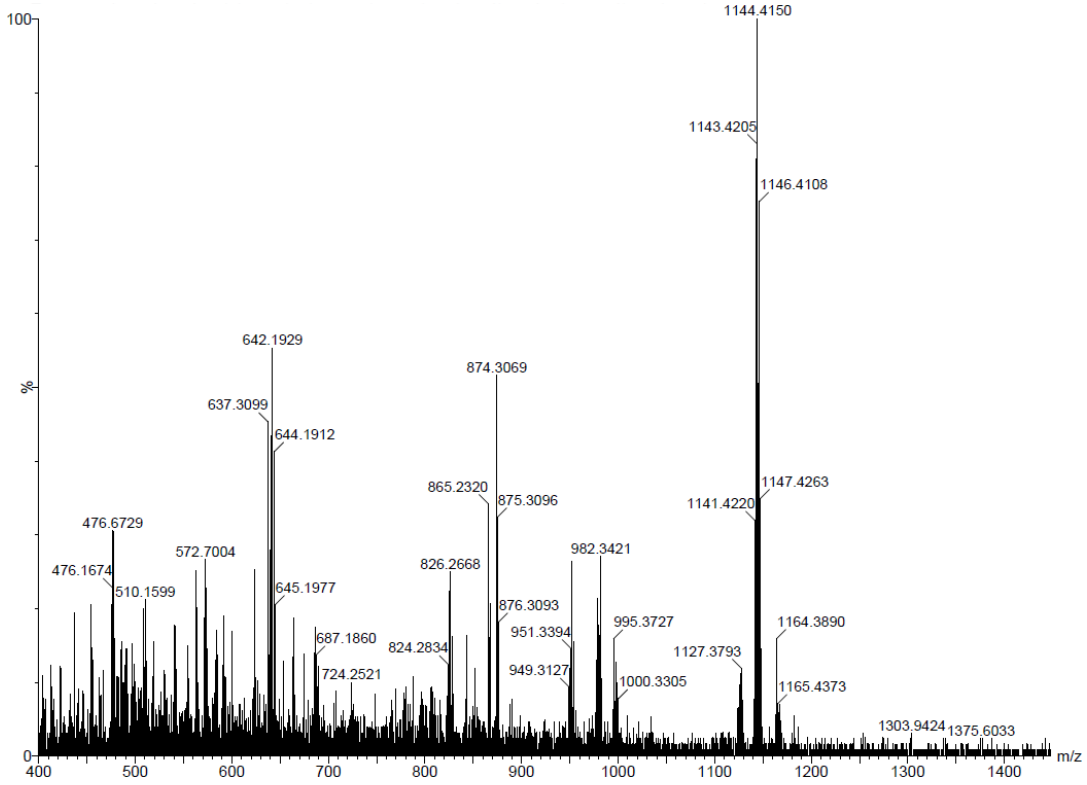

HRMS of **16b**, 1144.4150 m/z [M+H]